Magnetisation of bulk superconductors for future light-weight electric motors

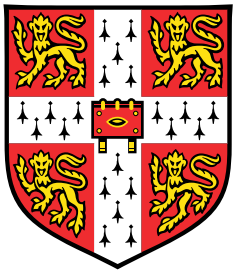

Jan Srpčič

Department of Engineering
University of Cambridge

This dissertation is submitted for the degree of
Doctor of Philosophy

Pembroke College

January 2020

Declaration

This dissertation is the result of my own work and includes nothing which is the outcome of work done in collaboration except as declared in the Preface and specified in the text. It is not substantially the same as any that I have submitted, or, is being concurrently submitted for a degree or diploma or other qualification at the University of Cambridge or any other University or similar institution except as declared in the Preface and specified in the text. I further state that no substantial part of my dissertation has already been submitted, or, is being concurrently submitted for any such degree, diploma or other qualification at the University of Cambridge or any other University or similar institution except as declared in the Preface and specified in the text. It contains fewer than 65,000 words including appendices, footnotes, tables and equations but excluding the bibliography and has fewer than 150 figures.

Jan Srpčič
January 2020

Magnetisation of bulk superconductors for future light-weight electric motors

Jan Srpčič

Bulk superconductors, in their capacity as trapped field magnets, offer a practical means of generating high magnetic fields in small volumes. This is desirable for applications in which portability is of primary concern. In particular, superconducting materials are seen as enablers leading towards light-weight, high power density electric motors to be used in future hybrid-electric passenger aircraft. One of the issues that needs to be addressed before this can become a reality, however, is the instability of trapped magnetic field in these materials, when exposed to external time-varying magnetic fields.

In this work a comprehensive study of the effect of AC magnetic fields on the trapped magnetic field in bulk superconductors is presented. Two distinct geometries are studied; the crossed-field and the parallel configuration, in which the AC magnetic field is applied perpendicular or parallel to the direction of trapped magnetic field, respectively.

An analytical empirical model is derived, with which the decay of trapped magnetic field in the crossed-field configuration can be predicted accurately, provided the value of the critical current density in the material is known. The model is found to be in excellent agreement with the observed experimental data, as well as with finite-element numerical simulations. In the parallel configuration the time dependence of trapped magnetic field is studied as a function of the AC magnetic field amplitude, its frequency and the operating temperature of the superconductor. Subsequently, the data are compared with their equivalent in the crossed-field configuration. It is found that, while the crossed-field configuration leads to a greater rate of decay of trapped field, in both configurations reducing the operating temperature proves an effective mitigation measure against it.

Lastly, the limits of the well established Bean critical state model are studied within the scope of the Campbell penetration depth of magnetic field, which is, itself, a direct consequence of the reversible and elastic movement of flux vortices within the pinning potential. I derive a convenient way of measuring the Campbell penetration depth using a pick-up method, and present measurements of its value in a bulk superconductor at different applied magnetic fields.

Acknowledgements

There are numerous people to whom I am immensely grateful, and without whom this work would not be possible.

Foremost, I would like to thank my supervisor Dr John Durrell, whose support and good humour are in large part what made my years in Cambridge so enjoyable. If matching well with one's supervisor is an important part of a successful PhD, I have been incredibly lucky in this respect.

I would like to thank Dr Difan Zhou for taking me under his wing in the lab from the very start. He was always willing to let me participate in his experiments - if only for the benefit of my experience - for which I am immensely grateful. His patience and good will helped show me how to be a careful and precise experimentalist.

I would like to thank Dr Mark Ainslie for his encouragement and support throughout my PhD. He introduced me to numerical modelling early on and was always willing to help with any hiccup I might have encountered. His confidence in me and his willingness to collaborate opened up many learning opportunities, for which I am very grateful.

I would like to thank Dr Yunhua Shi and Dr Devendra Namburi for providing more superconducting samples than I could ever need. They introduced me to the material science of superconductors, and I could not have wished for more knowledgeable experts from whom to learn.

I would also like to thank Professor Archie Campbell for his unending willingness to discuss anything and everything I needed help with. He showed me the standard of scientist I wish to aspire to.

I would like to thank all members of the Bulk Superconductivity Group for making me feel welcome from the very beginning, and for providing the most supportive and collaborative research environment I have ever had the pleasure to work in - this is something I wish to cultivate in my further career. Also, I would like to thank our colleagues at Siemens, especially Dr Martin Boll, for their support.

I would like to thank my girlfriend Abi for helping me see the important things in life. Without her love and emotional support this journey might have been much more difficult.

Finally, I would like to thank my family, Anja, Breda and Bojan, for their unconditional love and support. They have always stood behind my every decision and for this I remain eternally grateful.

To Archie

Table of contents

List of figures

List of tables

Chapter 1

Introduction

1.1 Scope and aims of the thesis

The air transportation sector is responsible for the emission of 860 million tonnes of carbon dioxide every year [1]. This is about 3 % of the total greenhouse gas emissions produced worldwide. The number of passenger miles flown is projected to double in the next two decades, making sustainability a primary concern. Progress needs to be made towards lower environmental impact air transport by either reducing the number of trips taken or by redesigning the aircraft themselves to be more fuel-efficient.

The energy source for aircraft is jet fuel, owing to its high energy density and to the high power density of the jet engine. Conversely, there are, as yet, no electric nor hybrid-electric transoceanic passenger aircraft. In order to progress into a carbon-neutral society we must gradually transition away from fossil-fuel-powered transportation towards greener and more sustainable alternatives. The electric motor appears to be a likely candidate to replace fossil-fuel based engines.

The European Union has seen a steady increase in the share of electric road vehicles, rising to about 1.8 % in 2017 [2]. This progress has not been shared by the air transport industry primarily due to the prohibitively high weight of the electric motor at the desired power specification. In particular, the power density required by concept hybrid-electric aircraft is estimated on the order of $25\,\mathrm{kW\,kg^{-1}}$, which appears unachievable using conventional technology [3]. Thus, electric motors must be made more efficient before they can become an alternative to the jet engine. One possible way of doing this is by using superconducting materials.

One of the types of electric motors which can be improved by the addition of superconducting materials is the permanent magnet motor. In this type of motor

permanent magnets, rather than coil windings, are used to generate the static DC magnetic field. This can be beneficial as the field generation requires no additional energy and the magnetic field remains constant over time. However, the magnetic field density of conventional magnets is at most about 1.8 T (the saturation magnetisation of iron [4]), which imposes an upper limit to the achievable magnetic loading of the motor. In comparison, bulk superconducting trapped-field magnets have been shown to generate magnetic field densities upwards of 17 T [5] – an order of magnitude higher than conventional magnets – which may lead to a marked increase in the specific power of electric motors. In order to successfully design and construct an electric motor using bulk superconductors three major challenges must be dealt with:

1. Mechanical strength.

   The most promising materials for trapped-field applications are $GdBa_2Cu_3O_{7-\delta}$ bulk superconductors – inherently brittle ceramics. During the magnetisation process (described in detail in Section 2.3.3) the Lorentz forces induced in the material are sufficient to cause cracking and catastrophic failure of the superconductor (the most common mode of failure is cracking during magnetisation). Thus, a means of mechanical reinforcement must be found.

2. Cryogenic and magnetisation systems.

   Since materials only superconduct at temperatures below their critical temperature (92 K for $GdBa_2Cu_3O_{7-\delta}$) a dedicated cryogenic system must be installed to accompany any superconducting motor. Additionally, a portable magnetisation system needs to be developed with which to charge the trapped-field magnets. Both these systems introduce additional weight to the electric motor, which will decrease the total specific power.

3. Magnetic field stability.

   After magnetisation the trapped magnetic field in a bulk superconductor does not remain constant – instead it decays over time following a logarithmic decay rate: if the magnetic field decays by 10 % in the first 10 min after magnetisation, it will subsequently decay an additional 10 % in the following 100 min. Additionally, if the superconductor is exposed to external changing magnetic fields, as will be the case in an electric motor, the decay of trapped field may be markedly accelerated as a consequence of hysteretic losses and heat generation. Thus, understanding this decay is of great interest as it may help ultimately in its mitigation.

This dissertation deals with the third problem – its aim is to discuss the effect AC magnetic fields have on the trapped field of a bulk superconductor. The goal will be to mimic the magnetic environment, expected in a rotating machine, and analyse its effects on magnetised bulks.

1.2 Thesis outline

In Chapter 2 the physics of superconductivity is introduced and the most important theories describing the behaviour of type-II superconductors are summarised. For the purposes of this thesis classical electromagnetism is sufficient to describe the relevant physical phenomena, hence the underlying quantum mechanical picture is not studied in detail. As we shall see, the Bean critical state model [6] along with Maxwell's equations is sufficient to account for most of the observables of interest, such as the critical current density, or the magnetisation of the superconductor. Bulk (RE)BCO superconductors (where RE is a rare earth or yttrium, B is barium, C is copper, and O is oxygen) are introduced and their properties discussed as these materials are studied in the subsequent chapters.

In Chapter 3 the methods used throughout the experimental work towards this thesis are described. This entails sample preparation and growth - the method used to manufacture the bulk (RE)BCO superconductors is the top-seeded melt growth technique [7]. Next, the magnetisation procedures to charge the bulk superconductors are described; field cooled magnetisation (FC), and pulsed field magnetisation (PFM). They are used to probe the full field-trapping capabilities and the realistically achievable trapped fields of the samples, respectively. Since, subsequent to magnetisation, the samples are exposed to time-varying magnetic fields, next the generation of the AC magnetic field is described, along with the measurement of the sample response (be it with Hall sensors or pick-up coils). Finally, a finite element modelling (FEM) technique is detailed, which is employed to generate numerical simulations to compare with the experimental data.

In chapters 4, 5, and 6 the experimental results are presented and analysed. Each of the chapters begins with a literature review in which the most important relevant studies are summarised, followed by the the presentation and analysis of new experimental results acquired for the production of this thesis.

Chapter 4 looks at the influence of AC magnetic fields on the trapped magnetic field in a bulk superconductor in the crossed-field configuration. Here, the orientation of the AC field is perpendicular to the direction of the trapped field, which is the

configuration found to lead to the greatest rate of decay of trapped magnetic field. An empirical analytical model is presented, with which the time dependence of trapped field in the crossed-field configuration can be predicted accurately, provided the value of critical current density in the superconductor is known. The model is corroborated with measurements of decay, and with FEM simulations, and all three are found to be in excellent agreement.

Chapter 5 looks at the parallel field configuration, in which, unlike in Chapter 4, the AC magnetic field is applied parallel to the direction of the trapped magnetic field. Initially, the highest achievable trapped magnetic field in a (RE)BCO sample is determined using PFM, and subsequently the sample is exposed to external AC magnetic fields. The decay of trapped field is analysed as a function of the AC magnetic field amplitude and frequency, and of the operating temperature of the superconductor. Then, the parallel configuration is compared to the crossed-field configuration in terms of decay of trapped field, and measures to mitigate decay are discussed.

Chapter 6 looks more deeply into the microscopic picture of the mixed state of type-II superconductors, and into the interaction of flux vortices with their pinning centres. The Campbell model [8] is introduced as the extension of the Bean critical state model in the regime of low-amplitude applied AC magnetic fields and reversible vortex movement within the flux pinning potential (this reversible movement is not accounted for within the Bean model framework). The governing partial differential equations for vortex movement are introduced and solved numerically in their complete form, and analytically in a linearised form, which proves convenient for comparison of theory with experiment. The data are presented and the Campbell penetration depth in a bulk (RE)BCO superconductor is discussed.

Finally, in Chapter 7, the conclusions are drawn and the further work is outlined. Here, the plans for a superconducting rotating ersatz motor, with which to test the bulk superconductors in a real machine environment, are described. Since the actual magnetic environment in a superconducting rotating machine will likely be a combination of the parallel and crossed-field configurations, the ersatz motor will provide a more accurate test for the expected performance of bulk superconductors, acting as trapped-field magnets.

Chapter 2

The physical background

2.1 The fields B, M and H

As a preface to this chapter we begin with an overview of the definitions and meanings of the three fields that arise in magnetodynamics: the magnetic field density **B** (here referred to simply as magnetic field), the magnetic field strength **H**, and the magnetisation **M**. The purpose of this overview is to establish the nomenclature used in the rest of this thesis, and to define unambiguously the relations between the fields in normal magnetisable (e.g. ferromagnetic) materials and in superconducting materials. In the latter the focus will be on type-II superconductivity. For a thorough discussion on the meaning of Maxwell's equations in normal matter, see [9], and for superconducting matter, see [10].

2.1.1 Normal matter

On the molecular scale of matter the microscopic magnetic field, **b**, is defined by the two Maxwell's equations

$$\nabla \cdot \mathbf{b} = 0, \tag{2.1}$$

and

$$\nabla \times \mathbf{b} = \mu_0 \left(\mathbf{J} + \epsilon_0 \frac{\partial \mathbf{E}}{\partial t} \right), \tag{2.2}$$

where μ_0 and ϵ_0 are the vacuum permeability and permittivity, respectively, **J** is the current density and **E** is the electric field. Equations 2.1 and 2.2 tell us that the field **b** is lossless, i.e. there are no magnetic sources (monopoles) or sinks, and that the field arises as a consequence of moving charges and time-varying electric fields. By

averaging these equations over a length scale much greater than the microscopic scale over which **b** varies, we can obtain the corresponding equations for the macroscopic magnetic field, **B**. This is the magnetic field, in Tesla, that we generate by passing current through a conductor, or that we measure using a Hall or inductive sensor.

In matter a second field has to be introduced to take into account the contribution of any magnetic dipoles present. A distribution of magnetic dipoles, which are effectively microscopic current loops, leads to an equivalent macroscopic distribution of current density **J** in the material. While in electrical insulators this current density is equivalent to the current density in equation 2.2 (Ampere's law), in electrical conductors the current density in equation 2.2 includes also the ohmic current due to a potential difference across the conductor. Here, the discussion is limited to the current density in the absence of any current sources or sinks, hence the current density that arises from the distribution of magnetic dipoles is equivalent to the current density in Ampere's law.

In the absence of current sources charge conservation dictates

$$\nabla \cdot \mathbf{J} = 0. \tag{2.3}$$

Hence, there exists a vector potential, **M**, for which the critical current density can be written as

$$\nabla \times \mathbf{M} = \mathbf{J}. \tag{2.4}$$

This vector potential is typically referred to as magnetisation and can be calculated with the additional boundary condition $\mathbf{M} = 0$ at the material surface. Equation 2.4, however, is insufficient to fully define magnetisation. A gradient of any scalar may be added to **M** and equation 2.4 will still hold. Hence, the formal definition of magnetisation is as a volume density of magnetic dipoles,

$$\frac{1}{2}\int_V \mathbf{r} \times \mathbf{J}\, dV = \int_V \mathbf{M}\, dV, \tag{2.5}$$

where the integral goes over the volume of the material. The microscopic picture, here, is that of a volume density of magnetic dipoles in matter, which may be affected by, and contribute to, the magnetic field.

It is possible to arrive at the above expression by substituting equation 2.4 into the left hande side of equation 2.5 and transforming the integral with the use of Stokes'

theorem,

$$\int_V \mathbf{r} \times (\nabla \times \mathbf{M})\, dV = -\oint_{\partial V} \mathbf{r} \times (\mathbf{M} \times\, d\mathbf{S}) - \int_V (\mathbf{M} \times \nabla) \times \mathbf{r}\, dV. \tag{2.6}$$

The surface integral on the right hand side is over the boundary of the the volume (where $\mathbf{M} = 0$), hence it is equal to zero. The term in the second integral is simply $(\mathbf{M} \times \nabla) \times \mathbf{r} = -2\mathbf{M}$, which brings us to equation 2.5.

In principle, the magnetic field and the magnetisation are independent fields – they arise due to moving charges and bound magnetic dipoles, respectively – and are sufficient to describe the magnetodynamics of matter. However, in some cases it is convenient to define an additional field, the magnetic field strength, as

$$\mathbf{H} = \frac{\mathbf{B}}{\mu_0} - \mathbf{M}. \tag{2.7}$$

The magnetic field strength can be used to describe finite size effects due to which the magnetisation in matter does not change linearly with magnetic field (see the example, below). In the absence of any applied magnetic field the $\mathbf{H}$ field is sometimes referred to as the demagnetising field, $\mathbf{H}_D$. This is because its direction can be opposite the direction of magnetisation, hence demagnetising the material. In vacuum, however, the fields $\mathbf{B}$ and $\mathbf{H}$ differ only by a factor of μ_0 and are equivalent.

Additionally, in isotropic materials at small magnetic fields the relation between $\mathbf{B}$ and $\mathbf{H}$ is linear,

$$\mathbf{B} = \mu\mathbf{H}, \tag{2.8}$$

where μ is the material permeability ($\mu = \mu_0$ in vacuum). Throughout this thesis the fields $\mathbf{B}$ and $\mathbf{M}$ will be referred to as independent fields, which, once known, fully define the field $\mathbf{H}$.

As an example of the above, let us look at a simplified case of a ferromagnetic cylinder of radius r_0 and height h_0 in which there is a constant density of magnetic dipoles. The magnetisation is assumed constant in the z-direction, $\mathbf{M} = M_0(1 - H(r - r_0))\hat{\mathbf{e}}_z$, where $H(r - r_0)$ is the Heaviside step function and $\hat{\mathbf{e}}_z$ is the unit vector in the z-direction (Figure 2.1 (a)).

To calculate the magnetic field at the centre of the cylinder we firstly find the equivalent surface currents from $\mathbf{M}$ via equation 2.4, which in one dimension in cylindrical coordinates reads

$$-\frac{\partial}{\partial r}\left(M_0\left(1 - H\left(r - r_0\right)\right)\right)\hat{\mathbf{e}}_\phi = M_0\delta\left(r - r_0\right)\hat{\mathbf{e}}_\phi = J\hat{\mathbf{e}}_\phi, \tag{2.9}$$

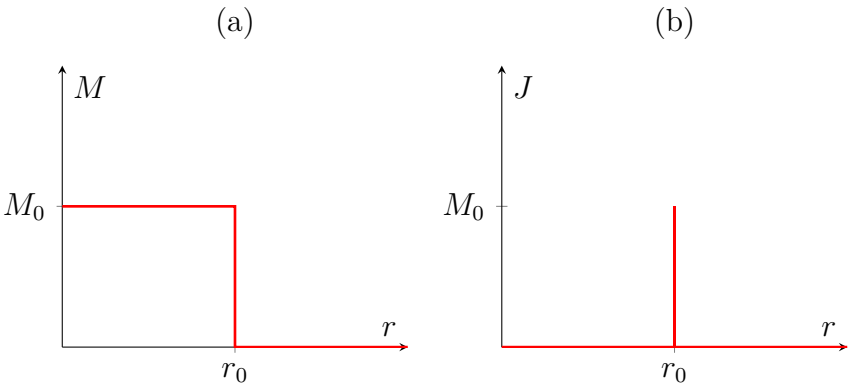

Fig. 2.1 (a) The magnetisation of a uniformly magnetised cylinder and (b) an equivalent surface current.

where r is the radial coordinate, $\hat{\mathbf{e}}_\phi$ the unit vector in the ϕ-direction, J the surface current density, and $\delta(r - r_0)$ is the Dirac delta function. The currents calculated in this way (shown in Figure 2.1 (b)) are used purely for the purposes of calculation; the microscopic picture remains one of a density of magnetic dipoles.

Next, the magnetic field in the centre of the cylinder due to the surface currents can be calculated using the Biot-Savart law,

$$\mathbf{B}(\mathbf{r}) = \frac{\mu_0}{4\pi} \int_V \frac{\mathbf{J}(\mathbf{r}') \times (\mathbf{r} - \mathbf{r}')}{|\mathbf{r} - \mathbf{r}'|^3} \, d^3\mathbf{r}'. \tag{2.10}$$

The cylinder inhabits the space $-h_0/2 \leqslant z \leqslant h_0/2$ and $r \leqslant r_0$, hence we can evaluate the z-component of the magnetic field as

$$B = \frac{\mu_0}{4\pi} \int_{r=0}^{r=r_0} \int_{z=-h_0/2}^{z=h_0/2} \frac{r M_0 \delta(r - r_0)}{(r^2 + z^2)^{3/2}} 2\pi r \, dr \, dz. \tag{2.11}$$

Integrating, and defining the cylinder aspect ratio $\eta = h_0/2r_0$, we arrive at the result

$$B = \frac{\mu_0 M}{\sqrt{1 + \eta^{-2}}}. \tag{2.12}$$

Note the magnetic field and the magnetisation have the same sign (i.e. they are both positive). The demagnetising field can then be expressed as

$$H_D = \frac{B}{\mu_0} - M = \left(\frac{1}{\sqrt{1 + \eta^{-2}}} - 1 \right) M = N(\eta) M, \tag{2.13}$$

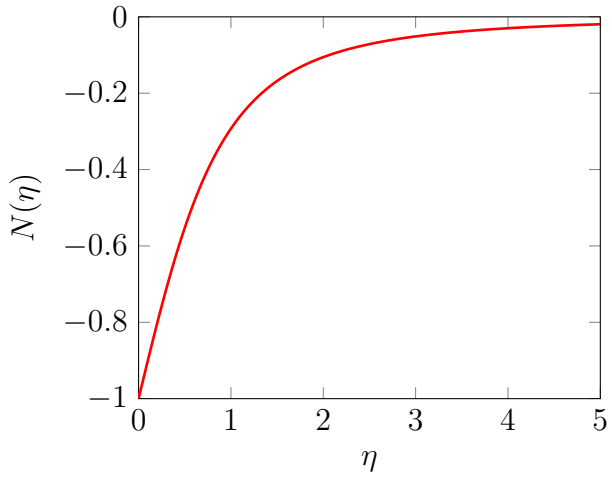

Fig. 2.2 The demagnetisation factor as a functing of the cylinder aspect ratio $\eta = h_0/2r_0$.

where we defined the demagnetisation factor $N(\eta)$. It can be seen that $H_D \leq 0$ for all values of η. The total magnetic field strength, in the presence of an external magnetic field B_0, can be written as

$$H = H_D + \frac{B_0}{\mu_0}. \tag{2.14}$$

The demagnetisation factor for a varying cylinder aspect ratio η is shown in Figure 2.2. In the $\eta \to \infty$ limit, which represents an infinitely long and thin cylinder, the demagnetisation factor is zero. Hence, $H_D = 0$ and $B = \mu_0 M + B_0$. In the case $\eta \to 0$, which represents a flat and infinitely wide cylinder the demagnetisation factor is $N = -1$, hence $H = -M$ and $B = B_0$. This latter case is equivalent to a current loop of infinite radius carrying a current where the magnetic field in the centre decays inversely with the loop radius (as $r \to \infty$, $B \to 0$).

2.1.2 Superconducting matter

Superconductors are diamagnetic materials, hence the direction of magnetisation is opposite the direction of the applied magnetic field. In type-II superconductors (see characterisation of superconductivity in Section 2.2.3) the absolute value of magnetisation was shown by Abrikosov [11] to increase linearly with magnetic field up to the first critical field, and decay inversely with field between the first and second critical fields (the mixed state). At the second critical field the magnetisation is zero. Additionally, the absolute value of magnetisation in the mixed state is typically much smaller than the applied field; $\mu_0 M \ll B$. The maximum value of magnetisation itself depends on

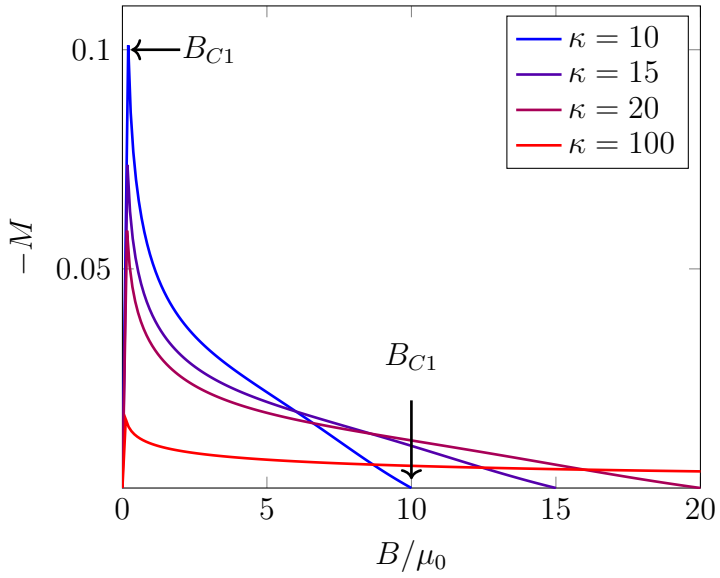

Fig. 2.3 The Abrikosov magnetisation (dimensionless) as a function of applied magnetic field for a varying Ginzburg-Landau parameter. The two critical fields, B_{C1} and B_{C1} are marked for the $\kappa = 10$ case. Reproduced from [13].

the Ginzburg-Landau parameter κ; a larger value of κ leads to a decreasing absolute value of magnetisation (see Figure 2.3). In the present work the discussion will mainly focus on cuprate superconductors, for which the Ginzburg-Landau parameter is $\kappa \approx 100$ [12]. Hence, a very good approximation will be

$$\mathbf{M} = 0, \tag{2.15}$$

$$\mathbf{B} = \mu_0 \mathbf{H}. \tag{2.16}$$

Then, Maxwell's equations in type-II superconductors are identical to those in vacuum and we can set the magnetic permeability to $\mu = 1$.

There is, however, a second type of magnetisation that can be defined in type-II superconductors, which is not the Abrikosov magnetisation in Figure 2.3. It is the total magnetic moment per unit volume due to persistent transport currents flowing through the superconductor and can formally be defined in the same way as in normal matter via equation 2.5. These transport currents are similar to e.g. eddy currents in a normal metal induced in a changing magnetic field as per Faraday's law of induction. The currents in a normal metal, however, will decay much more quickly than the persistent currents in a superconductor, hence it is meaningless to talk about a magnetic moment at longer timescales.

The superconductor magnetisation, defined in this way, can be useful for describing the current-carrying capabilities of the material as typically its value will be proportional to the current. Its value will also be proportional to the size of the sample, however, making the local magnetisation ill defined. Conversely, in normal materials the local magnetisation is well defined as the local density of magnetic dipoles.

Additionally, the distinction between the Abrikosov magnetisation and the total magnetic moment per unit volume due to transport currents is made apparent when calculating the total loss in the superconductor, $Q = \mathbf{E} \cdot \mathbf{J}$. If the total current density is written as a sum of the (Abrikosov) magnetising currents and transport currents, $\mathbf{J} = \mathbf{J}_M + \mathbf{J}_T$, the total loss can be calculated as $Q = \mathbf{E} \cdot \mathbf{J_T}$. The magnetisation currents are lossless and, hence, $\mathbf{E} \cdot \mathbf{J}_M = 0$.

A typical experiment involving type-II superconductors is to measure the so called magnetisation hysteresis loop (see the Bean model, Section 2.2.5) in which the magnetisation of a superconducting sample is measured as a function of applied magnetic field. The magnetisation in this case is the total magnetic moment of the sample per unit volume, and not the magnetisation in equation 2.7. Hence, when interpreting these experiments the value of permeability remains $\mu = \mu_0$. The slope of the magnetisation curve is due to the flux pinning forces, which are themselves the underlying cause for irreversible behaviour and hysteresis. Throughout this dissertation, unless explicitly stated otherwise, the term magnetisation will be used to describe the second type of magnetisation, the total magnetic moment per unit volume. The Abrikosov magnetisation will be assumed zero, such that the relation $\mathbf{B} = \mu_0 \mathbf{H}$ will always hold. Hence, the magnetic field $\mathbf{B}$ will be sufficient for the complete description of magnetodynamics in type-II superconductors.

2.2 The physics of superconductivity

2.2.1 Definition

Superconductivity is a state of matter, exhibited by certain materials when cooled below a material dependent transition temperature. Its onset is accompanied by a vanishing electrical resistivity and an expulsion of magnetic fields from within the interior of the material. These properties make superconductors distinct from all other materials and particularly interesting for certain applications requiring high current carrying capabilities, and, equivalently, high magnetic field. Formally, the two defining properties can be written as follows:

1. $\mathbf{B} = 0$; exclusion of the magnetic field from the material [14],

2. $\rho = 0$; vanishing electrical resistance in the material [15].

The two properties define a new state of matter, superconductivity, which occurs in certain matter when it is cooled down below a material dependent transition temperature, called the critical temperature, T_C. The first property defines the Meissner-Ochsenfeld effect, in which the material, when cooled below T_C, expels all magnetic field from its interior such that it is zero throughout the superconductor (except in a thin surface layer; see London penetration, below). This was initially observed by measuring the magnetic field between two superconducting cylinders, which itself suddenly rose when the temperature was lowered below T_C, indicating expulsion from the superconductor.

The second property states that the electrical resistance of the superconductor approaches zero, i.e. there is little dissipation of current flow. For example, a superconducting loop in which current is circulating will be able to support the current with little decay over time (with the decay constant on the order of 10^{12} s [16]). Both these properties are independent and do not follow from one another.

2.2.2 The London equations

Superconductivity is fundamentally a quantum mechanical phenomenon, and yet some observable predictions can be made using a purely classical approach. Specifically, both properties defining the superconducting state, zero magnetic field and zero electrical resistivity, can be described using the London equations [17]. Assuming there is a number density n_S of charge carriers inside the superconductor with charge q, mass m and velocity v_S, Newton's second law for one such carrier can be written as

$$m\frac{d\mathbf{v_S}}{dt} = q\mathbf{E}, \tag{2.17}$$

where $\mathbf{E}$ is the electric field at the position of the charge carrier. Next, the current density $\mathbf{J}$ can be written in the usual form

$$\mathbf{J} = n_S q\mathbf{v_S}. \tag{2.18}$$

Calculating the time derivative of the above equation and substituting into equation 2.17, we get the first London equation

$$\frac{d\mathbf{J}}{dt} = \frac{n_S q^2}{m}\mathbf{E}, \tag{2.19}$$

which describes the constitutive relation between the electric field and current density. As an example, let us consider the effect of an impulse of electric field, $E = E_0\,\delta(t)$, on a superconductor without any current ($\delta(t)$ is the Dirac delta function). Inserting the electric field impulse into the (one-dimensional) London equation, we arrive at

$$\frac{dJ}{dt} = \frac{n_S q^2 E_0}{m}\,\delta(t). \tag{2.20}$$

This differential equation can be solved readily by using the Laplace transform to obtain an equivalent algebraic equation. In the simplest case, in which $\mathcal{L}(dJ(t)/dt) = sJ(s)$, and $\mathcal{L}(\delta(t)) = 1$, where s is the complex frequency, the resultant algebraic equation becomes

$$J(s) = \frac{n_S q^2 E_0}{m}\frac{1}{s}. \tag{2.21}$$

Then, taking the inverse Laplace transform of the above, whereby $\mathcal{L}^{-1}(1/s) = H(t)$ ($H(t)$ is the Heaviside step function), we obtain the result

$$J = \frac{n_S q^2 E_0}{m}H(t). \tag{2.22}$$

This equation, albeit derived from simple assumptions, is able to capture the lossless behaviour of the current in a superconductor - the current remains constant after the electric field is removed. Additionally, the calculated current has a finite (maximum) value, which, as described in later sections, is also a physical result.

To obtain an equation, describing the magnetic field behaviour we can apply the curl operator to equation 2.19,

$$\frac{d}{dt}\nabla \times \mathbf{J} = \frac{n_S q^2}{m}\nabla \times \mathbf{E}. \tag{2.23}$$

Then, substituting in Faraday's law of induction, $\nabla \times \mathbf{E} = -\partial\mathbf{B}/\partial t$, and integrating with respect to time, we arrive at the second London equation

$$\nabla \times \mathbf{J} = -\frac{n_S q^2}{m}\mathbf{B}. \tag{2.24}$$

This equation relates the magnetic field inside the superconductor with the current, and encapsulates sufficient physics to describe the Meissner effect. By expressing the current using Ampere's law, $\nabla \times \mathbf{B} = \mu_0 \mathbf{J}$, we can write

$$\nabla \times \left(\frac{1}{\mu_0} \nabla \times \mathbf{B} \right) = -\frac{n_S q^2}{m} \mathbf{B}. \tag{2.25}$$

Then, making use of the vector calculus identity for the vector Laplacian $\nabla^2 \mathbf{B} = \nabla (\nabla \cdot \mathbf{B}) - \nabla \times (\nabla \times \mathbf{B})$, with $\nabla \cdot \mathbf{B} = 0$, we arrive at the equation

$$\nabla^2 \mathbf{B} = \frac{\mu_0 n_S q^2}{m} \mathbf{B}. \tag{2.26}$$

The solution of the above equation is an exponential decay of the magnetic field with distance from the material boundary. The characteristic distance, over which the magnetic field decays, is the London penetration depth

$$\lambda_L = \sqrt{\frac{m}{\mu_0 n_S q^2}}. \tag{2.27}$$

Thus, the magnetic field in reality is not excluded completely from the superconductor; there exists a layer of thickness λ_L beneath the surface of the superconductor up to which the magnetic field can penetrate. For (RE)BCO materials, studied in this work, the London penetration is on the order of $\approx 100\,\text{nm}$ [18], and is anisotropic, reflecting the crystal anisotropy of the material (see Section 2.3).

2.2.3 Type-I and type-II superconductivity

The London penetration depth is a characteristic distance over which the magnetic field decays inside the superconductor. However, there are two distinct types of superconductivity, which can be characterised based on the way in which the magnetic field is excluded from the superconducting material. The phase diagrams illustrating this differing behaviour are shown in Figure 2.4.

Type-I superconductivity is present in most elemental metals such as mercury, aluminium or lead, with critical temperature values typically below 10 K. When cooled below its critical temperature, T_C, a type-I superconductor undergoes a first-order phase transition, which is accompanied by the expulsion of magnetic fields from the interior of the superconductor (the Meissner state) and by the vanishing of the material electrical

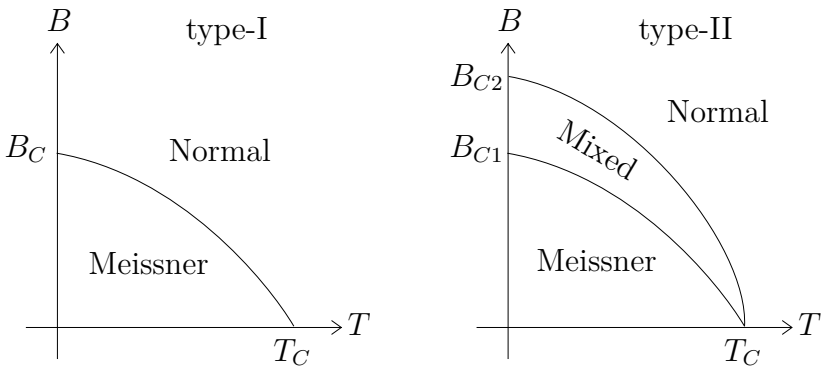

Fig. 2.4 The superconducting phase diagram of type-I (left) and type-II (right) superconductivity.

resistance. The magnetic field expulsion is due to the flow of lossless electric currents (supercurrents) in the field-penetrated region in the periphery of the superconductor.

The superconducting state can exist only at sufficiently small applied external fields - the superconductor is driven normal if the external field is increased above a temperature dependent limiting value, called the critical field, $B_C = \mu_0 H_C$. This is due to the superconducting energy at fields above the critical field being larger than the equivalent magnetic energy in the normal state. Since initially $\mathbf{B} = 0$ in the superconductor, it follows $\mathbf{M} = -\mathbf{H}$. The superconducting energy up to B_C, then, can be written as

$$\int_0^{B_C} M dB = -\int_0^{B_C/\mu_0} \mu_0 H dH = -\frac{B_C^2}{2\mu_0}. \tag{2.28}$$

Then, the definition of B_C becomes

$$\frac{B_C^2}{2\mu_0} = f_N - f_S, \tag{2.29}$$

where f_N and f_S are the free energy per unit volume of the normal and superconducting state, respectively.

Equivalently, there exists a maximum current, called the critical current, I_C, that can flow through the superconductor before superconductivity is suppressed. The equivalence for a long and thin wire of radius r is given by Silsbee' rule [19]

$$B_C = \frac{\mu_0 I_C}{2\pi r}. \tag{2.30}$$

The two parameters – the critical temperature and the critical magnetic field – confine the superconducting phase space to what we see in Figure 2.4 (left). Above B_C or above T_C the material transitions from the superconducting to the normal phase.

A second form of superconductivity, called type-II superconductivity, is present in some of the most technologically useful materials, such as NbTi or Nb_3Sn, or high temperature superconductors like $YBa_2Cu_3O_{7-\delta}$ (see Section 2.3). These materials are useful because in type-II superconductors the magnetic field can penetrate the material without suppressing superconductivity, which allows for significantly higher values of critical field and critical current.

At magnetic fields lower than the first critical field B_{C1} (equivalent to B_C in type-I superconductors) the superconductor is in the Meissner state with magnetic fields penetrating up to the London depth. Below B_{C1} the phase diagram for both types of superconductivity is identical. Increasing the magnetic field above B_{C1}, however, leads to a phase in which superconductivity coexists with the normal phase, called the mixed state (see Section 2.2.4). Then, if the magnetic field is raised further, above a second critical field B_{C2}, superconductivity is suppressed and the material is driven normal. The type-II superconductivity phase diagram is shown in Figure 2.4 (right).

In order to characterise superconducting materials into type-I or type-II a second characteristic length scale, besides the London penetration depth, has to be considered. This is the superconducting coherence length, ξ. This is a characteristic length, given by the Ginzburg-Landau theory [20, 21], which determines the scale over which the charge carrier density in the superconductor decays to zero (in contrast to the London penetration depth, which itself determines the scale over which the magnetic field decays to zero). In (RE)BCO superconductors the coherence length is on the order of $\approx 1\,\text{nm}$ [12] and is anisotropic depending on its direction in the crystal. The ratio of the two length scales, the Ginzburg-Landau parameter $\kappa = \lambda_L/\xi$, can be used to classify whether a superconductor is type-I or type-II. For type-I $\kappa < 1/\sqrt{2}$ and for type-II $\kappa > 1/\sqrt{2}$.

The Ginzburg-Landau theory of superconductivity built on Landau's theory of second order phase transitions [22] to describe the transition of normal matter into the superconducting state. In general, Landau's theory describes the free energy of a system as a polynomial function of some order parameter, which is chosen so that its value is finite below the transition and zero above it. For a superconductor this order parameter is the Cooper pair wave function, ψ, for which $|\psi|^2 = n_S$, the Cooper pair density. Based on this formulation the Ginzburg-Landau theory predicts the two characteristic lengths, λ_L and ξ. Their ratio, the parameter κ has to do with the surface

energy between the normal and the superconducting state. If $\kappa > 1/\sqrt{2}$, the surface energy becomes negative, making it favourable to form a large number of normal domains within the superconductor. Abrikosov showed [11] that the most energetically efficient configuration would take the form of a triangular lattice of normal filaments inside the superconductor. This state of coexisting superconducting and normal matter is known as the mixed state and the normal filaments are known as flux vortices.

2.2.4 Flux vortices and flux pinning

In the mixed state the magnetic field penetrates the superconductor in the form of flux vortices (also Abrikosov vortices [11]). These are thin filaments of normal material, surrounded by circulating current and each carrying a flux quantum, $\Phi_0 = h/2e_0$ (h is the Planck constant, e_0 the electron charge). Each flux vortex behaves as a magnetic field line; the number density of flux vortices, ρ_B, is directly related to the local magnetic field density by

$$\rho_B = \frac{B}{\Phi_0}. \tag{2.31}$$

Since each vortex is essentially a vortex of current, the distribution of vortices in a material determines the macroscopic current density flowing through the material.

Flux vortices in the mixed state repel each other if they are of the same sense (current circulating in the same direction), and attract each other if of the opposite sense. Additionally, a flux vortex can interact with the defects in the material lattice, and can be subjected to random thermal forces. The Langevin equation describing vortex movement can be written as [23]

$$\eta_v \mathbf{v} = \mathbf{F}_L + \mathbf{F}_P + \mathbf{F}_{th}, \tag{2.32}$$

where η_v is the vortex flow viscosity, $\mathbf{F}_L = \mathbf{J} \times \mathbf{B}$ is the Lorentz force, $\mathbf{F}_P$ is the pinning force, and $\mathbf{F}_{th}$ is the thermal actuation force.

Without thermal fluctuations and without any interaction between vortex and superconductor the only acting force would be the Lorentz force, $\mathbf{F}_L$. This is the repulsive or attractive vortex-vortex interaction and is the consequence of the magnetic energy stored in a distribution of flux vortices.

Next, the introduction of the vortex-matter interaction leads, firstly, to flux flow viscosity, η_v. Flux vortices are filaments of normal material, hence their movement through the superconducting matrix requires energy - vortex movement leads to dissipation. This dissipation can be accounted for by considering the loss due to the

flow of supercurrent through the normal vortex core as a consequence of its movement (the Bardeen-Stephen model [24]). When all the forces on the right hand side of equation 2.32 are evaluated the resultant leads to vortex flow and to dissipation.

Vortex flow dissipation presents a stark contrast to the situation in type-I superconductors, in which the current flow is lossless. In type-II superconductors in the mixed state, any change in the magnetic field will – through the movement of flux vortices – lead to dissipation. For practical application purposes this is not desirable as dissipation leads to losses and, hence, to a lower utility of applications that employ type-II superconductors. Therefore, it is desirable to impede vortex movement by introducing barriers, called pinning centres, into the superconducting matrix. Pinning centres are typically imperfections, irregularities or inclusions [25] purposefully engineered into the superconducting matrix during the manufacturing process (see Section 2.3.2). Physically, pinning centres are areas of normal material that act as potential wells, in which flux vortices get trapped due to a reduction of the total free energy of the system if the vortex normal core and the normal pinning centre overlap. The contribution of the pinning centres in the Langevin equation is summed up under the pinning force term, $\mathbf{F}_P$.

The final term in equation 2.32 is the thermal actuation force, $\mathbf{F}_{th}$. This force is a consequence of random thermal fluctuations felt by the flux vortices and leads to an Arrhenius type time evolution of the flux vortex distribution. For instance, if the Lorentz force and the pinning force are equal and opposite the flux vortex will be pinned in place. Then, if the vortex is acted upon by an additionall (small) thermal force, it may become unpinned and escape the superconductor. This process, known as flux creep, leads to a slow decay of current over time in type-II superconductors (see Section 2.2.6).

2.2.5 The Bean critical state model

As mentioned in the previous section, it is desirable to introduce pinning centres to the superconductor so as to impede vortex movement and mitigate dissipation. Type-II superconductors with sufficiently many such pinning centres are sometimes referred to as hard superconductors. Despite the generally complex equation governing vortex movement, there exists a simple model – the Bean critical state model [6] – with which the behaviour of hard superconductors can be explained.

The introduction of pinning centres to the superconducting material leads to hysteresis in the dependence of the current density in the superconductor on applied magnetic field - the change in current with a change in magnetic field depends on the

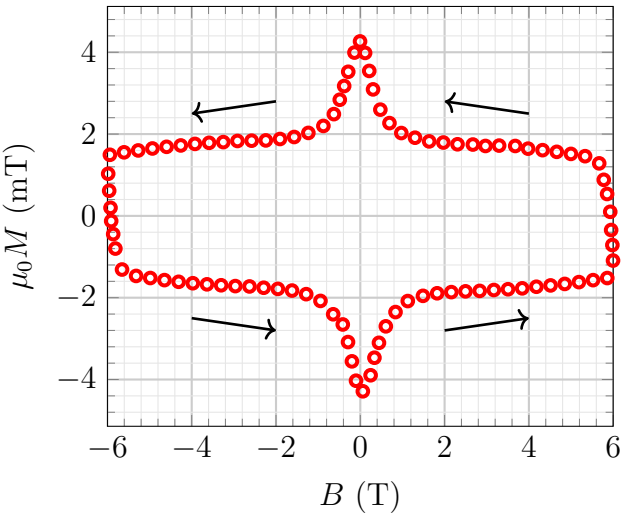

Fig. 2.5 A magnetisation loop of a $GdBa_2Cu_3O_{7-\delta}$ sample at 50 K. The arrows show the direction of the loop as the magnetic field is cycled. Reproduced with permission from Yunhua Shi (unpublished).

magnetic history of the superconductor. Equivalently, pinning centres lead to hysteresis in the magnetisation loops of these materials. A characteristic magnetisation loop for $GdBa_2Cu_3O_{7-\delta}$ is shown in Figure 2.5.

Superconductors are diamagnetic materials, meaning that the direction of induced currents in the superconductor will be such that the resultant magnetic field opposes the change in external magnetic field. At small (positive) applied fields this is seen in the negative value of magnetisation. Due to the flux pinning and consequent irreversibility, however, the magnetisation can become positive once the applied magnetic field is reversed.

The Bean critical state model explains this by making two assumptions about the behaviour of the superconductor:

1. There exists a maximum current density that can flow through the superconductor, the critical current density, J_C.

2. Any electromotive force applied to a superconductor will induce the full critical current density.

These two assumptions follow naturally from the Langevin equation for flux vortex flow if the pinning force, $\mathbf{F}_P$, is assumed to be sufficiently large, so that the thermal actuation force, $\mathbf{F}_{th}$, can be neglected, and there can be no flux vortex movement, such

that $\eta_v \mathbf{v} = 0$. Then, what remains is

$$\mathbf{F}_L + \mathbf{F}_P = \mathbf{J}_C \times \mathbf{B} + \mathbf{F}_P = 0. \tag{2.33}$$

Equation 2.33 is the definition of critical current density. The Bean model assumptions state that if there is any current flowing through the superconductor it must be the full J_C. Bean first formulated his model for a critical current density independent of magnetic field - this was later extended to take into account the observed decrease of current density with increasing magnetic field. For instance, the Kim model [26] assumes $J_C \propto 1/B$, which explains the shape of the magnetisation hysteresis remarkably well.

As an example let us consider the magnetisation hysteresis of an infinite cylinder of radius r_0, where the magnetic field B_0 is applied and cycled parallel to the cylindrical axis (z-direction). This is the so-called zero field cooled magnetisation procedure, which will be discussed further in Section 2.3.3. The two examples considered will be the Bean model, in which $J_C(B) = J_C^0$ is constant, and the Kim model, in which $J_C(B) = J_C^0/(1 + B/B_1)$, where J_C^0 and B_1 are constant parameters.

The magnetic field profiles inside the superconductor can be calculated using Ampere's law, $\nabla \times \mathbf{B} = \mu_0 \mathbf{J}_C$. The external magnetic field is applied along the cylindrical axis, hence the current is induced in the azimuthal direction, $\mathbf{J}_C(B) = \pm J_C(B)\hat{\mathbf{e}}_\phi$, where $\hat{\mathbf{e}}_\phi$ is the unit vector in the azimuthal direction. Since the cylinder is assumed infinite in the z-direction the only non-zero field component will be parallel to the cylindrical axis (due to cylindrical symmetry). Then, Ampere's law simplifies to the onedimensional form

$$\frac{\partial B}{\partial r} = \pm \mu_0 J_C(B), \tag{2.34}$$

where the sign on the right hand side depends on the direction of change of the applied field. In general, the currents will be induced so as to oppose any change in the external magnetic field. The integration of equation 2.34, along with the boundary condition $B(r = r_0) = B_0$, leads to the field profiles, shown in Figure 2.6 and the corresponding current density is shown in Figure 2.7 (Bean model in red, Kim model in blue).

When the external magnetic field is first increased shielding currents are induced in the sample periphery. The magnitude of the currents determines the magnetic field gradient inside the superconductor as per equation 2.34. Hence, the magnetic field decreases with distance until it reaches zero at a depth

$$\lambda_B = \frac{B_0}{\mu_0 J_C}, \tag{2.35}$$

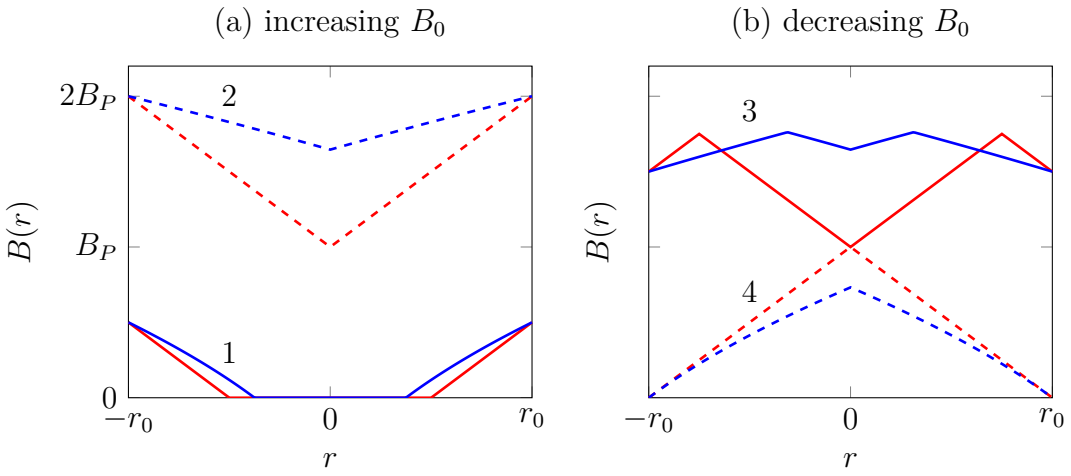

Fig. 2.6 The magnetic field profile inside the superconductor during the (a) increasing and (b) decreasing portion of the applied field B_0 (Bean model red, Kim model blue). The applied field at points 1, 2, 3, and 4 are, respectively, $B_P/2$, $2B_P$, $1.5B_P$, and 0. The values of magnetisation for each of the four applied fields are shown in Figure 2.8.

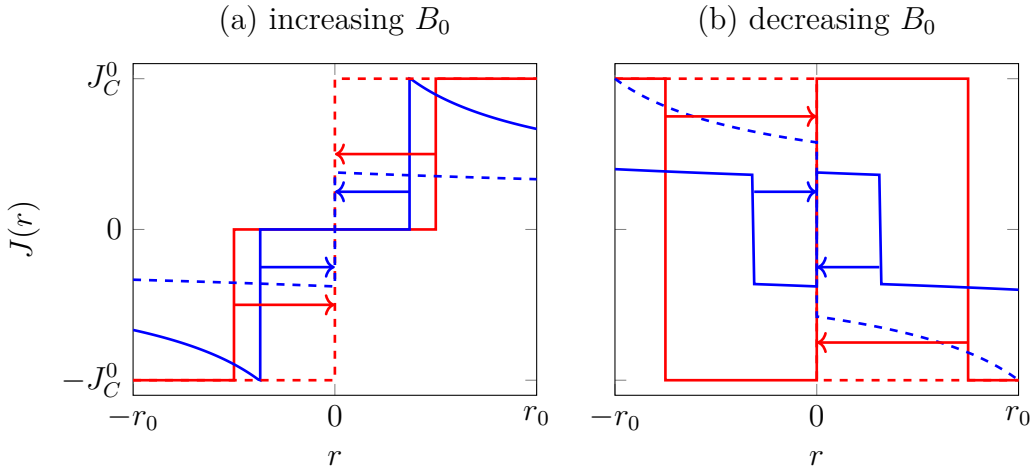

Fig. 2.7 The current distribution inside the superconductor during the (a) increasing ($0.5\,\mathrm{T} \rightarrow 2\,\mathrm{T}$) and (b) decreasing ($1.5\,\mathrm{T} \rightarrow 0\,\mathrm{T}$) portion of the applied field B_0, corresponding to the magnetic field profiles in Figure 2.6. Red lines are the Bean model, blue the Kim model.

called the Bean penetration depth. This is the depth up to which currents are induced when a magnetic field of amplitude B_0 is applied. In the case of the Kim model, in which the value of the critical current density varies with magnetic field, the slope of $B(r)$ inside the superconductor will not be constant, instead its value will be determined by the local magnetic field density. And, since the value of J_C was chosen to decrease with increasing magnetic field, the penetration depth in the Kim model will be greater than in the Bean model (Figure 2.6, blue lines).

The applied field, at which the Bean penetration depth becomes equal to the radius of the sample, is called the penetration field, B_P. Once the magnetic field is increased up to B_P the superconductor is fully penetrated and the induced currents circulate in the entirety of its cross section. In the framework of the Bean model with constant J_C, the magnetisation at this point reaches its maximum (absolute) value and remains unchanged until the external magnetic field starts decreasing (see Figure 2.8, below).

When the applied magnetic field is ramped down from its maximum value the irreversible behaviour begins to take place and there appears hysteresis in the magnetisation loop. This is because the gradient of the magnetic field inside the superconductor is $\pm\mu_0 J_C(B)$ and so the change in applied field in the decreasing portion of the ramp needs to be twice the value (for constant J_C) in the increasing portion of the ramp for the same Bean penetration depth λ_B. This leads to a non zero current density distribution in the superconductor even when the external field has reached zero.

The magnetisation of the superconductor can be calculated from the current distribution similarly to the magnetic field profile, with the equation

$$\nabla \times \mathbf{M} = \mathbf{J}. \tag{2.36}$$

The boundary condition, here, must be $M(r = r_0) = 0$, as the magnetisation is zero outside the superconductor. Then, the total magnetisation can be calculated as the cross section average of the local magnetisation. The resulting magnetisation as a function of applied field is shown in Figure 2.8.

A common practical application of the Bean model is determining the critical current density of a superconducting sample, J_C, and its dependence on magnetic field and temperature. This is done by measuring the magnetisation loop at a given temperature and calculating the current density by equation 2.36. As an example, the current distribution in a fully magnetised cubic superconducting sample of dimensions $2a \times 2a \times 2a$ is shown schematically in Figure 2.9.

The sample dimensions are typically chosen to be small so that the applied field will be larger than the penetration field. The current density can be assumed constant

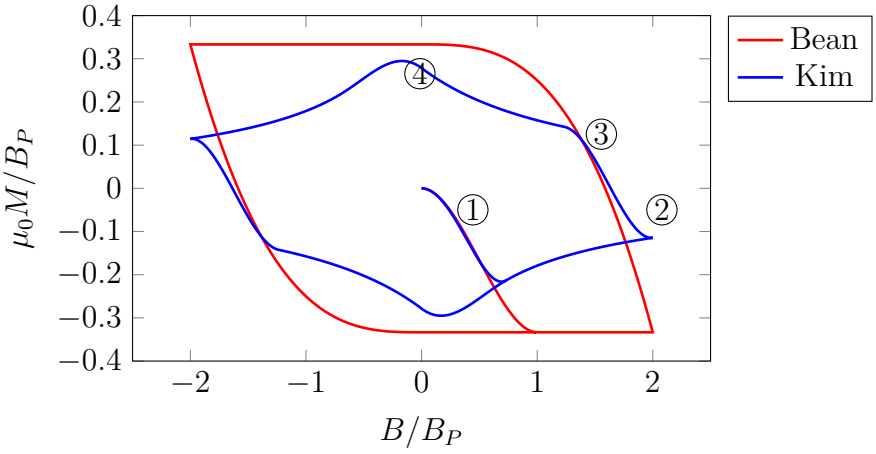

Fig. 2.8 Magnetisation loops for the Bean and Kim models. The applied field at points 1, 2, 3, and 4 are, respectively, $B_P/2$, $2B_P$, $1.5B_P$, and 0. The corresponding magnetic field profiles are shown in Figure 2.6.

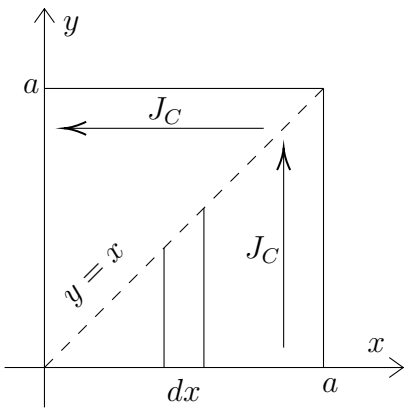

Fig. 2.9 The current distribution in a fully magnetised rectangular sample of side length $2a$.

throughout the sample and the magnetisation can be calculated as

$$M = \frac{1}{2V} \int \mathbf{r} \times \mathbf{J} \, dV. \tag{2.37}$$

Due to symmetry the integral can go over an eighth of the cubic sample (i.e. the cross-sectional area below the dashed line in Figure 2.9). Then,

$$M = 4 \frac{1}{2\,(2a)^3} \int_{x=0}^{x=a} \int_{z=-a}^{z=a} x J_C \,(x \, dx) \; dz = \frac{a J_C}{6}. \tag{2.38}$$

Assuming the value of magnetisation changes sign when the applied field changes sign, the width of the magnetisation loop $\Delta M = 2M$ can be used to determine the critical current density as

$$J_C = 3 \frac{\Delta M}{a}. \tag{2.39}$$

A characteristic $J_C(B, T)$ dependence for $GdBa_2Cu_3O_{7-\delta}$ bulk superconductors, extracted from magnetisation loop measurements with the help of equation 2.39, is shown in Figure 2.10. Since the pinning force decreases with applied magnetic field, this manifests itself in the field dependence of J_C. However, the value of J_C does not decrease monotonically with increasing field; instead there appear broad peaks where J_C reaches a local maximum. This is the so-called matching or fishtail effect [27] and occurs because the density of pinning centres matches the density of flux vortices ρ_B.

The magnetic field, at which the critical current density reaches a sufficiently low value, typically agreed to be $100\,\mathrm{A\,cm^{-2}}$ [29], is called the irreversibility field, B_{irr}. The irreversibility field represents a practical limit for the usability of type-II superconductors and is typically significantly lower than the second critical field B_{C2}.

It can also be seen from Figure 2.10 that J_C increases markedly with decreasing temperature, e.g. an order of magnitude between the temperatures 70 K and 40 K. For this reason most practical applications aim to employ superconductors at temperatures significantly below T_C at which the achievable current densities and trapped fields become significantly increased.

The Bean model, while being able to capture the hysteretic behaviour in the magnetisation loop, quantitatively differs from the real picture in Figure 2.5. The Kim model, with the field dependent critical current density, captures the real behaviour much more accurately. The framework of the Bean model and its extensions has become extremely useful in interpreting the behaviour of hard superconductors. However, as is the case with most physical models, the Bean model is merely a simplification of the physical picture and breaks down beyond the domain of its validity. For instance, as it

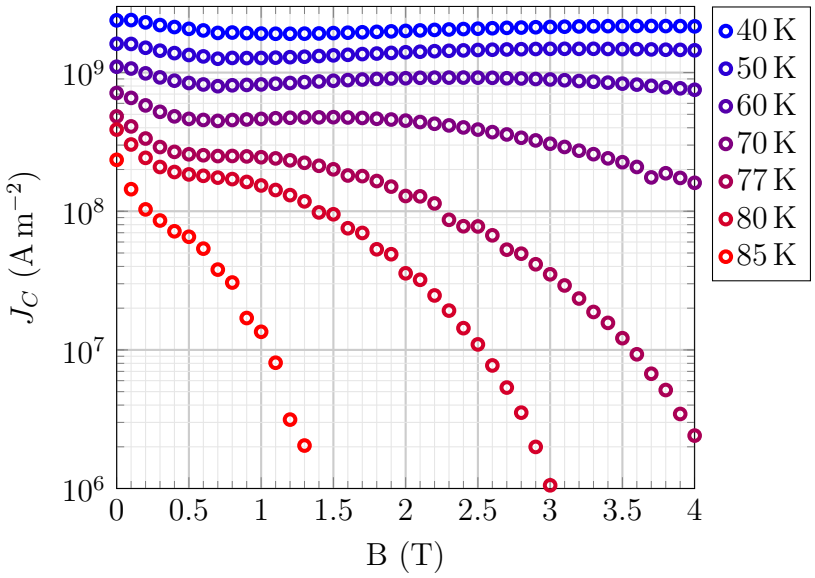

Fig. 2.10 The $J_C(B)$ dependence of a $GdBa_2Cu_3O_{7-\delta}$ superconductor, calculated from measured magnetisation loops using equation 2.39. Reproduced from [28].

assumes a large pinning force in comparison to the thermal actuation force, it does not take into account the thermal unpinning of flux vortices. This phenomenon, known as flux creep, can be especially significant in high temperature superconductors.

Additionally, the Bean model assumes that any Lorentz force will induce the full critical current density to flow through the superconductor. In reality, the flux vortices are held in place by pinning centres of finite size, which are essentially potential wells of finite depth. Hence, a sufficiently small Lorentz force will not displace the vortices from their pinning sites; it will instead cause vortex oscillation within the well without dissipation. This is the so called Campbell penetration, which becomes relevant at sufficiently small magnetic fields. These limitations of the Bean model will be discussed in Sections 2.2.6 and 2.2.7, respectively.

2.2.6 Flux creep

A commonly observed phenomenon in high temperature superconductors is a logarithmic decay of transport currents due to thermal activation of flux vortices from their pinning sites, or flux creep [30]. This phenomenon is more apparent in high-temperature superconductors because the thermal energy, k_BT (where T is the temperature and k_B is the Boltzmann constant), can be significantly larger than in low temperature superconductors due to higher values of T_C. Consequently, the thermal actuation force,

$\mathbf{F}_{th}$ in equation 2.32, can no longer be neglected and flux creep cannot be described within the Bean model framework. Anderson and Kim proposed a mechanism for this decay based on a random unpinning of flux vortices due to thermal oscillations [31].

In the presence of a stochastic thermal force a distribution of pinned flux vortices will oscillate randomly, each vortex within its respective pinning centre. At random time intervals a vortex will become unpinned and subsequently escape the superconductor. The rate of this process will be determined by the depth of the effective pinning potential, U, compared with the thermal energy $k_B T$.

To derive a governing equation for this decay we start with a current distribution inside the superconductor as a function of time

$$J(t) = \frac{1}{\mu_0}\frac{\partial B(x,t)}{\partial x}, \tag{2.40}$$

where $\partial B(x,t)/\partial x$ is the local magnetic field gradient at a time t. The local magnetic field can be expressed in terms of the number of flux vortices per unit area, dN_B/dS as

$$B = \frac{\rho_B}{\Phi_0} = \frac{1}{\Phi_0}\frac{dN_B}{dS}. \tag{2.41}$$

The rate of change of N_B due to random unpinning can then be obtained from the Arrhenius creep rate equation [32],

$$\frac{dN_B(t)}{dt} = -N_0\omega_0 e^{(-U/k_B T)}, \tag{2.42}$$

where N_0 is the number of flux vortices at time $t = 0$ and ω_0 is a characteristic rate of vortex unpinning. Hence, we can write the initial current density as

$$J_0 = \frac{1}{\mu_0\Phi_0}\frac{\partial}{\partial x}\frac{dN_0}{dS} \tag{2.43}$$

and, taking the time derivative of equation 2.40, we arrive at the expression for decay

$$\frac{dJ}{dt} = -J_0\omega_0 e^{(-U/k_B T)}. \tag{2.44}$$

At this point the form of the pinning potential U must be chosen in order to calculate the time dependence of the current density. In general the effective pinning potential will be a decreasing function of current density. When the value of the current density is J_C the Lorentz force will be equal and opposite the pinning force (equation 2.33). Hence, the effective pinning potential will be zero (e.g. if we further increase the

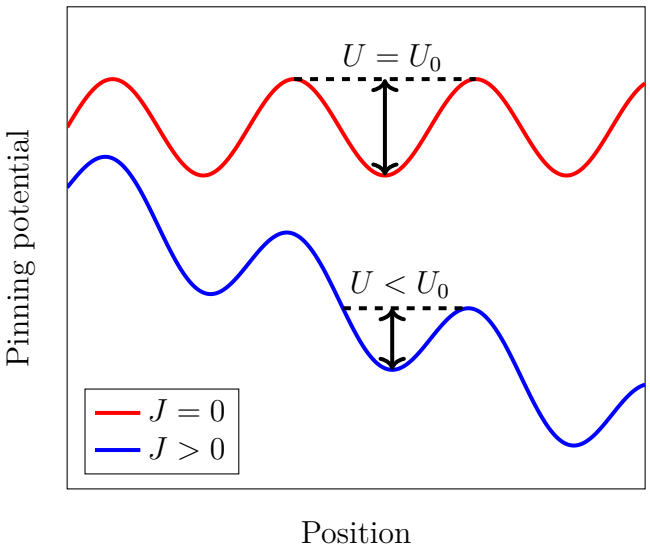

Fig. 2.11 The tilted washboard potential representing the effective pinning potential for a varying current density.

Lorentz force the flux vortex will become unpinned). If the current is lowered below J_C the Lorentz force decreases and the effective pinning potential increases. This behaviour can be represented schematically by the tilted washboard potential, as shown in Figure 2.11.

Initially Anderson and Kim proposed a linearly decreasing pinning potential with current, which leads, upon integration of equation 2.44, to a logarithmic decay of current over time, consistent with observations. Subsequent measurements of the pinning potential dependence on current [33] have shown that in some cases the pinning potential does not decrease linearly with current, instead the dependence is logarithmic,

$$U \propto \log J. \tag{2.45}$$

Substituting this expression into equation 2.44, integrating, and comparing the result to the value of resistivity given by the Anderson flux creep theory [30], we arrive at a power-law relation between the electric field and current density

$$E = E_0 \left(\frac{J}{J_C} \right)^N, \tag{2.46}$$

where the exponent $N = U_0/k_B T$. Equation 2.46, typically referred to as the E-J power law, is a useful approximation for the relation between the electric field and the current density and is commonly used in numerical simulations to model the resistivity

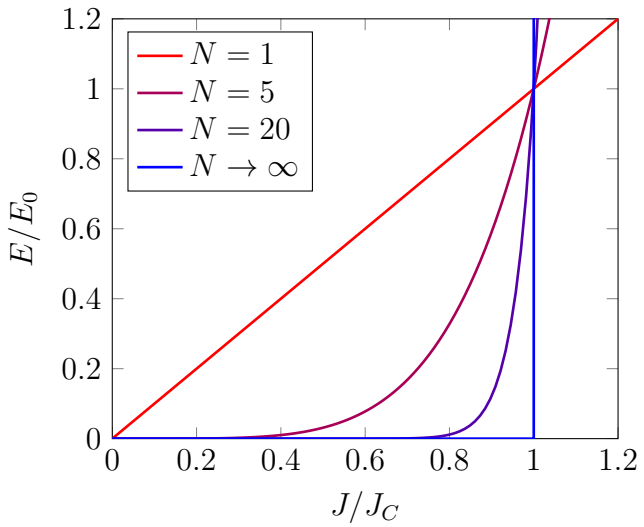

Fig. 2.12 The E-J power law for a varying exponent N. The value $N = 1$ represents Ohm's law, and $N \to \infty$ represents the Bean model.

of a superconducting material. This is because the value of the parameter N can be tuned to describe anything from normal matter (the E-J power law for $N = 1$ is simply Ohm's law) to an ideal hard superconductor (for $N \to \infty$ the power law approaches the Bean model). Between the two extremes the value of N determines the flux creep rate of a superconductor. For good quality superconductors with a low rate of creep a typical value is $N = 20$, whereas lower values in the range of $N = 5$ represent a higher creep rate. In practice it can be difficult to justify any particular choice of N because the creep rate will depend on the temperature, the magnetic history of the superconductor, the applied magnetic field, and the rate at which the applied magnetic field is changed. Moreover, the measurement of N as a function of all the mentioned parameters can be difficult. Hence, the value of N used in numerical simulations is typically chosen such that the simulated rate of decay due to flux creep at self-field (zero applied magnetic field) matches the measured rate of decay [34, 35]. The shape of the E-J power law for different values of the exponent N is shown in Figure 2.12. It can be seen that increasing the value of N leads to a higher electric field at current densities below J_C. Hence, the total losses $Q = \mathbf{E} \cdot \mathbf{J}$ will be higher for lower values of N.

2.2.7 The Campbell model

As mentioned in Section 2.2.5 the Bean model neglects the finite size of pinning centres and consequently it breaks down if the applied electromotive forces acting on the flux vortices are sufficiently small so as not to displace the vortices from their pinning centres. Campbell proposed an alternative model [8, 36] in which the pinning force is not constant (equal end opposite the Lorentz force) for all vortex displacements; instead, for small displacement the force is proportional to the displacement (Hooke's law). At small displacements the flux vortex response is assumed linear and without dissipation. Hence, within the framework of the Campbell model, the calculated hysteretic losses will be lower than those predicted by the Bean model.

The purpose of the following paragraphs will be to derive a dynamic equation for flux motion due to external time varying magnetic fields within the Campbell model. Hence, the magnetic field profile, the total flux, and the induced voltage (as the time derivative of the flux) will be calculated. Since the induced voltage itself is easily measurable with pick-up methods, the Campbell model will provide a convenient method of measuring flux vortex movement on a nanometre scale.

To analyse the effect of finite pinning centres let us consider, firstly, the mixed state in a uniform magnetic field B_0 (Figure 2.13 (top)). Since the magnetic field is assumed constant throughout the superconductor the vortex density will be constant as well. The vortex spacing in the x-direction can be written as

$$a = \frac{\Phi_0}{B_0 l}, \tag{2.47}$$

where l is the vortex spacing perpendicular to the x-direction (in the subsequent discussion l will be kept constant, whereas a will be made to change). A small vortex displacement from its equilibrium position will lead to a local perturbation of magnetic field $b(x)$ (we use lower case letters to emphasise $b(x) \ll B_0$). We write the local vortex displacement from the equilibrium position as $y(x)$ (Figure 2.13 (bottom)). Hence, the new vortex spacing at x can be written as

$$a' = a + y(x + a) - y(x). \tag{2.48}$$

The right hand side of the above equation can be approximated with a derivative (provided the vortex spacing a is much smaller than the scale over which y varies), as

$$a' = a\left(1 + \frac{dy}{dx}\right). \tag{2.49}$$

Then, the resultant local magnetic field can be written as

$$B' = B_0 + b(x) = \frac{\Phi_0}{a'l} = B_0 \frac{1}{1 + dy/dx} \approx B_0 \left(1 - dy/dx\right), \tag{2.50}$$

where we assumed $dy/dx \ll 1$. Dividing the above equation by B_0 we arrive at

$$\frac{b(x)}{B_0} = -\frac{dy}{dx}, \tag{2.51}$$

which is the relation between the local flux displacement and the local change in magnetic field, and describes flux conservation. As we shall see below, Campbell showed that a sufficiently small external AC magnetic field leads to an average vortex displacement from equilibrium, $y(x)$, which is largest just below the surface of the superconductor and decays with depth as

$$y(x) \propto \exp\left(-\frac{x}{\lambda_C}\right). \tag{2.52}$$

Here, λ_C is the Campbell penetration depth and is determined by the effective size of the pinning centres, i.e. the maximum reversible displacement d of the flux vortices from their equilibrium positions.

To show how the pinning force F_P determines vortex displacement we start with the force balance equation for a single vortex

$$F_P = F_L, \tag{2.53}$$

where $F_L = \mathbf{J}(x) \times \mathbf{B}_0$ is the local Lorentz force per unit volume. Writing the current density $\mathbf{J}(x)$ in terms of the magnetic field gradient via Ampere's law, the force balance equation reads

$$F_P = -\frac{B_0}{\mu_0} \frac{db(x)}{dx}. \tag{2.54}$$

Then, the magnetic field gradient can be expressed in terms of the vortex displacement, $y(x)$, by derivating the flux conservation equation 2.51 and substituting into the above equation, which gives

$$F_P = \frac{B_0^2}{\mu_0} \frac{d^2y}{dx^2}. \tag{2.55}$$

Equation 2.55 determines how the pinning force affects the vortex displacement and applies more generally than just in the framework of the Campbell model. For instance, in the Bean model framework the pinning force is constant and equal in size to the

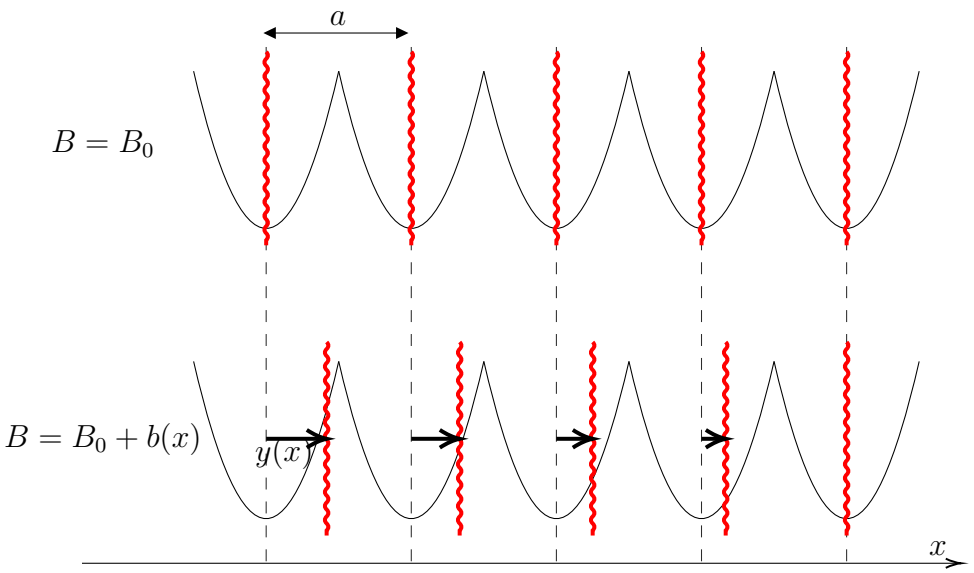

Fig. 2.13 Top: a constant distribution of pinned flux vortices (red wavy lines) corresponds to a constant magnetic field B_0. Bottom: a vortex displacement $y(x)$ from its equilibrium position in the pinning potential leads to a local change in magnetic field, $b(x)$.

Lorentz force,

$$F_P = \pm B_0 J_C. \tag{2.56}$$

Substituting this expression into equation 2.55 and integrating once, the magnetic field profile becomes

$$b(x) = -B_0 \frac{dy}{dx} = \mp \mu_0 J_C x + \text{const.}, \tag{2.57}$$

which is identical to the result for $b(x)$ in the Bean model framework, calculated with Ampere's law $\nabla \times b(x) = \mu_0 J_C$.

The Campbell model expands on the Bean model to include the possibility of reversible vortex movement for small displacements $y(x)$ from equilibrium. This expansion is done by modifying the pinning force to include a linear region at small displacements and to transition to a constant value at large displacements. The physical justification for the linear region is that regardless of the overall shape of the pinning potential, locally in the vicinity of its minimum it can be approximated by a harmonic potential. Then, if the potential is quadratic in displacement, the force will be linear. Additionally, the choice of pinning force must capture the irreversible behaviour of the Bean model at large displacements – for large values of $y(x)$ the pinning force must approach $\pm B_0 J_C$, where the sign is determined by the direction of change of $y(x)$.

In the virgin state – before any change in the external field, when all the vortices are in their equilibrium positions – a commonly employed [37–40] candidate dependence of pinning force F_P on local displacement $y(x)$ is

$$F_P(y(x)) = B_0 J_C \left(1 - \exp\left(-\frac{y(x)}{d}\right)\right). \tag{2.58}$$

Here, d represents the maximum reversible displacement before the vortex becomes displaced from the pinning centre (effectively, d is the radius of the pinning potential). For small vortex displacements $y(x) \ll d$ the exponential can be approximated by a linear function as

$$F_P \approx B_0 J_C \left(1 - \left(1 - \frac{y(x)}{d}\right)\right) = \frac{B_0 J_C}{d} y(x) = \alpha_L y(x), \tag{2.59}$$

where we introduced the Labusch parameter α_L, the curvature of the pinning potential at its minimum [41]. The pinning force defined by equation 2.58 is linear for small displacements, hence it is a suitable candidate to describe reversible vortex movement. Additionally, at large displacements $y(x) \gg d$ its value approaches $B_0 J_C$, which is the pinning force in the Bean model framework.

To account for hysteresis due to a cycling external field let us consider a vortex that has been displaced a distance $y_0 \gg d$ from its equilibrium position when the magnetic field is reversed. The pinning force just before the reversal will be $F_P \approx B_0 J_C$ and must transition to $F_P \approx -B_0 J_C$ at $y = -y_0$. Additionally the slope of the force just after the reversal must be identical to the initial slope in the virgin state – its value will be determined by the curvature of the pinning potential α_L. Hence, for the hysteresis force curve the dependence 2.58 may be used with both axis scaled by a factor of two and with the origin moved to y_0. The hysteretic pinning forces can be expressed in terms of the virgin pinning force 2.58 as

$$F_P^{\pm} = \pm \left(2F_P(\frac{y_0 \pm y}{2}) - F_P(y_0)\right), \tag{2.60}$$

where the sign depends on whether the displacement is increasing (+) or decreasing (−). This is represented graphically in Figure 2.14.

To calculate the vortex displacement $y(x)$ at all times the hysteresis force term is substituted into the force balance equation 2.55, which can subsequently be integrated

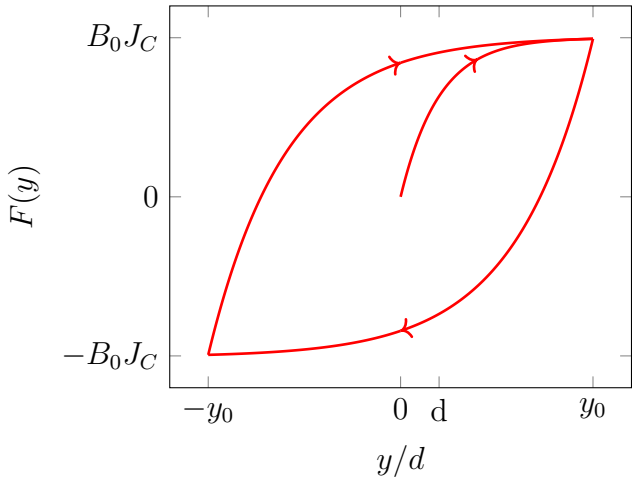

Fig. 2.14 The pinning force hysteresis in the Campbell model. The initial curve is $F_P(y)$ from equation 2.58. The two loop curves are $2F_P((y_0+y)/2) - F_P(y_0)$ (top) and $-\left(F_P((y_0-y)/2) - F_P(y_0)\right)$ (bottom). The slope at $y = 0$ is the same as at $y = y_0$, and is determined by the curvature of the pinning potential, α_L.

to obtain $y(x)$ and $b(x)$. For the initial virgin state the equation can be written as

$$\frac{B_0^2}{\mu_0}\frac{d^2y}{dx^2} = B_0 J_C \left(1 - \exp\left(-\frac{y(x)}{d}\right)\right) \tag{2.61}$$

The value of the Campbell penetration depth can be found by analysing the characteristic length scale of the above equation. By introducing the reduced variables $\tilde{x} = x/\lambda_C$ and $\tilde{y} = y/d$, the equation becomes

$$\frac{d^2\tilde{y}}{d\tilde{x}^2} = 1 - \exp\left(-\tilde{y}\right), \tag{2.62}$$

where

$$\lambda_C = \sqrt{\frac{B_0 d}{\mu_0 J_C}} = \frac{B_0}{\sqrt{\mu_0 \alpha_L}}. \tag{2.63}$$

The Campbell penetration depth is the characteristic distance over which a perturbation of magnetic field $b(x)$ decays due to the finite reversible movement of the flux vortices within their pinning centres. Its value is determined by the maximum reversible displacement d (provided the applied field B_0 and the critical current density J_C are known). Hence, the measurement of λ_C can be used to determine the effective size of the pinning centres in the superconductor. The Campbell field profiles, compared to those predicted by the Bean model, are shown in Figure 2.15. The profiles are

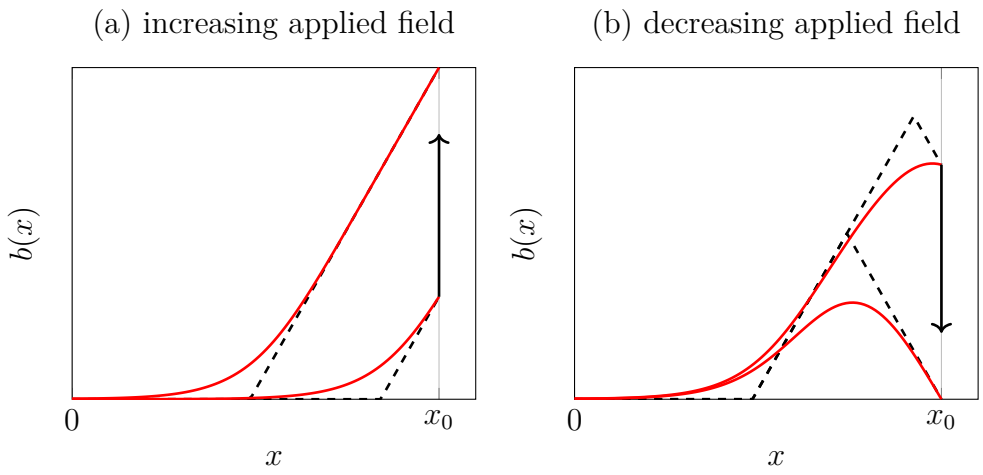

Fig. 2.15 The Campbell (red) and Bean (black, dashed) magnetic field profiles during the (a) increasing and (b) decreasing portion of the applied field. $x = 0$ is the centre of the superconductor and $x = x_0$ is the surface.

calculated by solving the differential equation for the vortex displacement $y(x)$, from which $b(x)$ is calculated with the flux conservation equation 2.51. The boundary conditions used are set such that the displacement at the centre of the superconductor is $y(x = 0) = 0$ (due to symmetry) and the field at the surface is equal to the applied field, $b(x = x_0) = B_{applied}$.

2.3 Bulk (RE)BCO superconductors

2.3.1 Crystal structure

Two increasingly important superconducting compounds are $YB_2Cu_3O_{7-\delta}$ (YBCO) and $GdB_2Cu_3O_{7-\delta}$ (GdBCO), both members of the (RE)BCO family (where RE is a rare earth or yttrium). The (RE)BCO family, discovered in 1986 [42], is significant because its member compounds exhibit record high values of T_C, such that they form part of a new group, called high temperature superconductors. YBCO and GdBCO, in particular, exhibit critical temperatures of $T_C = 92\,\mathrm{K}$ [43], which is, significantly, above the boiling temperature of liquid nitrogen and, as such, technologically important.

YBCO, along with the other members of the (RE)BCO family, has a tetragonal or orthorombic unit cell, shown in Figure 2.16. The crystal structure is defect perovskite, in which the oxygen concentration, denoted as $7 - \delta$, determines the shape of the unit cell and whether the compound is superconducting or insulating (notice the two

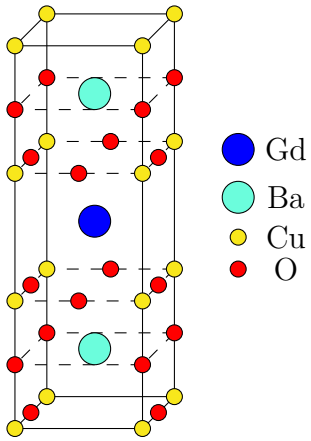

Fig. 2.16 The unit cell of $GdBa_2Cu_3O_{7-\delta}$. Here, $\delta = 0.5$. The Cu and O ions in the dashed line planes are in reality not exactly coplanar, instead they are slightly displaced in the c-direction. The dimensions are $a \approx b \approx 3.8\,\text{Å}$ and $c \approx 11.7\,\text{Å}$ (see text).

additional oxygen atoms on the bottom face of the unit cell in Figure 2.16, due to which $7 - \delta = 6.5$). When $\delta = 1$ the unit cell is tetragonal and the phase is not superconducting. The optimal concentration is $\delta = 0.07$, at which the compound is superconducting with a highest value of T_C and the unit cell is orthorhombic [44].

A characteristic feature of the crystal structure is its layered form that leads to anisotropic macroscopic observables. The two short axis of the primitive cell are commonly denoted as the a and b directions, whereas the long axis is the c direction. The typical side lengths of the primitive cell are, depending on the doping, $a \approx b \approx 3.8\,\text{Å}$ and $c \approx 11.7\,\text{Å}$ [44]. Hence, quantities such as the critical current density and the critical field typically exhibit cylindrical symmetry - their values in the ab-plane differ from their value in the c-direction. Importantly, the critical current density (at self-field, i.e. zero applied magnetic field) is highest in the ab-plane, which has to be taken into account when developing practical applications. As an example, bulk superconductors are typically grown such that the c-direction is perpendicular to the expected direction of induced currents, hence maximising the relevant J_C.

A possible practical form of (RE)BCO superconductors are bulk single grains. These are essentially (bulk) single crystals, i.e. three dimensional bodies of superconductor (as opposed to e.g. superconducting tapes or wires, which are thin in one or two dimensions). The term single grain is used instead of single crystal due to a high concentration of pores, inclusions and cracks, which interrupt the long range order formally required to define a single crystal. Bulk superconductors (bulks) are the only materials known today which offer high current carrying capabilities in all three

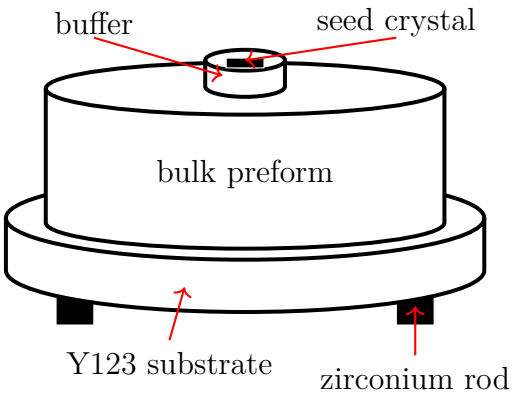

Fig. 2.17 A schematic illustration of the bulk preform prepared for heat treatment. A typical diameter of the bulk preform is 30 mm.

cardinal directions. This is especially useful for applications such as magnetic levitation [45], where it is of great importance that the current carrying capabilities be high in all the crystallographic directions so as to provide an opposing force to a displacement of a levitated object in any direction.

Another important application of bulks is as quasi-permanent trapped field magnets (more in Section 2.3.3). The high critical current densities, achievable in YBCO and GdBCO today offer pathways toward high values of trapped field. Since the bulks are typically on the order of 10 mm to 50 mm in size they offer a practical way towards high portable magnetic fields. Other notable applications include e.g. magnetic bearings, magnetic lenses, magnetic resonance imaging devices, drug delivery systems [46–49].

2.3.2 Manufacturing process

The most commonly employed method of manufacturing bulks is the top seeded melt growth (TSMG) technique [7, 50], where the growth of the superconducting matrix is nucleated by a seed crystal of a desired lattice parameter. Initially, the raw powder is pressed into a preform of a desired, commonly cylindrical, shape. In the case of YBCO the raw powder will consist of a mixture of $YBa_2Cu_3O_{7-\delta}$ (Y123) and Y_2BaCuO_5 (Y211), with possible additions of Ag_2O for improved mechanical strength and thermal conductivity [51]. The Y211 phase is non-superconducting and is added to Y123 to provide normal areas needed for flux pinning.

After pressing the preform is prepared for heat treatment in a configuration, shown in Figure 2.17. The seed crystal is placed at the centre of the top surface of the preform

from which the sample growth will nucleate during heat treatment. The seed crystal is typically a (RE)BCO thin film with a higher melting temperature than of the bulk to be manufactured (so that the seed crystal itself does not melt). If the bulk is made with the addition of Ag_2O a buffer pellet is placed between the seed crystal and the preform to protect the seed crystal from the silver, which can degrade the seed. The buffer is of the same composition as the bulk, but without the added Ag_2O. Then, the preform is placed onto an Y123 substrate, which has a lower melting temperature than the preform, hence it prevents nucleation from the bottom surface. Finally, this is placed on zirconium rods that are placed onto an aluminium oxide plate. The entire assembly is placed into a furnace for heat treatment.

The heat treatment temperature profile is designed to achieve peritectic decomposition of the bulk and subsequent solidification, based on the reaction [52]

$$2\,\mathrm{YBa_2Cu_3O_{7-\delta}} \xrightarrow{1080\,^\circ\mathrm{C}} \mathrm{Y_2BaCuO_5} + \mathrm{L(Ba_3Cu_5O_8)}, \tag{2.64}$$

where L denotes a liquid phase.

The bulk is initially heated to above the peritectic temperature, T_P, to achieve partial melting of the Y123 phase. Above T_P, which is between 1000 °C and 1080 °C for (RE)BCO, the Y123 phase decomposes into Y211 and a liquid phase $Ba_3Cu_5O_8$. The temperature is subsequently lowered slowly below T_P during which the liquid phase reacts with Y211 and recombines into a single Y123 phase. If the heat treatment is successful the result is a single grain bulk of mostly Y123 phase with uniformly distributed inclusions of the Y211 phase, providing pinning centres throughout the superconducting matrix. The bulk is not yet superconducting, however, due to an insufficient oxygen concentration. Hence, the final stage of the manufacturing process is bulk oxygenation, during which the bulk is heated to around 400 °C in an oxygen rich atmosphere. During the oxygenation process the oxygen stoichiometry is changed such that it approaches it optimum value at which the crystal structure is orthorhombic and the material superconducting.

Superconducting bulks can be used as trapped field magnets, provided there exist a means to induce transport currents to circulate inside the bulk. For an infinite cylinder of radius r_0, in which a current density of magnitude J_C is flowing in the azimuthal direction, the trapped field at the centre can be calculated using the Biot-Savart law as

$$B = \mu_0 J_C r_0. \tag{2.65}$$

Hence, it is desirable to manufacture single grain bulks of large radii in order to maximise the achievable trapped field. However, due to the nature of the manufacturing process, during which the single grain grows from the seed crystal outwards, it becomes increasingly difficult to produce larger bulks. They typically show deteriorated superconducting properties, such as lower values of T_C and J_C, as compared with smaller bulks. Thus, there exists a trade-off between manufacturing a larger bulk and a bulk with superior superconducting properties.

2.3.3 Magnetisation methods

There exist two conventional methods of inducing a circulating transport current in the superconductor (i.e. magnetisation techniques): zero field cooled magnetisation (ZFC) and field cooled magnetisation (FC). Both are shown schematically in Figure 2.18.

With ZFC the magnetisation is induced by cycling an external magnetic field from zero to a maximum value and back to zero while the temperature is kept below T_C. This is essentially represented by the first and second quadrants of the magnetisation loop in Figure 2.8. To achieve a fully magnetised bulk, i.e. a bulk in which the current circulates through the entire cross-section, the maximum value of the applied field must be at least twice as high as the penetration field for a particular sample.

With FC the magnetisation is induced by first ramping the magnetic field to its maximum value when the temperature of the bulk is above T_C, so that the bulk is not superconducting. The applied field is then kept at its maximum value and the bulk is cooled below T_C in field. Subsequently, the applied field is ramped back to zero. For the FC technique the maximum applied field need only be as high as the penetration field, half what is needed with the ZFC technique. However, the applied field must be held at its maximum value for the time needed to cool down the bulk.

Both techniques necessitate a low ramp rate of the applied field once the bulk is superconducting so as to prevent heating of the bulk. The electric field induced in the superconductor is, per Faraday's law, proportional to the ramp rate of the magnetic field. Hence, the loss $Q = \mathbf{E} \cdot \mathbf{J}$ and the temperature rise ΔT are proportional to the ramp rate. For this reason both techniques require a long time and a lot of power to magnetise the bulk (depending on the maximum applied field and on the temperature at which the bulk is kept).

The highest trapped field achieved to date in a bulk superconductor is 17.6 T between a stack of two 25 mm diameter GdBCO bulk superconductors [5]. This trapped field was achieved using a superconducting magnet and the FC technique. The applied field was initially ramped to 18 T with the bulk temperature kept above T_C.

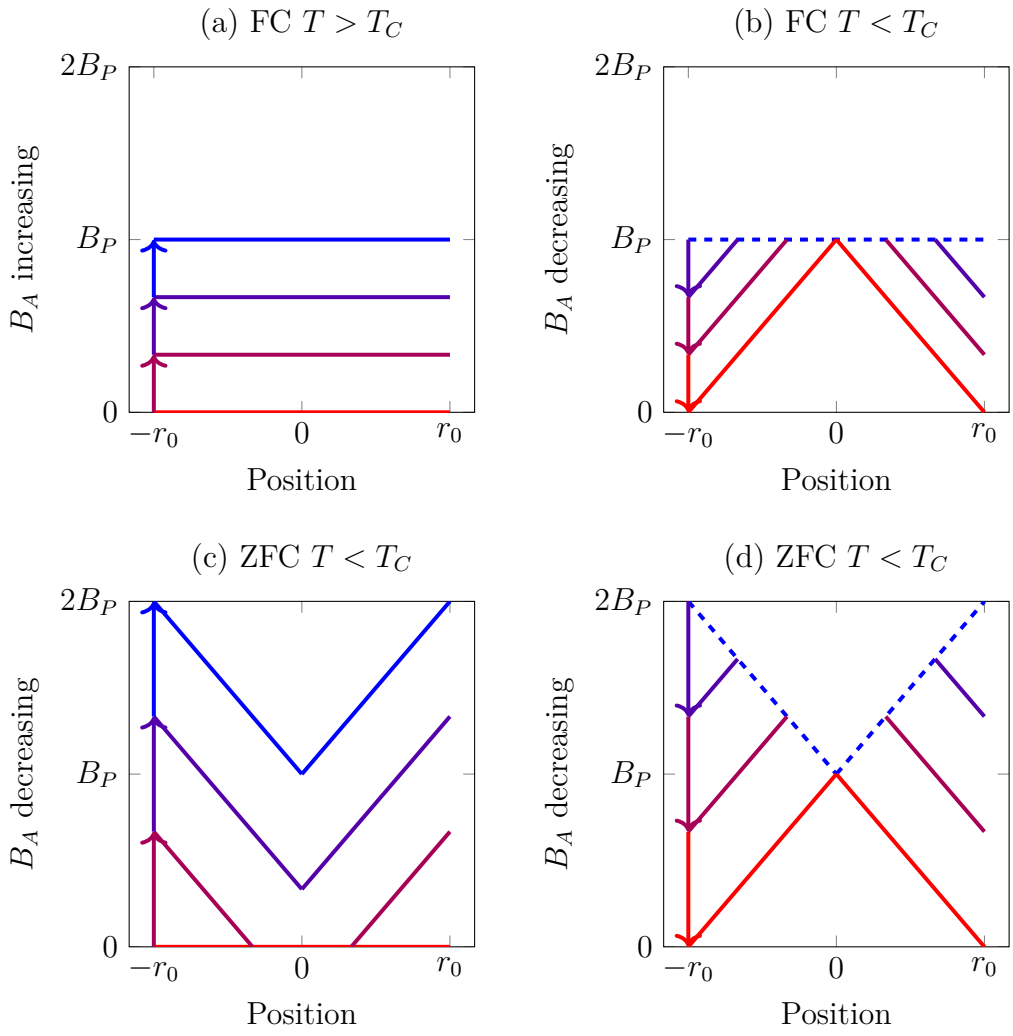

Fig. 2.18 The field cooled ((a) and (b)) and zero field cooled ((c) and (d)) magnetisation techniques. While the maximum applied field using the FC method needs to be equal to the penetration field, B_P, it needs to be equal to $2B_P$ using the ZFC method.

Then, the bulk was cooled down to 26 K and kept constant for the remainder of the procedure. Finally, the applied field was slowly ramped down, magnetising the bulk.

Both the FC and the ZFC technique typically take several hours to complete and require large superconducting magnets for the generation of the applied field. This is not very practical for portable applications for which a technique called pulsed field magnetisation (PFM) shows great promise [53, 54]. PFM is a variant of the ZFC technique in which the applied field is not ramped slowly from zero to its maximum value and back to zero; instead it is applied in the form of a short (on the order of milliseconds) pulse. Since the bulk is superconducting throughout the PFM procedure the pulse generates a significant amount of heat leading to a reduction in J_C and a lower achievable trapped field. The record trapped field achieved with PFM is 5.2 T in a GdBCO bulk [53]. The pulse of magnetic field is typically generated by discharging a capacitor bank through a copper solenoid, hence the magnetising equipment can be made more portable than that needed for the FC and ZFC techniques.

An additional advantage of the PFM technique in bulk superconductors is the flux jump effect [55, 56], by which the magnetic field suddenly enters into the superconductor during the ramp up portion of the pulse. Essentially, the heat generation due to the penetrating field increases the temperature in the periphery of the bulk and decreases the local J_C. Hence, the field penetration is increased, and with it the volume in which heat is generated, resulting in a further temperature increase. In some cases this can lead to an avalanche effect, called the flux jump, which can be used to increase the trapped field achieved by PFM. Since the flux jump occurs due to a sudden decrease in the superconductor shielding capability, PFM can be seen as a combination of FC and ZFC; whereas during FC the shielding is zero due to the temperature being above T_C, during PFM the shielding will approach zero due to the flux jump effect.

2.3.4 Magnetisation decay in bulks

Once the bulk is magnetised it can be used instead of conventional magnets as a quasi-permanent trapped field magnet. However, as the name suggests, the trapped field will invariably decay over time. The intrinsic reason for decay is flux creep, discussed in Section 2.2.6, which leads to a logarithmic decay of trapped field over time. Flux creep cannot be avoided completely since the random thermal forces will always be present, their magnitude proportional to $k_B T$. Lowering the temperature of the superconductor is an effective way of reducing decay.

Even in the absence of flux creep the trapped field may decay over time provided there is a mechanism by which the current density is made to either decrease in

amplitude or change the direction of its flow. Both these mechanisms will arise if a magnetised bulk is exposed to time-varying magnetic fields.

If a magnetised bulk is exposed to AC magnetic fields there will be currents induced below the surface of the bulk to shield it from the change in external field. The shielding currents will flow according to the Bean model and the depth of the shielding regions will be determined by the AC field amplitude and the value of J_C. Hence, the currents in the shielding regions will no longer contribute to the trapped field, which will, consequently, be reduced. In general, the mitigating measure to avoid decay due to current redistribution is, as in the case of flux creep, a reduction of the superconductor temperature. This is because at lower temperatures the value of J_C will be increased, leading to a reduced thickness of shielding regions (lower Bean penetration depth λ_B) and to a lower degree of current redistribution.

Aside from current redistribution an undesired effect of AC fields applied to the bulk is temperature rise. As discussed in Section 2.2.4 the movement of flux vortices is a dissipative process and leads to losses. An AC magnetic field will, effectively, force flux vortices to move in and out of the superconductor up to the depth λ_B, leading to heat generation per unit volume $Q = \mathbf{E} \cdot \mathbf{J}$. The subsequent temperature rise will be determined by numerous factors and can be, in principle, difficult to calculate. The amplitude of the AC field will, at a given value of J_C, determine the value of λ_B, hence it will determine the volume in which heat is generated. The frequency of the AC field will, per Faraday's law, determine the magnitude of the electric field and, with it, the value of Q. Additionally, the superconductor heat capacity and thermal conductivity can be temperature dependent, hence the change in temperature may not go linearly with Q.

To avoid temperature rise in real applications the bulks need to be in good thermal contact with the coolant or cryocooler. Typically a thermally conductive vacuum grease will be used between bulk and holder, or alternatively sheets of indium can be used to provide good thermal contact. The aim is to achieve a higher effective cooling power Q_{eff} of the cryogenic system, compared with the total heat $\int Q\, dV$ generated in the superconductor.

When talking about cylindrical bulks there are two principal axis along which the AC field can be applied: parallel and perpendicular to the cylindrical axis (we assume the trapped field is parallel to the axis). These are commonly refereed to as the parallel and crossed field configuration [57].

The parallel configuration (Figure 2.19 (a)) is well studied and generally well understood. Since the applied field is along the axis of the bulk the configuration is

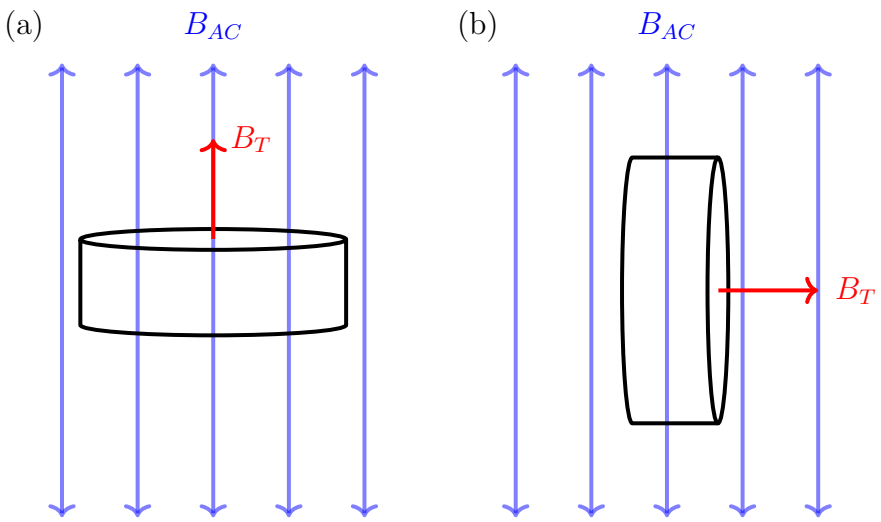

Fig. 2.19 The parallel (a) and crossed field (b) configuration. The trapped field direction is represented in red and the AC field orientation in blue arrow.

axially symmetric and relatively straightforward to model numerically. The applied field is always perpendicular to the current in the superconductor, hence the Lorentz force, $\mathbf{F}_L = \mathbf{J} \times \mathbf{B}$ is well defined.

In the crossed field configuration (Figure 2.19 (b)) the external field is applied perpendicular to the direction of the trapped field. Hence, the problem is no longer axially symmetric and needs to be modelled in three dimensions. Additionally, some parts of the circulating current will be parallel to the direction of the applied field, in the so-called force free configuration [58], since $\mathbf{J} \times \mathbf{B} = 0$. In such a configuration flux vortices can break and rejoin – in a process called flux cutting [59, 60] – or pass through other vortices. This complicates the physics of the crossed field configuration, which remains a less well understood problem.

Chapter 3

Methods

In this chapter the experimental methods employed throughout the work towards this thesis will be outlined. The experimental work can be split into three distinct groups:

1. Sample manufacture and preparation,
2. magnetic field generation (either DC, AC, or pulsed field), and
3. measurement and data acquisition.

The sample manufacture and preparation entailed growing the bulk superconductors from raw powders and of machining the samples into a desired shape - depending on the specific requirements of a given measurement. The sample preparation is described in detail in Section 3.1.

The generation of magnetic field was necessary, firstly, for the magnetisation of the samples and, secondly, to expose the samples to time-varying magnetic fields, simulating the likely magnetic environment in a real machine. For the magnetisation procedure the two main methods used were field cooled magnetisation (FC) and pulsed field magnetisation (PFM). FC will have been used to determine the maximum field-trapping capabilities of the bulk, whereas PFM was used to probe the more realistically achievable trapped field. The way by which the magnetic field was generated for magnetisation purposes is described in detail in Section 3.2. The generation of the AC magnetic field is described in Section 3.3.

The measurable quantities of interest in all experiments were, ultimately, the local magnetic field $\mathbf{B}$, the total magnetisation $\mathbf{M}$, the critical current density J_C, and their respective time dependencies. For the local magnetic field measurement on the surface of the superconductor an array of Hall sensors was used. This method allowed for the

magnetic field profile in the superconductor to be measured directly, which allowed for a straightforward comparison with theory (e.g. the Bean model).

The total magnetisation of a sample and, thus, the critical current density in a background magnetic field, was measured using a SQUID magnetometer. Essentially, the magnetic moment of a sample is measured by passing it through a set of coils and measuring the induced voltage. This is done at a range of values of applied magnetic field, hence measuring the magnetisation loop. Subsequently, the critical current density is calculated with equation 2.39.

3.1 Sample manufacture and preparation

All samples characterised in this study were $GdBa_2Cu_3O_{7-\delta}$ bulk superconductors manufactured with the top-seeded melt growth technique. The raw powders from which the bulk preforms were made were all identical in composition, but were from several different batches meaning that their respective grain size and purity will vary. Hence, the superconducting properties of the manufactured bulks will vary as well (a difference of 5 % to 10 % in trapped field of two same size bulks is common).

The specific temperature profile of the heat treatment of the bulk will also vary depending on the sample size and the powders used. As an example, a larger bulk will typically require a slower ramp rate and a longer holding time at maximum temperature in order to reach equilibrium and peritectic melting throughout the entirety of the sample. The cooling period will be longer as well due to the growth front needing to propagate a longer way to the edge of the sample from the seed crystal.

In this section the manufacturing procedure for a triangular bulk, shown in Figure 3.1 (a), is outlined. The purpose of its non-standard shape is to maximise the total flux of an assembly of several such bulks, as a triangle can tile a surface more efficiently than a circle (the improvement of the triangular shape over the cylindrical shape is discussed in Appendix A). The manufacturing procedure for all other bulks was similar qualitatively, but the heating temperature profile varied from bulk to bulk depending on its size. For a discussion on the microstructure of single grains manufactured with the top-seeded melt growth technique, see [61].

3.1.1 Pressing the bulk preform

To make the bulk preform the raw powders were ground together to form a uniform mixture. The composition of the mixture is shown in Table 3.1.

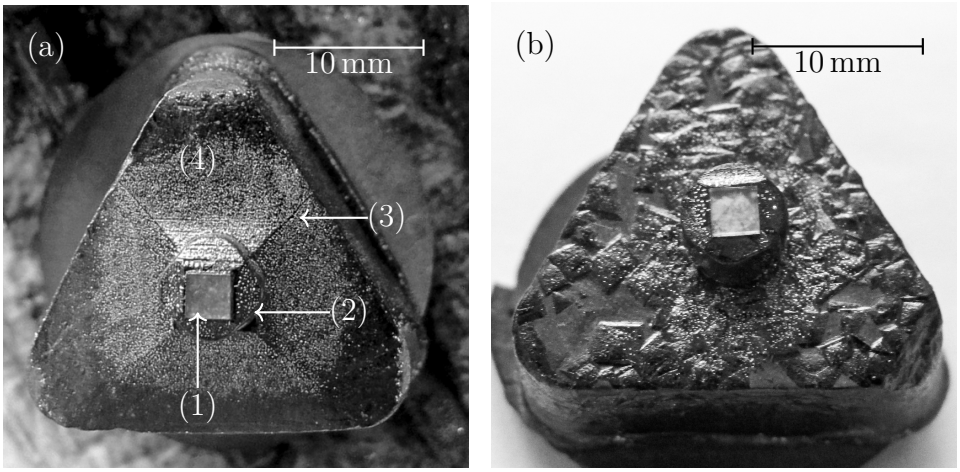

Fig. 3.1 (a) A successfully grown $GdBa_2Cu_3O_{7-\delta}$ single-grain after heat treatment: (1) the seed crystal; (2) the buffer layer between the seed and the bulk; (3) the growth sector boundary, along which the growth rate is highest; (4) the growth sector region. (b) An example of an unsuccessful growth of a bulk with numerous sub-grains apparent.

Component	Wt percent	Mass (g)
$GdBa_2Cu_3O_{7-\delta}$	67.5	9
Gd_2BaCuO_5	22.5	3
Ag_2O	9	1.2
BaO_2	0.9	0.12
Pt	0.2	0.02
Total		13.3

Table 3.1 The composition of the raw powders for the bulk preform (the sum of the masses does not equal the total mass due to rounding errors).

The $GdBa_2Cu_3O_{7-\delta}$ (Gd123) is the main superconducting phase in powder form, which will, subsequent to the heat treatment, account for the superconducting matrix in the bulk. The Gd_2BaCuO_5 (Gd211) phase is not superconducting and is added to the Gd123 phase to provide normal inclusions which act as vortex pinning centres, leading to a higher value of J_C.

The silver oxide Ag_2O is added to the preform to increase the mechanical strength of the bulk as the silver, upon melting, may seep into the pores and cracks that form during the growth of the single grain. The reduced porosity will lead to an increased survival rate of the bulks subjected to stress [62]. Additionally, the silver helps increase the thermal conductivity of the bulk, which is desirable for the purposes of effective cooling.

The barium oxide BaO_2 is added to prevent substitution of gadolinium on barium sites in the crystal structure [63]. Such substitution is undesired as it leads to lower values of T_C and J_C. Finally, the addition of platinum prevents the formation of large Gd211 grains [64], which ideally should be on the order of nanometres in scale and homogeneously distributed throughout the superconducting Gd123 matrix to provide pinning centres.

Once the raw powder is mixed, it is poured into a rubber mould, which subsequently is pressurised in a cold isostatic press up to 2000 bar. This helps to increase the density of the preform by about 100 %. Cold isostatic pressing of the bulk preform has been shown to yield an improved distribution of Gd211 across the bulk [65], as compared to uniaxial pressing and subsequent sintering, thus yielding a more homogeneous distribution of vortex pinning centres and a higher critical current density.

While the above process of preparing the sample preform is kept unchanged across different samples, the subsequent stage in the manufacture of single grains – the heat treatment, described in the next section – needs to be adjusted based on the specific batch the raw powder has been sourced from (as the raw powder is expensive it will be bought in individual batches of several kilograms). The batch-to-batch variation in powder particle size means that the heat profile needs to be adjusted for each individual powder batch for successful growth. For example, Figure 3.1 (a) and (b) shows a photograph of a successfully and unsuccessfully grown sample, respectively, using the same temperature treatment during the heat treatment for both samples, but raw powders sourced from different batches.

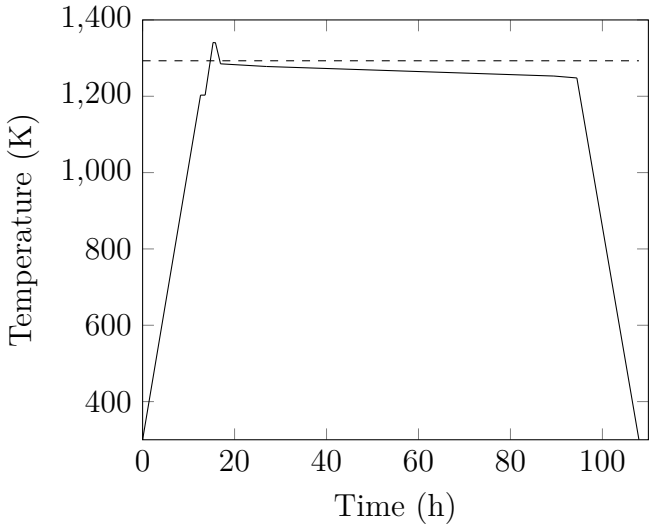

Fig. 3.2 The temperature profile during the heat treatment of the bulk preform. The dashed line represents the peritectic temperature. The durations and heating/cooling rates, defining the above profile, are shown in Table 3.2.

3.1.2 Heat treatment

After pressing, the preform was prepared for the heat treatment as shown schematically in Figure 2.17. The temperature profile during the heat treatment is shown schematically in Figure 3.2 and in detail in Table 3.2.

The initial stage of the heat treatment of the bulk is a quick ramp to just below the peritectic temperature, T_P, followed by the second stage in which the temperature is kept constant. This is to allow for the preform to shrink at the high temperature – a common feature for ceramic materials – and to allow gasses to escape, reducing porosity. In the third and fourth stages the sample is heated above T_P, and held at a high temperature to allow the Gd123 to melt. If the duration of this (fourth) stage is too high the chances of destroying the seed crystal increase, hence the total time at peak temperature is only 30 min. Subsequently, in the fifth stage the sample is cooled back below T_P, which is when the growth starts to nucleate at the seed crystal.

To increase the chances of growing a single grain, the temperature, once below T_P, must be decreased at a low ramp rate (compared to the initial heating rate). However, the growth rate of the crystal at a higher temperature is lower – and increases with decreasing temperature – which is why the temperature is initially decreased more rapidly in the sixth stage, followed by a slow ramp rate in the seventh stage. The seventh stage is when the majority of crystal growth takes place (which is also why

Stage	T_1 (K)	T_2 (K)	Rate (K/h)	Duration (h)
1	300	1203	50	12.6
2	1203	1203	n/a	1
3	1203	1341	80	1.725
4	1341	1341	n/a	0.5
5	1341	1285	-50	1.12
6	1285	1278	-0.7	10
7	1278	1253	-0.4	62.5
8	1253	1248	-1	5
9	1248	300	-0.4	13.5
Total				108

Table 3.2 The temperature profile during the bulk growth. Here, nine distinct stages are shown with the initial and final temperatures, T_1 and T_2, respectively, the ramp rate (if applicable), and the total duration of each stage.

this is the longest stage of the entire process). By the time this stage is finished the growth front along the growth sector boundary should have reached the sample edge. However, since the growth along the growth sector region is slower (by a factor of $\sqrt{2}$, due to the geometry of the growth fronts), the sample is not immediately cooled to room temperature; in the eighth stage the temperature is still ramped at a relatively low rate to allow for the final growth of the sample at the edges in the middle of the growth sector regions. Finally, the sample is cooled back to room temperature in the ninth, and final, stage.

After the heat treatment the bulks are placed into an oxygen-rich environment at $T = 400°$ for up to ten days so that the crystal structure is oxygenated, which transforms the unit cell from tetragonal to orthorhombic, and the bulk becomes superconducting.

Unlike with the cylindrical bulk the azimuthal angle of the placement of the seed crystal is not arbitrary on a triangular bulk since the properties of the superconductor on the growth sector boundaries may differ from those in the growth sector regions [66]. For this reason two different placements of the seed crystal were trialled in order to compare any potential differences of the properties of the bulks. Two bulks were grown with two different seed placements: one with the seed crystal side parallel to one of the side edges, and another with the crystal side at a 45° angle. The images of the resulting bulks are shown in Figure 3.3. The trapped fields of the two bulks are $T = 77\,\mathrm{K}$ were measured to be 0.62 T and 0.61 T, indicating that the placement of the seed crystal has little effect on the superconducting properties.

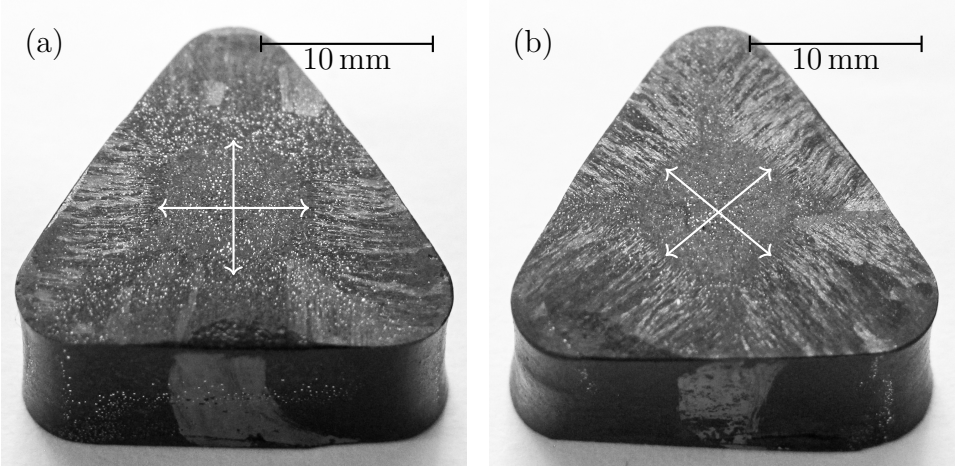

Fig. 3.3 Successfully grown single-grain bulks for two different rotations of the seed crystal. In (a) the side of the seed crystal is parallel to the bottom edge. In (b) the seed is rotated by 45° with respect to the placement in (a). The arrows indicate the direction of crystal growth (the growth sector boundaries are apparent diagonally between the arrows).

In total, six triangular bulks were manufactured (as shown in Figure 3.4) for the purpose of constructing a six pole pair ersatz motor with which the performance of the bulks in a machine environment can be tested. The progress of this project is summarised in Section 7, below.

3.2 Magnetisation procedure

3.2.1 Field cooled magnetisation (FC)

The field cooled magnetisation technique (FC) was used to determine the field-trapping capability of the samples, and to fully magnetise the samples before exposing them to time-varying magnetic fields. This was done typically at liquid nitrogen temperature, at which none of the samples examined were capable of trapping magnetic fields above around 1 T. Hence, a 1.5 T electromagnet was used for FC at 77 K as, in principle, this was sufficient to fully magnetise all the samples.

The FC procedure consisted of placing the samples in a non-magnetic stainless steel dewar, which was inserted into the bore of the electromagnet, and the magnetic field ramped up to 1.5 T. Then, the dewar was filled with liquid nitrogen to cool the superconductor samples below T_C. Once thermal equilibrium was reached, the magnetic field was ramped to zero over a period of 100 s. The slow ramp rate was to

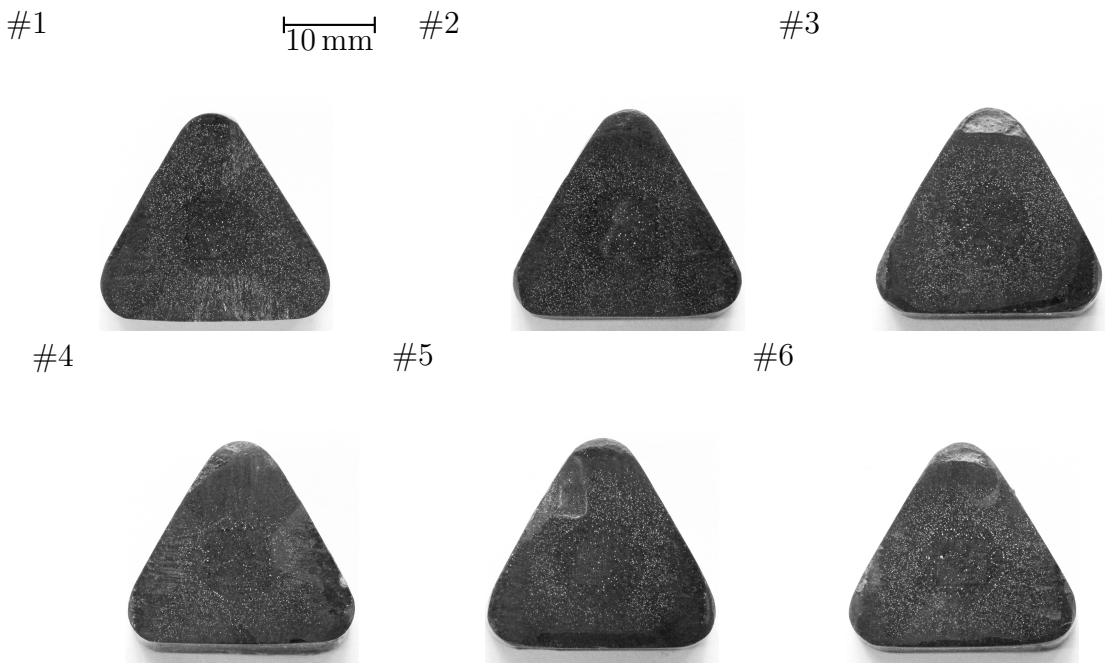

Fig. 3.4 Triangular bulk superconductors labelled #1 to #6 with centre trapped fields at 77 K, respectively, 0.77 T, 0.73 T, 0.78 T, 0.74 T, 0.76 T, 0.70 T.

prevent excessive heating of the samples, which would lead to a reduction in trapped magnetic field. After magnetisation, a waiting period of 5 min to 15 min was established to allow for any heat, generated during the magnetisation process, to dissipate. At the end of the waiting period the centre trapped field was measured using a Hall sensor. This measured trapped field was assumed to be the maximum trapped field of the bulk.

3.2.2 Pulsed field magnetisation (PFM)

The PFM system, designed by Dr Difan Zhou [67], consisted of a cryogenic system and a pulsing system. The cryogenic system is shown in Figure 3.5.

For cooling below T_C the sample was connected via a copper holder (Figure 3.5 (a)) to the cold stage of a cryocooler (Figure 3.5 (b)). The copper holder was slotted so as to prevent large eddy currents from being induced during pulsing, and generating heat. The cryocooler was a two-stage Gifford-McMahon (manufactured by Sumitomo, model number CH-204) with a base temperature of 10 K and cooling power 7.5 W at 20 K.

The sample and the cryocooler together were enveloped in a stainless steel can (Figure 3.5 (c)), which was used to keep the cryogenic system under vacuum. Atop the steel can a G10 box was placed (Figure 3.5 (d)), containing the pulsing copper

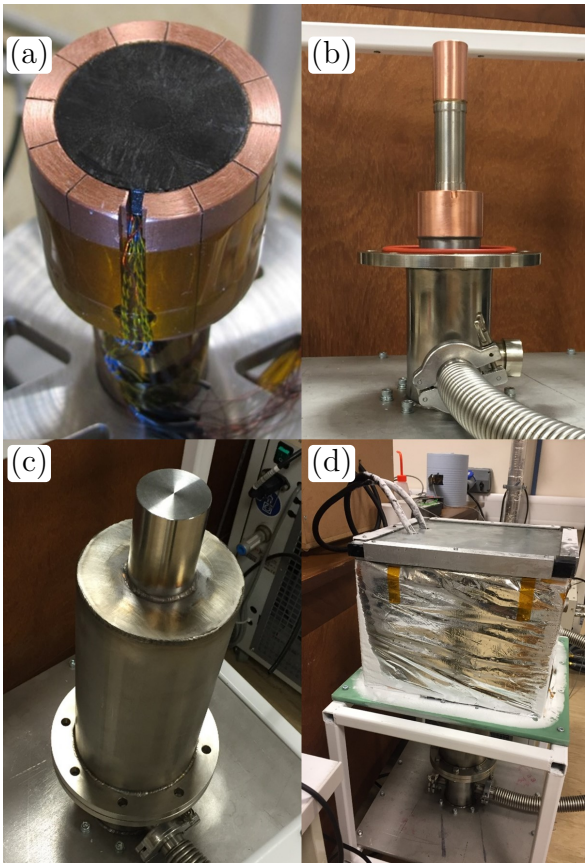

Fig. 3.5 (a) The sample (black) in a copper holder, which itself is connected to the (b) cold stage of the GM cryocooler. (c) The steel vacuum can. (d) The G10 box with a copper solenoid submerged in liquid nitrogen.

Wire diameter	2.6 mm
Solenoid height	60 mm
Inner diameter	50 mm
Outer diameter	140 mm
Number of turns	300

Table 3.3 The geometry of the pulsing coil.

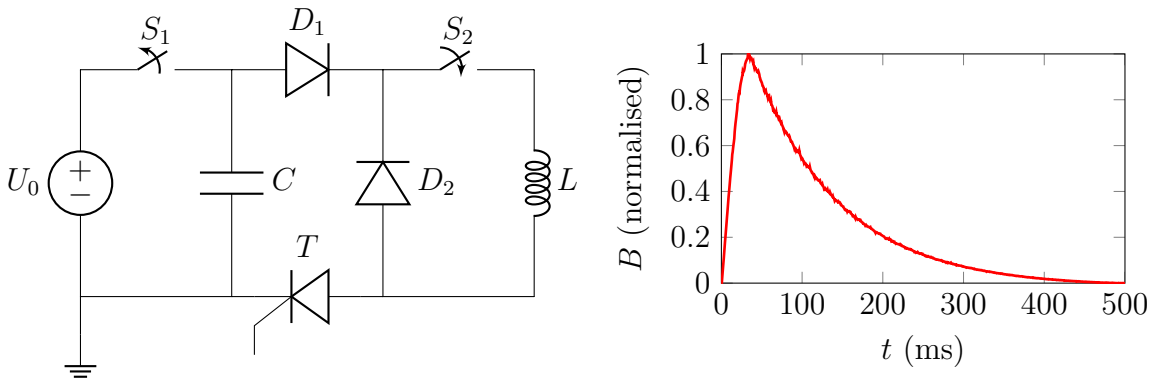

Fig. 3.6 (Left) The circuit diagram of the pulsing rig. For charging the capacitor bank, C, S_1 is closed and S_2 is open. Subsequently, S_1 is opened and S_2 is closed, and the pulse of current through the coil is triggered by the thyristor, T. (Right) The resulting pulse of magnetic field in the bore of the discharge coil.

solenoid, submerged in liquid nitrogen. The coil bore size was sufficient to fit over the narrow part of the vacuum can, in which the sample was held. The solenoid geometry is shown in Table 3.3.

Alternatively to this setup, the sample could be placed directly into the bore of the copper solenoid and submerged into liquid nitrogen - this was convenient for measurements at 77 K. For this purpose bespoke sample holders were made from G10.

The main components of the pulsing part of the system were a capacitor bank and a pulsing coil - the circuit diagram is shown in Figure 3.6 (left). The operating principle was as follows: initially, the capacitor bank was charged by connecting it to a DC current supply. Once a desired voltage across the bank was achieved the capacitors were disconnected from the power supply and discharged through a solenoid or split-pair type pulsing coil. This produced a pulsed current (and, hence, magnetic field), which was used to magnetise the superconductor.

The pulsing rig is essentially a damped LCR circuit. The capacitors are connected with the discharge coil through a diode D_1 and a thyristor T. The diode is used to

C_{bank}	208 mF
L_{coil}	4 mH
R_{coil} (300 K)	240 mΩ
R_{coil} (77 K)	35 mΩ
V-B characteristic	20 mT V^{-1}
pulse rise time	30 ms
pulse duration	500 ms

Table 3.4 The specifications of the PFM rig.

prevent a reverse voltage on the capacitors, and the thyristor is used to complete the circuit to generate the pulse. Additionally, a second diode, the flyback diode D_2, is connected in parallel with the coil.

The resulting pulse shape, which will depend on the total capacitance, resistance and inductance of the circuit, is shown in Figure 3.6 (right). Given a set capacitance of the bank, and a set coil inductance, the characteristic time of the circuit can be varied by changing the resistance. Since it is desirable to generate a pulse with as short a rise time as possible in order to trigger the flux jump effect in the superconductor [67], the resistance of the circuit has to be as low as possible. For this reason the pulsing copper solenoid is placed into a liquid nitrogen bath. Finally, the peak magnetic field value during the pulse is varied by varying the initial voltage across the capacitor bank, and the relation is linear: doubling the voltage will double the peak magnetic field. The specifications of the circuit and the pulsing coil are shown in Table 3.4.

3.3 AC magnetic field generation

Once the superconductor is magnetised, either by using FC of PFM, it is of interest to determine its response to an AC magnetic field. To genereate the AC field a copper solenoid is connected with an AC current supply, and the sample is inserted into the bore of the solenoid. Since the current-magnetic field characteristic of the coil is known (it is measured by passing a known DC current through the coil and measuring the generated magnetic field with a Hall sensor), the applied AC magnetic magnetic field can be inferred by measuring the amplitude of the AC current. For this reason the coil is connected in series with a shunt resistor (of a known resistance), and the voltage drop across the resistance is monitored throughout.

Depending on the type of measurement performed, a different setup will have been used to obtain the experimental data, presented in the results chapters, below (Chapters 4 - 6). The main differences between the setups are:

1. The direction of applied AC magnetic field with respect to the trapped field (parallel or perpendicular),
2. The temperature, at which the sample was kept (at 77 K in liquid nitrogen, or at lower temperatures using a GM cryocooler),
3. The type of measurement performed (measurement of local magnetic field with Hall sensors, or of total flux with a pick-up coil).

Based on these differences the different setups used are summarised in the following sections.

3.3.1 Decay measurements in the perpendicular configuration

In the perpendicular (crossed-field) configuration the AC magnetic field is applied perpendicular to the direction of trapped field of the superconductor. Therefore, in our setup, two different solenoid coils were used: first for magnetisation and second for the application of the AC magnetic field.

For measurement of trapped-field decay in the crossed-field configuration, presented in Chapter 4, the following procedure was employed. The sample was initially magnetised using the field cooled (FC) magnetisation procedure in a 1.5 T electromagnet, as described in the previous section.

Following magnetisation the sample was inserted into a bore of a copper solenoid, which was, itself, submerged in liquid nitrogen. This setup is shown in Figure 3.7. The sample is held in the centre of the bore with a G10 holder (not shown in the schematic). On the top surface of the sample a Hall sensor, or Hall sensor array, is mounted to monitor the local trapped magnetic field over time - the Hall voltages are acquired using a data acquisition card connected with a computer for storing data.

Throughout this work the Hall sensor model used was Lakeshore HGT-2101, which has a sensitivity of 1.1 V T^{-1} to 2.8 V T^{-1}.

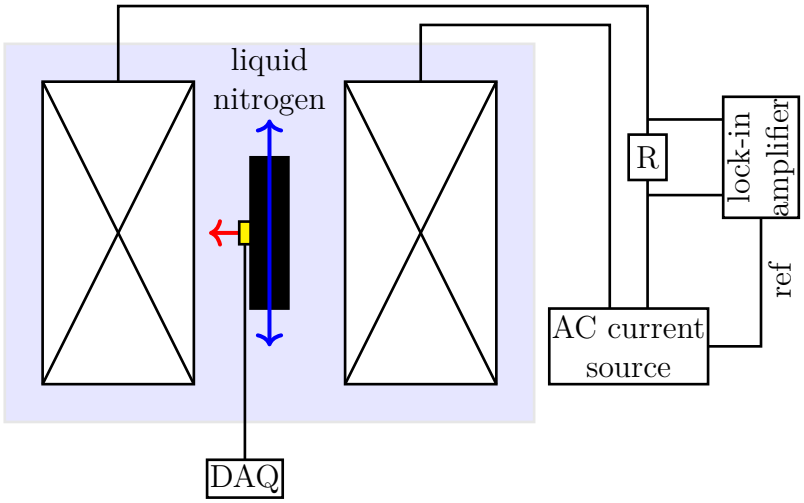

Fig. 3.7 The experimental setup for crossed-field decay measurements. The single grain (black rectangle) is inserted into the bore of the solenoid with its trapped field (red arrow) perpendicular to the orientation of the AC magnetic field (blue arrow). The trapped field over time is measured using a Hall sensor mounted on its surface (yellow rectangle).

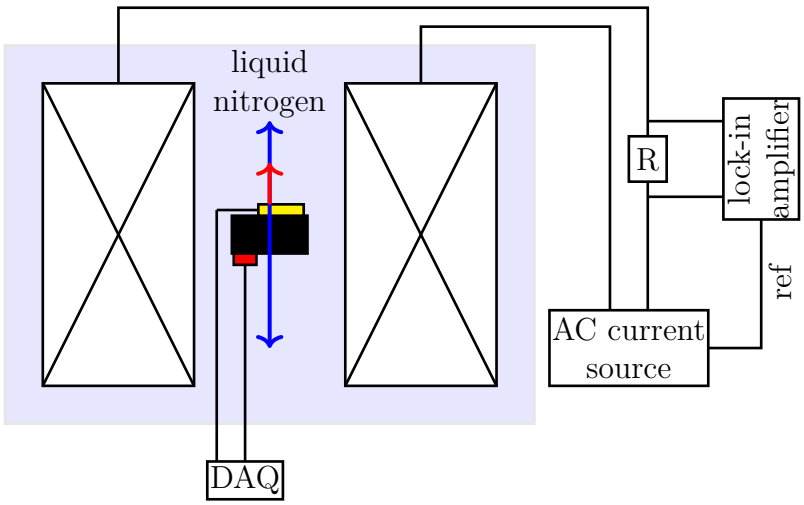

Fig. 3.8 The experimental setup for measuring the decay of trapped field (red arrow) in the parallel configuration (AC magnetic field in blue). The bulk (black rectangle) is fitted with an array of Hall sensors (yellow) and a temperature sensor (red). Prior to the AC field application the solenoid is connected with a capacitor bank, which produces a pulse of magnetic field.

3.3.2 Decay measurements in the parallel configuration

In the parallel field configuration the AC magnetic field is applied parallel to the direction of the trapped magnetic field. For this reason the coil with which the sample has been magnetised can be used subsequently to generate the AC magnetic field. Thus, in the parallel configuration (results presented in Chapter 5), the sample was magnetised using PFM. After magnetisation, the charging coil was disconnected from the capacitor bank and connected to an AC current source. The schematic is shown in Figure 3.8.

The decay measurements were done initially with the superconductor at 77 K in a liquid nitrogen bath. Subsequently, the measurements were done at lower temperatures as well, by using a GM cryocooler. The sample was connected to the cryocooler with a bespoke copper holder (shown in Figure 3.5 (a)). The schematic of the placement of the copper solenoid with respect to the sample is shown in Figure 3.9.

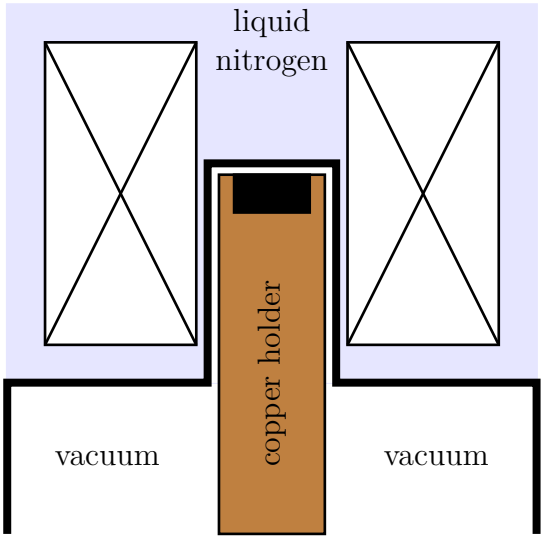

Fig. 3.9 The setup used for measurements at temperatures below 77 K.

3.3.3 Pick-up measurements in the parallel configuration

The total flux through, or total magnetisation of, a superconducting sample can be measured by a magnetometry technique, typically involving the measurement of induced voltage through a pick-up coil wound round the sample. This method gives information about the whole sample; however, for the pick-up method to work the flux has to be changing in some way. A standard method is to induce a changing flux by applying an AC magnetic field, or another possibility is by changing the position of the sample with respect to the pick-up coil, such as in a SQUID magnetometer, or in a vibrating reed magnetometer.

Generally, the induced voltage in a coil wound round a superconductor can be expressed as

$$U_i = -N\frac{\partial \Phi}{\partial t}, \tag{3.1}$$

where N is the number of turns in the coil. If the superconductor is axially symmetric (e.g. a cylinder) and $B(r,t)$ is the radial magnetic field profile in the superconductor, the induced voltage can be expressed as

$$U_i = -2\pi N \int \frac{\partial B(r,t)}{\partial t}\, dr, \tag{3.2}$$

where r is the radial coordinate.

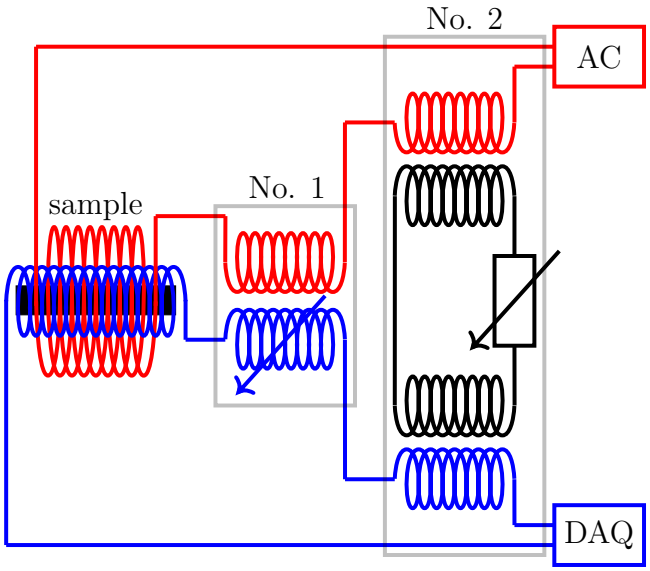

Fig. 3.10 The circuit diagram of the measurement set-up (in red is the driving AC coil, in blue the pick-up circuit connected to the data acquisition card). The sample with the two enveloping coils is inserted into a superconducting DC magnet (not shown). The two balancing rigs are labelled No. 1 and No. 2.

The pick-up coil method was used in this work to measure the Campbell penetration depth, with the results presented in Chapter 6. The measurement procedure consisted of exposing a non-magnetised superconducting sample to AC magnetic fields and measuring its response in the form of induced voltage in a pick-up coil. To extract the desired signal from the measured voltage a precise balancing rig had to be constructed - the circuit schematic is shown in Figure 3.10.

The sample (shown in black rectangle in Figure 3.10) was fitted with a pick-up coil of 1000 turns, wound tightly round its cross-section. The sample with the pick-up coil was, then, inserted into the bore of a larger solenoid, which was used to produce the external AC magnetic field by passing an alternating current through it. The current amplitude was set so that the AC magnetic field amplitude was 1 mT, and its frequency was set to 300 Hz. The sample with the two coils was then inserted into the bore of a superconducting magnet (not shown in Figure 3.10), used to produce the larger DC magnetic field, up to the amplitude of 6 T. The temperature of the sample was kept constant at 70 K by using helium gas in the variable temperature insert of the superconducting magnet.

In addition to the pick-up coil wound round the sample there were two balancing rigs connected in series in order to eliminate noise from the measurement. In Figure

3.10 the sensing circuit is shown in blue, the driving AC circuit in red, and the two balancing rigs used labelled number 1 and 2.

The first balancing rig consisted of a variable mutual inductance between the sensing and the driving circuit. By tuning the variable mutual inductance a signal in phase with the pick-up voltage could be added to, or subtracted from, the pick-up voltage. This was used to subtract any pick-up voltage induced in the sensing coil due to the finite thickness of the winding. The pick-up coil had 1000 turns in several layers, therefore not all the wire was in direct contact with the sample. This means that an AC magnetic field, passing through the inner layers of the coil, would induce a voltage in the outer layers. This voltage had to be subtracted from the signal as it carried no information about the flux penetration into the sample. This was done by applying an AC magnetic field to the sample in the virgin state - at zero DC magnetic field - and at a low amplitude of 1 mT, below the first critical field. At that point, the balancing rig 1 was tuned so that the measured signal was zero. This meant that all the aforementioned voltage due to the finite thickness of the pick-up coil was subtracted - and any signal measured subsequently at non-zero DC magnetic field would give a direct measure of the flux penetration beyond the London penetration depth.

The second balancing rig consisted of a set of two mutual inductances between the sensing and the driving circuit, connected with a variable resistor. In contrast to the balancing rig 1, this was used to subtract any unwanted signal a quarter period out of phase with the pick-up voltage. If there are any flawed connections present in either of the circuits this will lead to parasitic capacitances in the connections - shifting a portion of the signal by one quarter period. A similar effect will be seen in the presence of conductors in the vicinity of the sensing circuit - the AC magnetic field will induce eddy currents in the conductors, which will, in turn, induce a back emf in the sensing circuit. This will be shifted in phase by a quarter period as well. For these reasons, the balancing rig number 1 was insufficient to subtract all of the parasitic signal, and the second balancing rig was used. With both the rigs the signal could be balanced to 0.1 %. Additionally, the signal was averaged over 1000 periods of AC field to improve the resolution.

3.4 Finite element modelling

In addition to the experimental work finite element modelling (FEM) was performed in order to compare measured data with theory. For this a commercial FEM package Comsol Multyphysics 5.3a was used. FEM simulations have become a standard way

of numerical analysis of high-temperature superconducting materials, because type-II superconductors, in particular, can be adequately described in most applied-type problems with just Maxwell's equation without the need to look at the microscopic picture. For a detailed review of superconductor FEM modelling, see [34].

Essentially, FEM consists of creating a grid of points, called the mesh, in a geometry that matches the geometry of an experiment we wish to model. Hence, Maxwell's equations, in conjunction with a constitutive relation, are solved in each point of the mesh in a self-consistent way. As an example, in the **H**-formulation [34], employed here, Ampere's law,

$$\nabla \times \mathbf{H} = \mathbf{J}, \tag{3.3}$$

and Faraday's law,

$$\nabla \times \mathbf{E} = -\mu_0 \frac{\partial \mathbf{H}}{\partial t}, \tag{3.4}$$

are solved with the addition of the constitutive **E-J** power law,

$$\frac{E}{E_0} = \left(\frac{J}{J_C}\right)^N, \tag{3.5}$$

where the electric field, **E**, is assumed parallel to the current, **J**. The value of the constant E_0 determines the electric field when the current density becomes $J = J_C$, and is typically chosen to be $E_0 = 1\,\mu\mathrm{V\,cm^{-1}}$ [34]. The value of J_C will typically be measured as a function of B and input into the model by means of a look-up table, or its value will be chosen such that the trapped field predicted by FEM will match the measured trapped field. The value of N will determine the rate of flux creep; here, $N = 20$ is chosen, which is a typical value for high-quality superconductors with a low flux-creep decay rate (see the results section in Chapter 4 for more details).

Chapter 4

Crossed-field decay in bulk superconductors

4.1 Background

Bulk superconductors, employed as quasi-permanent trapped-field magnets, appear a likely candidate for future applications in which high magnetic fields in small volumes are a requirement. A prime example of such a potential application is a permanent-magnet electric motor or generator, in which conventional magnets are used to generate the magnetic field in the rotor or stator [68]. Permanent magnet electric machines are attractive as the magnetic field is generated passively, hence avoiding the need for slip rings or additional power supplies. However, the limitation of conventional magnets to generating magnetic fields of at most 1.8 T imposes an upper limit to the power density of these machines. In contrast, bulk superconductors can generate trapped magnetic fields an order of magnitude higher and are, as such, attractive alternatives for future light-weight electric motors.

Despite the initial order-of-magnitude improvement in magnetic field, however, the trapped field in a bulk superconductor will decay with time due to flux creep. The decay will further be accelerated in the presence of AC magnetic fields – a likely magnetic environment in rotating electric machines due to the inevitable non-ideal nature of the motor or generator. For this reason it is of interest to study the effects of external time-varying magnetic fields on the time-dependence of the trapped field in bulk superconductors.

In this chapter the focus will be on one specific geometry, the crossed-field configuration, shown schematically in Figure 4.1. In this thesis the analysed material will be

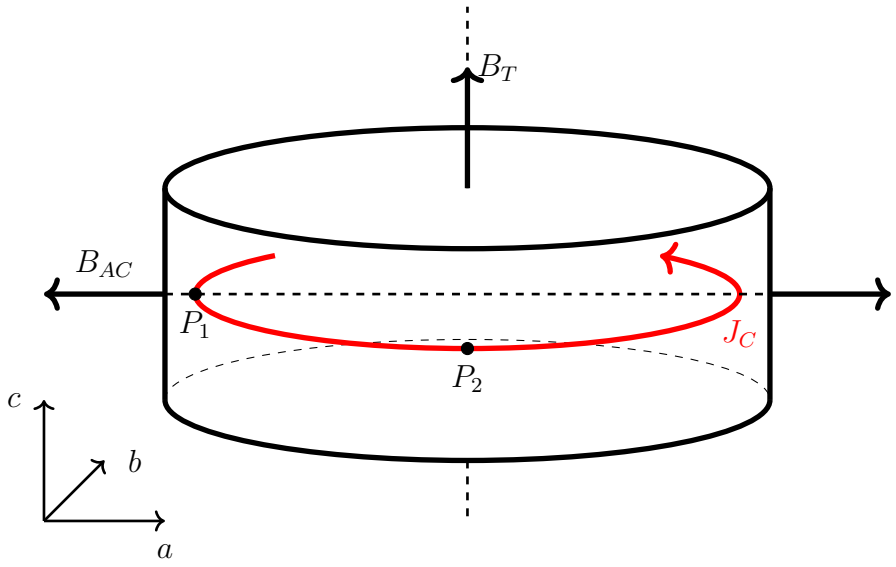

Fig. 4.1 A schematic of the crossed-field configuration. The external magnetic field, magnetising the bulk, is initially applied along the c-direction, which induces currents to flow in the ab-plane. Subsequently, B_{AC} is applied parallel to the ab-plane. In points P_1 and P_2 the current is, respectively, perpendicular and parallel to B_{AC}.

exclusively $GdBa_2Cu_3O_{7-\delta}$ in bulk form and so it is convenient to define the geometry of the problem in this initial section and refer to it throughout the text.

The crossed-field configuration in this work is defined as follows. We begin with a single-grain bulk superconductor in the shape of a cylinder in which the crystallographic c-direction is parallel to the cylindrical axis. The bulk is magnetised along the c-direction by one of the aforementioned magnetisation techniques, which induces a current to flow in the azimuthal direction everywhere in the bulk (red arrow in the ab-plane, Figure 4.1), leading to a trapped field parallel to the c-direction. The bulk is said to be fully magnetised if the current density throughout is $J = J_C$ (J_C can be a function of the local magnetic field, B).

Following magnetisation an AC magnetic field, called here the crossed-field, is applied perpendicular to the c-direction, and its effects on the trapped field are studied by means of a Hall probe array or a pick-up coil. Typically, the trapped field decays over time in what is called the crossed-field decay. This particular configuration is interesting to study as it has been shown to lead to the largest rate of decay [57] (this is true for applied fields of double polarity; for homopolar applied fields the direction leading to the greatest decay is anti-parallel to the trapped field). For this reason

it remains important to first understand crossed-field decay in order to subsequently mitigate against it.

4.2 Previous studies

In this section the relevant studies of the crossed-field effect will be summarised. A common thread among all of them is the effect of a magnetic field, applied perpendicular to some axis, on the trapped field or magnetic moment along the axis. Ultimately, the applied field will induce currents to flow in shielding regions below the surface of the superconductor, and this can adequately be explained within the Bean model framework. Another common thread, when the applied crossed-field is an AC magnetic field, is a rapid decay of trapped field over time. Most of the studies mentioned here find that the decay of trapped field over time is exponential – especially at short times immediately after the start of AC field application, and for AC field amplitudes which fully penetrate the superconductor. In the subsequent section this exponential decay – in conjunction with the logarithmic decay due to flux creep – will be taken as an assumption in the derivation of an analytical model, used to predict crossed-field decay in bulk superconductors.

Some of the earliest work on the effects of mutually perpendicular components of magnetic field applied to a superconductor was done by LeBlanc and Mattes on coils of NbTi, a low temperature type-II superconductor [69]. The authors showed that the component of the magnetic moment along the axis of the coil will change as the magnetic field component perpendicular to the axis of the coil changes (even when the magnetic field component along the axis does not change). This is explained as being due to currents induced perpendicular to the direction of the total magnetic field (the sum of the parallel and perpendicular components).

Funaki and Yamafuji [70–72] studied the effect of an AC magnetic field applied to a linear array of superconducting wires, used to approximate an infinite slab. They showed that if a DC magnetic field is applied perpendicular to the wires and an AC magnetic field is applied along the wires, the shielded magnetic field at the centre of the array will approach the DC magnetic field value. Here, again, the AC field changes the component of the magnetic field, perpendicular to its orientation. Additionally, they showed that the magnetic field penetrates the wires in shielding regions of induced current, the thickness of which depends on the amplitude of the applied field.

Park and Kouvel [73] studied the crossed-field effect in a $YBa_2Cu_3O_{7-\delta}$ bulk superconductor. The authors magnetised a single-grain superconducting disk along the

c-direction and measured the magnetic moment components in the *c*-direction and in the *ab*-plane (M_c and M_{ab}, respectively). They showed that, although the M_{ab} component obeys a Bean-like hysteresis, the M_c component decays essentially to zero in the first few cycles of applied AC field. This is in contrast to the much slower intrinsic decay due to flux creep.

Fischer *et al.* [74, 75] measured magnetisation loops (for a DC magnetic field along the *c*-direction) in $YBa_2Cu_3O_{7-\delta}$ platelets while simultaneously applying an AC magnetic field parallel to the *ab*-plane. The loops were shown to become narrower for an increasing amplitude of AC field. Additionally, the irreversibility field was shown to decrease and to approach zero as the AC field magnitude reaches the value of the penetration field for the sample. At that point the magnetic moment becomes reversible and the critical current density zero.

All these studies point to a decay of magnetisation due to an applied crossed-field, which itself effectively renders the magnetic moment reversible. In essence, the crossed field, by shaking the pinned flux vortices, reduces the effective pinning force to zero, making the vortices free to move under the influence of the Lorentz force. Then, the time dependence of magnetisation cannot be predicted by the Bean model as, if the pinning force is zero, $J_C = 0$.

Instead, the time dependence of current density in the superconductor with zero pinning force can be analysed by the Langevin equation 2.32, where the pinning force is assumed zero,

$$\eta_v v = \eta_v \frac{\partial y}{\partial t} = B_0 J, \tag{4.1}$$

where η_v is the vortex viscosity, y is the vortex displacement, v its time derivative, the vortex velocity, and $B_0 J$ is the Lorentz force. Since the current density is $J > J_C = 0$ the above equation describes vortex flux flow. The subsequent derivation of the time-dependence equation for y proceeds in a similar way to the derivation of equation 2.55 (the differential equation describing the Campbell penetration depth), giving

$$\eta_v \frac{\partial y}{\partial t} = \frac{B_0^2}{\mu_0} \frac{\partial^2 y}{\partial t^2}, \tag{4.2}$$

which can be solved by a separation of variables. It can be shown that the vortex velocity decays exponentially with time,

$$v \propto \exp\left(-\frac{t}{\tau}\right), \tag{4.3}$$

where the decay time $\tau \propto \eta_v$. In essence, a distribution of vortices, contributing to a bulk current density, will be pushed apart by the Lorentz force in the absence of pinning. As the vortices move further apart the current density will decrease, and so too will the Lorentz force. Hence, the rate of change of current will be proportional to the current itself, leading to exponential decay.

In the case of crossed-field decay this situation may arise because, due to the AC-field-induced moving of vortices back and forth, the vortices cannot remain pinned and the effective pinning force becomes zero. For example, the total force acting on a vortex, averaged over one period of AC field, is proportional to the Lorentz force as the force due to the AC field averages to zero.

The exponential-like decay has been observed elsewhere as well. Willemin et al. [76] explained the phenomenon as being due to the shaking of the flux vortex lattice. They showed that, provided the amplitude of the crossed-field is sufficient, the decay of magnetic moment in a $YBa_2Cu_3O_{7-\delta}$ single-grain is exponential across several orders of magnitude of magnetisation. Subsequently, LeBlanc et al. [77] conducted similar measurements in a stack of $Bi_2Sr_2Ca_2Cu_3O_{10+x}$ thin films and they showed that, while the decay of magnetisation initially appears exponential, at longer times the decay rate decreases and the magnetisation plateaus at some non-zero value. As we shall see in the following section, this plateauing is a common feature in our results as well. This is due to the incomplete penetration of the crossed-field and a combination of the exponential decay, mentioned here, and the logarithmic decay due to flux creep.

More recently, Vanderbemden et al. [78] studied the crossed-field decay in single grain $YBa_2Cu_3O_{7-\delta}$, noting the tilting of trapped field due to the induced shielding regions with a non zero component of current in the c-direction. The authors corroborated this in subsequent studies [79, 80] in which experiment was complemented with finite-element modelling (FEM). In order to simplify the numerical modelling the authors employed a 2D infinite-slab model as an approximation of the 3D bulk, showing that the results agree qualitatively with the experimental data. The FEM proved useful in predicting the distribution of current across the cross-section of the superconductor. Due to the now widespread availability of commercial FEM packages it has become standard practice to analyse the crossed-field configuration in a combination of experimental analysis and numerical modelling.

Badía-Majós and López [81] first showed that, using FEM, the pure Bean model (constant J_C and the $E-J$ power law exponent $N \to \infty$), in conjunction with Maxwell's equations, is sufficient to describe the initial rapid decay and subsequent plateauing of magnetisation provided that there is some current-free region beyond the depth to

which the initial magnetising field has penetrated. However, with the infinite value of N the intrinsic decay due to flux creep cannot be predicted. Numerous later studies have successfully employed FEM analyses with a finite value of N across different materials and geometries, including studies done on (RE)BCO bulks [82–85] and tape stacks [86–89], MgB_2 bulks [90], and $Bi_2Sr_2Ca_2Cu_3O_{10+x}$ tapes [91].

The wide scope of the studies mentioned is a testament to the great versatility and applicability of this combined experimental and modelling approach. However, a remaining issue is that, depending on the complexity of the study, the calculations done by FEM software packages can take days to weeks to perform. This is due – in part – to the highly non-linear behaviour of the superconductor, described by the $E - J$ power law, which entails large changes in electric field for even small perturbations of current density at $J \approx J_C$. Moreover, in order to perform a sweep of the parameter space (e.g. to change the AC magnetic field frequency or amplitude across a range of values), the total calculation time increases further, making the studies impractical. Hence, analytical models will always be preferable – at least initially, with simplified geometries – as they are much less computationally demanding.

In the following section I present an analytical model with which I explain the trapped field decay in a bulk superconductor in the crossed-field configuration. The model takes into account both the rapid exponential-type decay due to the crossed-field, as well as the slower logarithmic decay due to the intrinsic flux creep. The model is subsequently compared with measurements of trapped field decay in a $GdBa_2Cu_3O_{7-\delta}$ bulk superconductor and is shown to agree very well with the data. Additionally, FEM analysis is performed to serve as a benchmark against which the analytical model can be compared, and to help visualise some of the geometrical assumptions made in the derivation of the analytical model. I show that the analytical model reproduces very well the FEM predictions of the current density redistribution, as well as of the penetration depth of shielding currents due to the crossed-field.

4.3 Two mechanisms of trapped-field decay: an analytical model

4.3.1 Derivation

The goal of this section is to derive a model with which the time dependence of trapped field in a bulk in the crossed-field configuration can be predicted. In summary, the model is based on calculating the trapped field on the surface of the bulk from

an assumed current distribution using the Biot-Savart law. The AC magnetic field is assumed to penetrate the superconductor in shielding regions, which are regions of thickness λ (the Bean penetration depth), as measured perpendicularly from the superconductor surface (see Figure 4.2). The time dependence of the current density is assumed to change at the penetration depth of the AC field: beyond the penetration depth the current is assumed to decay logarithmically due to flux creep, whereas within the penetration depth of the surface it is assumed to decay exponentially due to the crossed-field. The model is purely empirical; here, no microscopic derivation is presented. For this reason all the assumptions will be justified only in comparing the model with experiment and FEM analysis.

To start, let us consider a fully magnetised cylindrical bulk superconductor of height h and radius R, shown schematically in Figure 4.2 (a). The current density everywhere in the bulk is $J = J_C$, with the currents flowing in the azimuthal direction. The trapped field at the centre of the top surface of the bulk ($z = r = 0$) can be calculated via the Biot-Savart law as

$$B(\mathbf{r} = 0) \equiv B_0 = \frac{\mu_0}{4\pi} \iiint \frac{\mathbf{J}(\mathbf{r}') \times (\mathbf{r} - \mathbf{r}')}{|\mathbf{r} - \mathbf{r}'|^3} \, d^3\mathbf{r}' = \frac{1}{2}\mu_0 J_c h f\left(\frac{R}{h}\right), \tag{4.4}$$

where, for the purposes of clarity in the subsequent derivation, we defined the function

$$f(x) = \ln\left(x + \sqrt{1 + x^2}\right). \tag{4.5}$$

Since all the currents contribute constructively to the trapped field there are two fundamentally different mechanisms by which the trapped field can be made to decay:

1. reduction of current density, and

2. redistribution of current density.

If the current density, flowing through the superconductor, decreases such that $J < J_C$ – regardless of the mechanism by which J decreases – the trapped field will decay. Conversely, even if the current density remains critical, if some of the current changes its direction of flow so that it no longer circulates in the azimuthal direction, the trapped field will decay as well.

Once the initial magnetisation is established the bulk is exposed to an external crossed-field perpendicular to the direction of magnetisation. The crossed-field will penetrate the bulk from the top and bottom surfaces up to the field-dependent Bean penetration depth, λ, forming shielding regions I and III (shown in gray in Figure 4.2

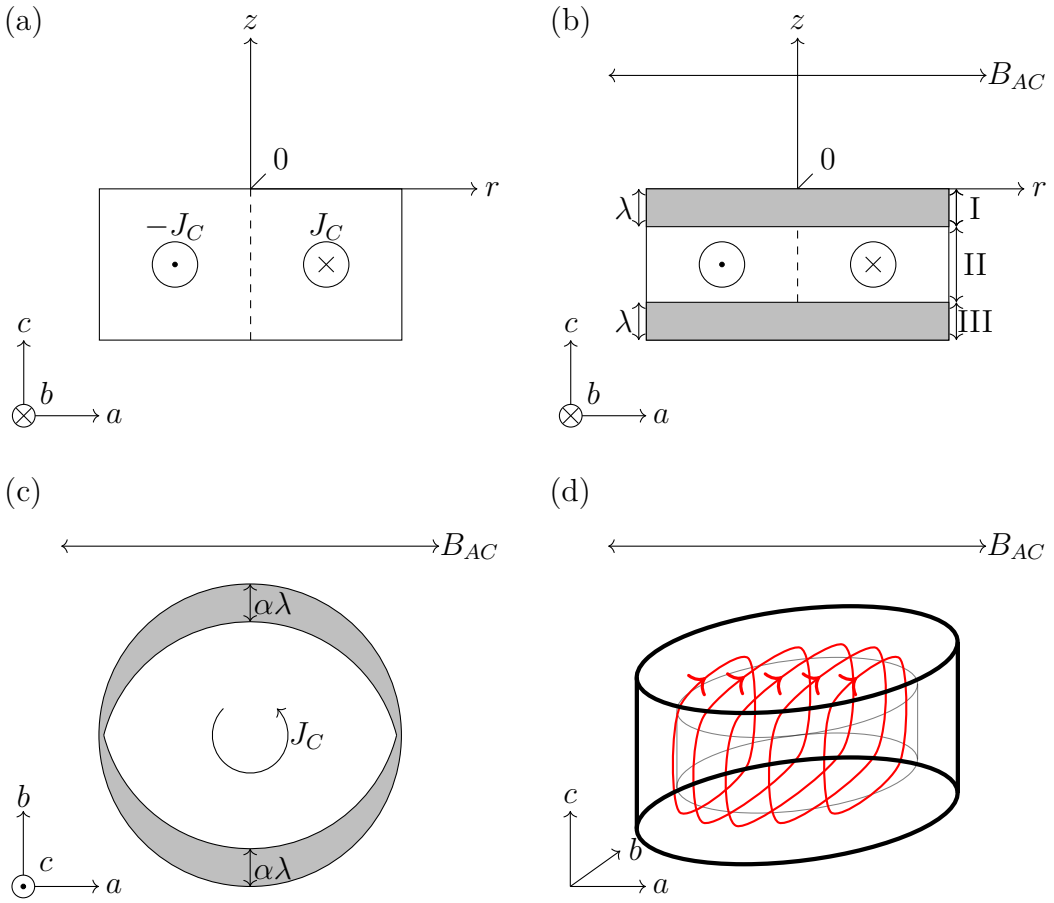

Fig. 4.2 (a) A schematic representation of a fully magnetised bulk superconductor: the current density is $J = J_C$, flowing in the azimuthal direction. (b) The change of current density due to the crossed field: in the shielding regions I and III the current changes direction every half-cycle of the applied field. The thickness if the region is the penetration depth, λ. (c) Plan view (top-down) of the shielding regions. The thickness is $\alpha\lambda$, where α is the critical current anisotropy. (d) A projected view of the induced currents in the region between the inner and the outer cylinder (the inner cylinder corresponds to region II in (b)).

(b)). In these regions the crossed-field will affect the established circulating current in much the same ways as discussed in the previous section: the current will be made to decay exponentially with time. More accurately, the current contribution to the trapped field (i.e. the product $\mathbf{J}(\mathbf{r}') \times (\mathbf{r} - \mathbf{r}')$ in equation 4.4, averaged over one period of crossed-field) will decay exponentially with time; however, mathematically the final calculated trapped field is identical in both situations. Hence, the time dependence of current density in regions I and III can be written as

$$J(t) = J_C \exp\left(-\frac{t - t_1}{\tau}\right), \tag{4.6}$$

where t_1 is the time at which the crossed-field is turned on, such that $J(t = t_1) = J_C$, and τ is a characteristic time constant of decay and will depend on the crossed-field amplitude and frequency.

In region II in Figure 4.2 (b), which is beyond the penetration depth of the crossed-field, the current is assumed to decay due to flux creep and its time dependence can be written as

$$J(t) = J_C \left(1 - k \ln\left(\frac{t}{t_1}\right)\right), \tag{4.7}$$

where k is the logarithmic decay rate. The time dependence of current is, again, chosen such that $J(t = t_1) = J_C$.

In addition to the formation of three distinct regions along the bulk height, the crossed-field will induce shielding currents to flow in the c-direction along the sides of the bulk so that the current loops are completed (shown in Figure 4.2 (c) and (d)). The thickness of these regions will be determined by the Bean penetration depth as well; however, due to the anisotropy of critical current density, α, the thickness will be $\alpha\lambda$. The critical current anisotropy in $GdBa_2Cu_3O_{7-\delta}$ is [83, 92]

$$\alpha = \frac{J_C^{ab}}{J_C^{c}} \approx 3, \tag{4.8}$$

where J_C^{ab} is the critical current density in the ab-plane and J_C^{c} is the critical current density in the c-direction. The typical values of α can range from ≈ 1.5 to ≈ 10, but the value $\alpha = 3$ at zero applied magnetic field is corroborated by our measurements, as discussed in the Results secton, below.

Albeit not perfectly cylindrical, the shielding region in Figure 4.2 (c) will be assumed to be a tube with the outer diameter R and thickness $\alpha\lambda$ in order to simplify the calculation. The time dependence of critical current density in this region is assumed exponential, as in the regions I and III.

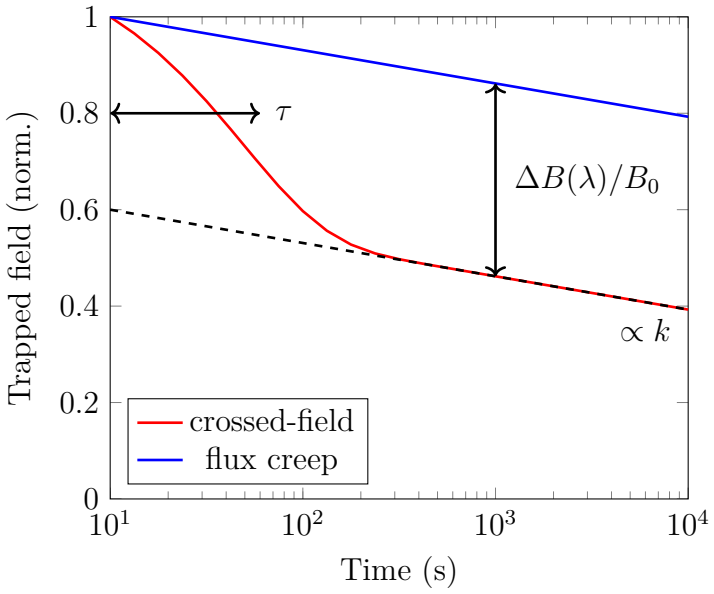

Fig. 4.3 The schematic representation of equation 4.9 (red), as compared to flux creep (blue). The characteristic time of the initial exponential decay is determined by τ, whereas the decay amount at $t \gg \tau$ is determined by λ. Here, $\tau = 50\,\mathrm{s}$ and $k = 0.05$.

Once the geometry of shielding regions is established, and the time dependence of current density is assumed exponential in the shielding regions and logarithmic elsewhere, equations 4.6 and 4.7 can be substituted into the Biot-Savart law. Integration gives the time dependence $B(t)$ as

$$B(t) = \frac{\mu_0 J_C}{2}\left\{\exp\left(-\frac{t-t_1}{\tau}\right)\left[h\,f\left(\frac{R}{h}\right) - (h-\lambda)\,f\left(\frac{R-\alpha\lambda}{h-\lambda}\right) + \lambda\,f\left(\frac{R-\alpha\lambda}{\lambda}\right)\right]\right.$$
$$\left. + \left(1 - k\log\left(\frac{t}{t_1}\right)\right)\left[(h-\lambda)\,f\left(\frac{R-\alpha\lambda}{h-\lambda}\right) - \lambda\,f\left(\frac{R-\alpha\lambda}{\lambda}\right)\right]\right\}. \tag{4.9}$$

Here, the expressions in square brackets are purely geometric: in the first term they correspond to the integral of current density over the shielding regions and in the second term they correspond to the integral over the rest of the bulk. Hence, for a given bulk geometry, equation 4.9 is simply a weighted sum of an exponential and logarithmic function and it is shown graphically in Figure 4.3.

The model, as defined by equation 4.9, is a function of several parameters. The normalised time dependence of trapped field (i.e. equation 4.9, divided by B_0) is independent of the value of J_C, hence its parameters remain τ, k, and λ.

The parameter τ determines the rate of initial decay due to current redistribution in the shielding regions as defined in Figure 4.2. Its value will depend both on the intrinsic properties of the superconductor, as well as the exact crossed-field applied. For example, the characteristic constant of current decay in the absence of pinning (as shown in equation 4.3) will be proportional to the vortex viscosity, η_v. Conversely, if the crossed-field is an AC magnetic field and its frequency increases, the value of τ will likely decrease as there are more cycles applied per unit time during which the current can decay (see the results section, below).

The parameter k is the logarithmic decay rate of current and is relevant at times $t \gg \tau$. In the case of flux creep its value approaches [30]

$$k = -\frac{\partial \log J}{\partial \log t} = \frac{k_B T}{U_0}, \tag{4.10}$$

where k_B is the Boltzmann constant, T is the temperature, and U_0 is the pinning potential in the absence of pinning. It is expected that the decay rate due to crossed-fields will approach the value of k for flux creep once the circulating current in the shielding regions has gone to zero.

The final parameter is λ, the Bean penetration depth. Its value determines the thickness of the shielding regions and the amount of decay beyond flux creep at times $t \gg \tau$. Its can be used as an input parameter for the model to predict the decay or, conversely, decay measurements can be used to infer the value of λ (see the results section, below).

4.3.2 Decay as a function of aspect ratio

The total decay beyond that of just flux creep, $\Delta B(\lambda)/B_0$ (see Figure 4.3), determined by the penetration depth λ, is of interest because it characterises the performance of the superconductor at long times – this is particularly important for practical applications requiring a stable and time-independent magnetic field. Its value can be calculated from the ratio of the geometric factor of the logarithmic term in equation 4.9, and the initial trapped field (equation 4.4), giving

$$\frac{\Delta B(\lambda)}{B_0} = 1 - \left\{ \left(1 - \frac{\lambda}{h}\right) \frac{f\left[(R - \alpha\lambda)\,/\,(h - \lambda)\right]}{f\left[R/h\right]} - \left(\frac{\lambda}{h}\right) \frac{f\left[(R - \alpha\lambda)\,/\,(\lambda)\right]}{f\left[R/h\right]} \right\}, \tag{4.11}$$

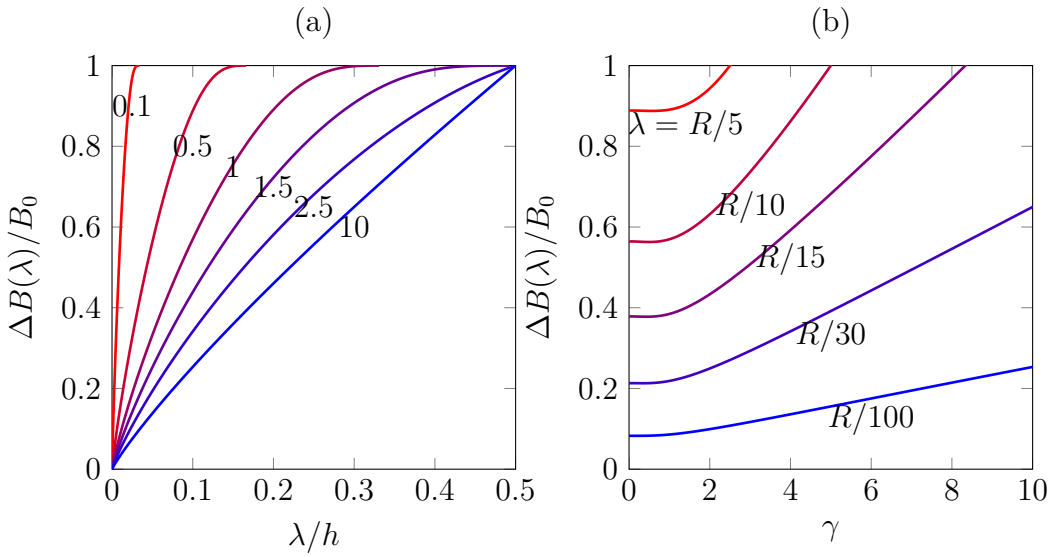

Fig. 4.4 (a) The normalised decay from equation 4.11 as a function of penetration depth for different values of aspect ratio γ. (b) The decay as a function of aspect ratio for different values of penetration depth λ.

where we use the definition of $f(x)$ from equation 4.5. The dependence of decay on the value of λ for different values of the bulk aspect ratio $\gamma = R/h$ is shown in Figure 4.4 (a).

The result seemingly favours a large aspect ratio $\gamma = R/h$ (squat and wide bulk) as the decay decreases with increasing γ, reaching its minimum value $\lambda/2h$ for $\gamma \to \infty$. This is because the trapped field, as defined by equation 4.4, is calculated at the top surface of the bulk. In long and thin bulks ($\gamma \ll 1$) all the current will circulate close to the axis of the cylinder and, after the shielding regions are formed, the untouched region II in Figure 4.2 will be moved a distance λ away from the surface. Conversely, in squat and wide bulks a large portion of the current will circulate at a large distance from the cylinder axis. Hence, after the shielding regions are formed, the currents at radius R will be moved to a distance $\sqrt{\lambda^2 + R^2} \approx R$, which will itself have a less negative impact on the trapped field.

The above result, favouring a large γ, is in contrast with the low value of γ, which is favoured in order to maximise the initial trapped field. For example, the initial trapped field in equation 4.4 can be rewritten in terms of γ as

$$B_0 = \frac{1}{2}\mu_0 J_C R \frac{f(\gamma)}{\gamma}. \tag{4.12}$$

The function $f(\gamma)/\gamma$ equals unity at $\gamma = 0$ and decreases with increasing γ. Hence, the trapped field will be maximised for a long and thin superconductor. Looking back at Figure 4.4 (a), however, increasing the value of γ by increasing the height for a given radius also leads to a decreased ratio λ/h. This is equivalent to moving leftwards in the graph, in which direction decay decreases. This effect is shown in Figure 4.4 (b), in which the radius R, and the value of λ are kept constant and the aspect ratio is varied by varying the height h. Here, the decay is lowest at a low aspect ratio γ, which means that, in fact, both the initial trapped field will be maximised and the decay minimised for long and thin bulks.

In the above analysis the calculation of decay is done by keeping either the bulk radius or its height constant, and varying the bulk height or radius, respectively, meaning there is no limitation imposed on the bulk volume. A more realistic analysis, therefore, might be one of decay as a function of aspect ratio in a bulk with a constant volume.

Assuming the volume of the superconductor is $V_0 = \pi R^2 h$, and its aspect ratio is $\gamma = R/h$, the trapped field of a fully magnetised bulk can be written as

$$B_0(\gamma) = \frac{1}{2}\mu_0 J_C \left(\frac{V_0}{\pi}\right)^{1/3} \frac{f(\gamma)}{\gamma^{2/3}}. \tag{4.13}$$

The terms in front of the fraction are all constant, hence the trapped field will be highest when $f(\gamma)\gamma^{-2/3}$ is maximum. This function indeed exhibits a maximum at $\gamma = 1.67$ (see figure 4.5 (b), black curve).

With the added constraint of a constant volume the decay (equation 4.11) can be rewritten in terms of the aspect ratio γ and the reduced penetration depth, which we define here as $\beta = \lambda/h$. The decay, then, takes the form

$$\frac{\Delta B(\lambda)}{B_0} = 1 - \left[(1-\beta)\frac{f\left(\frac{\gamma-\alpha\beta}{1-\beta}\right)}{f(\gamma)} - \beta\frac{f\left(\frac{\gamma-\alpha\beta}{\beta}\right)}{f(\gamma)}\right], \tag{4.14}$$

and is shown in Figure 4.5 (a). The normalised decay decreases with increasing γ for all values of penetration β. However, since the initial trapped field exhibits a maximum at $\gamma = 1.67$, the actual final trapped field (i.e. the initial trapped field minus the actual – non normalised – decay) exhibits a maximum as well. This is shown in Figure 4.5 (b).

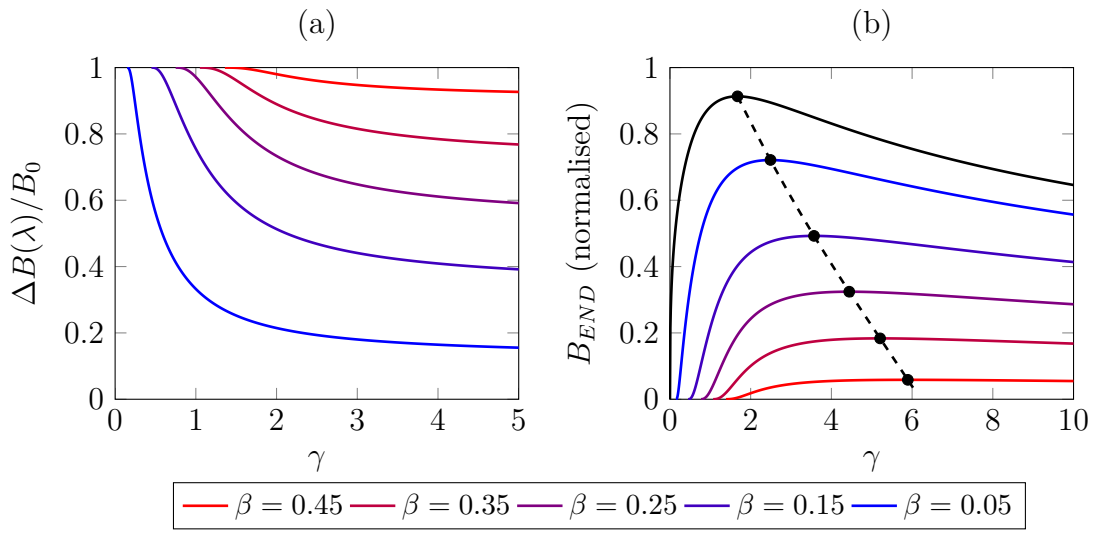

Fig. 4.5 (a) The normalised decay as a function of γ, for different values of $\beta = \lambda/h$, with the constant volume constraint. (b) The initial trapped field ($f(\gamma)\gamma^{-2/3}$, black curve), and the final trapped fields as functions of γ for different values of β. The black points represent the values of γ at which the field is maximum.

4.4 Critical current anisotropy

As discussed in the previous section the geometry of the shielding regions in the superconductor will be determined by the value of the Bean penetration depth, which will, in turn, be determined by the critical current density. Since in the crossed-field configuration the applied magnetic field is perpendicular to the *c*-axis of the bulk, a portion of the shielding currents will be induced parallel to the *c*-axis. Due to the critical current anisotropy α, however, the magnitude of these currents will be lower than those, induced in the *ab*-plane. Consequently, the Bean penetration depth will vary depending on the direction of induced currents. For this reason it is important to be able to measure the current anisotropy in order to predict accurately the geometry of the shielding regions.

A commonly employed technique of measuring the critical current density in bulk superconductors is the measurement of magnetisation loops from the thickness of which the value of J_C can be inferred. However, in the derivation of the relation between the magnetisation loop thickness and critical current density [93] it is assumed that the critical current density is isotropic. This is applicable to the situation in which the external magnetic field is applied parallel to the *c*-axis, inducing currents in the *ab*-plane, and the magnetisation parallel to the *c*-axis is measured.

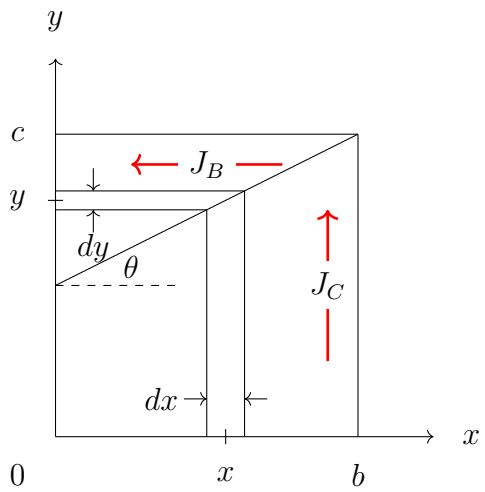

Fig. 4.6 A schematic of one quarter of the cross-section of the cuboid sample. Here, $J_B/J_C > b/c$. The surface element used in the integration is $dS = x\,dy + y\,dx$.

In order to measure the magnetisation due to the currents parallel to the c-axis, the magnetic field has to be applied perpendicular to the c-axis. Since a portion of the currents will still be induced in the ab-plane, the problem is no longer isotropic and the above approach no longer applies. In the following paragraph the relation between the an anisotropic current density and magnetisation will be derived (for more details, see [94]).

We start with a rectangular bulk of dimensions $2a \times 2b \times 2c$ parallel to the z-, x- and y- axes, respectively, and with $a \gg b \approx c$. We magnetise the superconductor parallel to the a-direction, inducing currents in the xy-plane, in which the critical current density is anisotropic. We assume the current density parallel to the b-dimension is J_B, and parallel to the c-dimension it is J_C. The current distribution of a fully magnetised superconductor is shown in Figure 4.6. Due to symmetry only one quarter of the cross-section has to be considered.

The line, separating the regions with different current directions, is defined by the equation

$$y = k(x - b) + c, \tag{4.15}$$

where $k = \tan\theta = J_C/J_B$. In the schematic in Figure 4.6 this separating line crosses the y-axis at $y > 0$, which is true if $c/b > k$, or, equivalently,

$$\frac{J_B}{J_C} > \frac{b}{c}. \tag{4.16}$$

The following derivation will be for this condition; for the case $c/b < k$ the derivation is the same, with the substitutions $b \leftrightarrow c$ and $J_B \leftrightarrow J_C$.

The magnetisation of a rectangle with this assumed current density distribution can be calculated as

$$M = \frac{1}{2V} \iiint \mathbf{r} \times \mathbf{J}(\mathbf{r})\, dV, \tag{4.17}$$

where $\mathbf{r}$ is the radial vector from the origin to the volume element dV, carrying a current density $\mathbf{J}(\mathbf{r})$. The integral is evaluated over the whole volume of the superconductor, $V = 8abc$.

Since the a-dimension (perpendicular to the xy-plane in Figure 4.6) is assumed much larger than b or c, the current is assumed unchanging with the z-axis (no demagnetisation effects due to finite size). Hence, the integral in the z-direction gives simply the height, $2a$, and the remainder is a surface integral in the xy-plane. In the region with the current $J = J_C$ the cross product to be integrated is

$$\mathbf{r} \times \mathbf{J}(\mathbf{r}) = x\, J_C, \tag{4.18}$$

and the surface element equals

$$dS = (k\,(x - b) + c)\, dx. \tag{4.19}$$

Similarly, in the region with the current $J = J_B$ the cross product is

$$\mathbf{r} \times \mathbf{J}(\mathbf{r}) = y\, J_B, \tag{4.20}$$

and the surface element

$$dS = \left(\frac{y - c}{k} + b\right) dy. \tag{4.21}$$

Inserting the above expressions into equation 4.17 the integral gives

$$M = \frac{1}{16abc} \left[2a \cdot 4J_C \int_0^b (k\,(x - b) + c)\, dx + 2a \cdot 4J_B \int_{c-kb}^{c} \left(\frac{y - c}{k} + b\right) dy \right], \tag{4.22}$$

where the factor 4 before the integrals is due to integrating only over a quarter of the cross-section. The result, then, can be written as

$$M = \frac{J_C b}{2} \left(1 - \frac{J_C}{J_B} \frac{b}{3c}\right), \tag{4.23}$$

is in agreement with the literature [94] and reduces to the expression for the isotropic case if $J_B = J_C$.

The problem with this result for the current anisotropy measurement, however, is that the value of M depends both on the value of J_B and of J_C. Moreover, the value of J_B cannot be inferred from magnetisation loop measurements in the isotropic case, in which $J_A = J_B$ and the magnetic field is applied parallel to the c-direction. This is because in the isotropic case the pinned flux vortices are parallel the c-direction with the current flowing in the ab-plane, whereas in the anisotropic case, described above, the flux vortices are all parallel to the a-direction and the current is induced in the bc-plane. Hence, the value of J_B will differ in the two cases. A prime example of this is the different values of the irreversibility field (the magnetic field, at which the magnetisation loop becomes reversible as the value of critical current density approaches zero). When the vortices are pinned in the ab-planes the irreversibility field increases significantly, as compared to the isotropic case.

The equation 4.23 must be simplified in some way so that it can be used for anisotropy measurements. A convenient way of doing this is by choosing the sample dimensions so that $c \gg b$, which means the second term in equation 4.23 can be neglected, giving

$$M = \frac{J_C b}{2}, \tag{4.24}$$

which will be accurate with a relative error of $\approx b/3c$.

4.5 Results

The sample used in this part of the study was a $GdBa_2Cu_3O_{7-\delta}$ bulk superconductor, 30 mm in diameter and 6 mm in height. The bulk was manufactured by the top-seeded melt growth technique initially 12 mm in height and subsequently cut into half along its height. The top half was used for the decay measurements, whereas the bottom half was further cut into rectangular samples and used for $J_C(B)$ measurements using a SQUID magnetometer.

The bulk used for decay measurements was initially magnetised parallel to the c-direction using FC in a 1.5 T electromagnet in a liquid nitrogen bath. After the bulk was cooled to 77 K the magnetic field was ramped to zero at a ramp rate of $0.015\,\mathrm{T\,s^{-1}}$. After magnetisation the trapped field was allowed to stabilise over a waiting period of 900 s, which was established to dissipate any heat that might have been generated during the magnetisation process. At the end of the waiting period the centre trapped

field was measured to be 0.9 T (measured using a calibrated Hall sensor mounted on the centre of the top surface). This was assumed to be the trapped field of a fully magnetised bulk, used as the initial condition for the subsequent crossed-field decay.

The bulk was inserted into the bore of a solenoid coil with its trapped field perpendicular to the axis of the coil. The coil, along with the bulk, was submerged in a liquid nitrogen bath. To generate the crossed-field an AC current was passed through the coil, its amplitude monitored throughout the measurement using a lock-in amplifier and a shunt resistor in series with the coil. The measurement consisted of the application of several thousand cycles of AC magnetic field at different amplitudes and frequencies and data acquisition of the Hall sensor voltage using a data acquisition card (DAQ) and a PC. Additionally, a Cernox® temperature sensor was mounted atop the bulk surface with which the temperature was monitored, insuring isothermal conditions.

From the bottom half of the as-grown bulk two cuboid samples were cut for the purposes of measuring the critical current anisotropy from magnetisation loops. The first sample was of dimensions $a = 2.85\,\text{mm}$, $b = 2.75\,\text{mm}$ and $c = 5.65\,\text{mm}$, and was used to measure the $J_C(B)$ dependence of the current in the ab-plane using the isotropic magnetisation equation (the magnetic field was applied parallel to the c-axis). The second sample was of dimensions $a = 4.7\,\text{mm}$, $b = 1.18\,\text{mm}$ and $c = 5.6\,\text{mm}$, and was used to determine the $J_C(B)$ dependence of current in the c-direction. Here, the magnetic field was applied parallel to the a-direction and the critical current density was inferred using equation 4.24. The error in the estimate of J_C, as determined by the ratio of the sample dimensions, was $b/3c = 7\,\%$.

4.5.1 Decay measurements

The measurements of trapped field in the crossed-field configuration for a varying amplitude of AC magnetic field, and at two different frequencies, are shown in Figure 4.7. As expected, the decay rate is largest immediately following the start of AC field application, after which its value decreases and appears to stabilise independently of the amplitude of applied field. Hence, the total amount of decay increases with the field amplitude largely because of the initial rapid decay at short times. This fits well with the picture of currents decaying exponentially in the shielding regions, the thickness of which will be directly proportional to the AC magnetic field amplitude.

Shown in black in Figure 4.7 are the least-square fits of the analytical model to the measured data, with which they appear in excellent agreement. The model, here, has three free parameters, k, τ, and λ. Their values, as determined by the fit, are shown

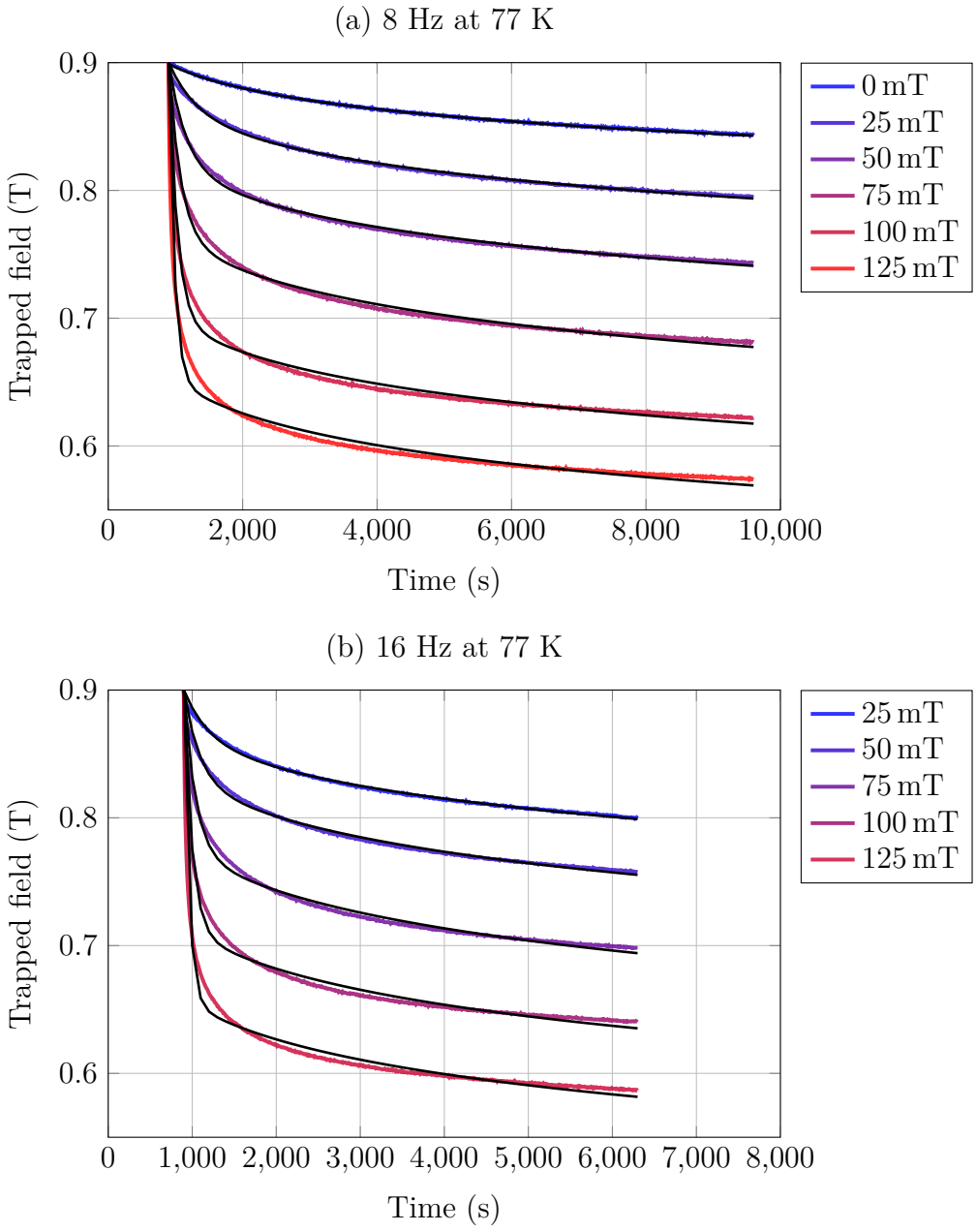

Fig. 4.7 (a) The decay of trapped field in the crossed-field configuration for varying values of AC magnetic field amplitude at a frequency of 8 Hz, and temperature 77 K. (b) Decay measurements as in (a), at the frequency 16 Hz.

in Figure 4.8. Additionally, the temperature rise due to the crossed-field, as measured by the temperature sensor on the bulk surface, is shown.

The value of τ, shown in Figure 4.8 (a), determines the rate of exponential decay of trapped field at short times immediately after the start of crossed-field application. Its value decreases with increasing crossed-field amplitude, meaning that the decay is more rapid at higher crossed-field amplitudes. It is possible that this amplitude dependence is an artefact of the fit, as the biggest discrepancy between the model at data is at $t \approx 100\,\mathrm{s}$ after the start of crossed-field application.

The value of τ also depends on the frequency of the crossed-field. In the Bean model framework the decay per cycle should be independent of frequency. Hence, the values of τ at the frequency 8 Hz should be twice the values at 16 Hz. From our data the ratio appears to be $\tau \approx 1.4$ at all amplitudes of crossed-field. It is possible that the ratio is lower than the value, predicted by the Bean model, due to the magnetisation becoming reversible in some regions, in which case the value of τ depends on the vortex viscosity η_v and is, hence, independent of frequency.

The values of k, given by the least-squares fit, are shown in Figure 4.8 (b). They represent the logarithmic decay rate at times $t \gg \tau$, the decay rate when the currents in the shielding regions have gone to zero. A larger (absolute) value of k means a larger rate of decay of trapped field

$$\frac{\partial B}{\partial t} \propto -\frac{k}{t}. \tag{4.25}$$

The values of k at all field amplitudes are within 20 % of their average value, which itself is about twice the value of flux creep (zero applied field). It is expected that the decay rate will approach a constant value across all crossed-field amplitudes. However, the fit gives a slight dependence of k on the crossed-field amplitude. A possible reason for this is a small temperature rise, which will increase with amplitude (Figure 4.8 (c)), and which will cause an increase in the rate of decay. Additionally, as with the values of τ, it is possible that this dependence of k on amplitude is an artefact of the least-squares fit.

The parameters τ and k both determine the rate of decay of trapped field. As such, their values cannot be determined very precisely from the least-square fit of the model to the data. This is because the fit minimises the residuals between the values of the model and the data, and not between their respective time-derivatives. Hence, there is no direct constraint on the local rate of decay of trapped field, possibly leading to a large error in the values of τ and k.

Conversely, the value of the penetration depth, λ, determines the amount of decay at times $t \gg \tau$, hence it is expected that the error, here, will be significantly lower.

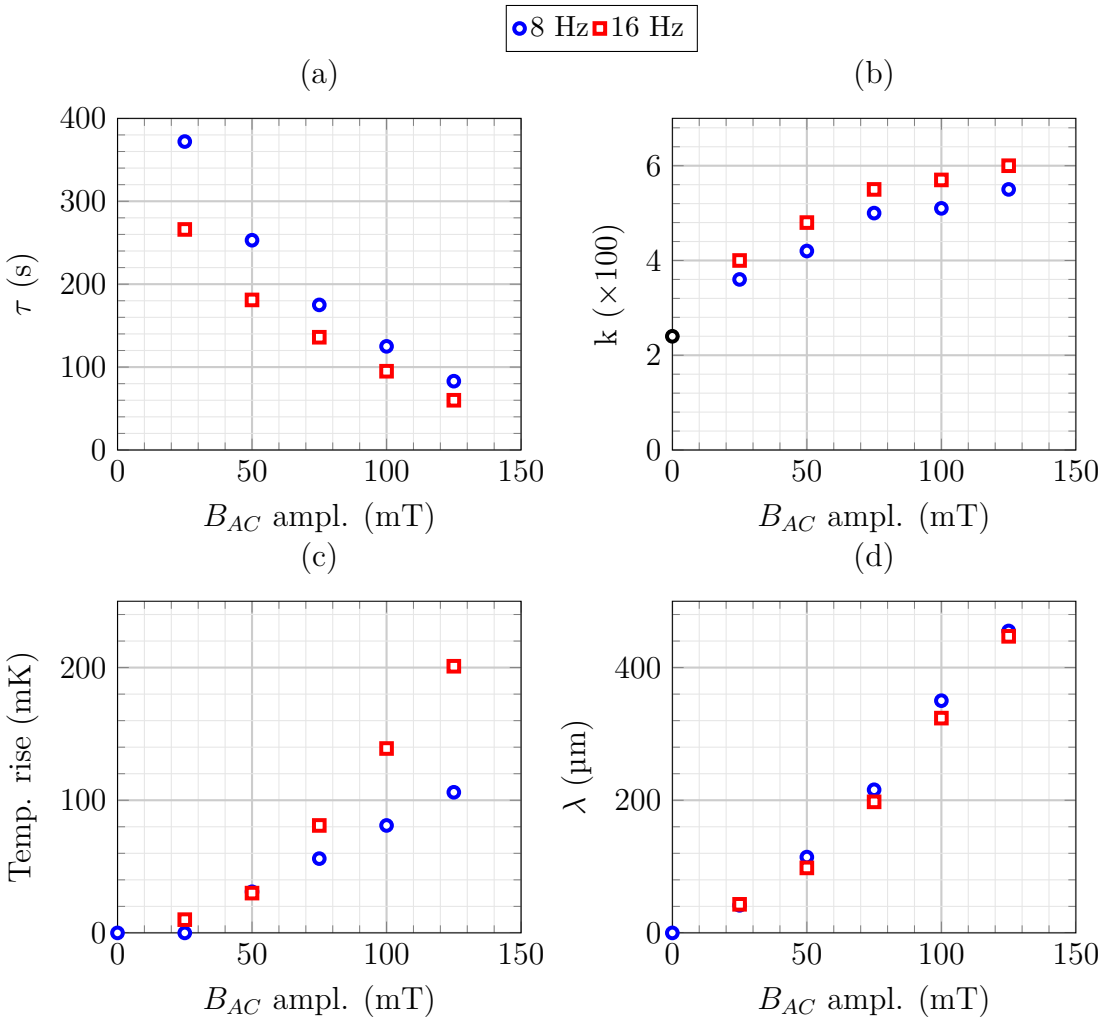

Fig. 4.8 The dependence on the crossed-field amplitude of: (a) the exponential decay rate τ, (b) the logarithmic decay rate k, (c) the temperature rise, and (d) the penetration depth λ. In (b) the black point at zero represents the flux creep decay rate.

The values of λ, extracted from the fit, are shown in Figure 4.8 (d). Increasing the crossed-field amplitude leads to an approximately linear increase in the value of λ, the penetration depth of shielding currents. This is in qualitative agreement with the prediction of the Bean model, which states

$$\lambda = \frac{B_{AC}}{\mu_0 J_C}. \tag{4.26}$$

To quantitatively corroborate this result, however, the value of $J_C(B)$ needs to be known. In the following section the $J_C(B)$ anisotropy data are presented.

4.5.2 Current anisotropy measurements

The magnetisation loop measurements, from which the critical current density was calculated, are shown in Figure 4.9 (a). When the magnetic field was applied parallel to the *c*-direction (blue symbols) the magnetisation exhibited the characteristic fishtail effect whereby there appears a local maximum at around $B = 1\,\mathrm{T}$. Conversely, the fishtail effect was not observed when the magnetic field was applied parallel to the *ab*-plane, with the magnetisation value at zero applied field reaching much lower absolute values, implying a significant critical current anisotropy, as discussed in the previous sections.

The irreversibility field values also differ in the two cases: in the anisotropic case the irreversibility field increases markedly as compared to its value in the isotropic case, where $B_{irr} \approx 5\,\mathrm{T}$. This implies that the part of the current that is induced in the *ab*-plane in the anisotropic case indeed does not have the same dependence on B as the current in the *ab*-plane in the isotropic case (as discussed in the previous section).

The increase in the value of B_{irr} when the magnetic field is applied parallel the *ab*-planes has been observed in previous studies [95–97] and has to do with the intrinsic pinning of flux vortices by the *ab*-planes. While the critical current density for $B||c$ decreases rapidly with increasing applied magnetic field, its value for $B||ab$ remains within 10 % of its self-field value between the applied magnetic fields 1 T and 5 T. In this latter case the vortices are pinned strongly in place along their entire length by the *ab*-planes, hence the increase in B_{irr}.

The critical current densities, inferred from magnetisation measurements using equation 4.23 for the anisotropic and 2.39 for the isotropic case, are shown in Figure 4.9 (b). Their values will determine the penetration depth of shielding currents, λ, parallel to the *ab*-plane and the *c*-direction. Since the critical current anisotropy, α, shown as a function of B in the inset of Figure 4.9 (b) is $\alpha \approx 3$ at self-field (zero applied field),

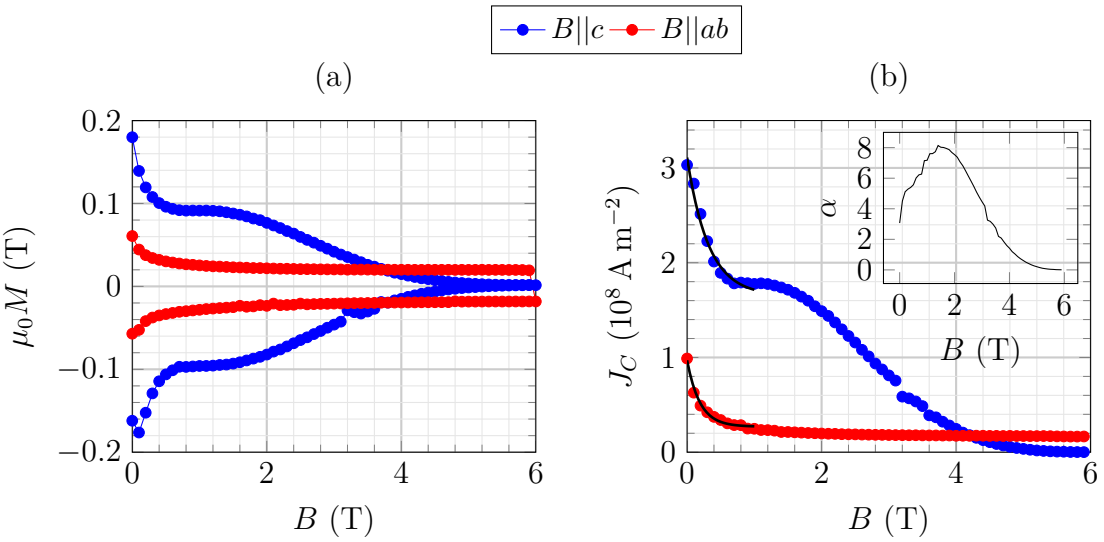

Fig. 4.9 (a) The magnetisation loop measurements of a cuboid sample, where the magnetic field was applied parallel (blue) or perpendicular (red) to the c-direction. (b) The corresponding calculated critical current densities with the exponential fits in black line. The inset of (b) is the critical current anisotropy, α.

and the maximum crossed-field amplitude is at most $B_{AC} = 125\,\mathrm{mT}$, the value of α will be treated as constant for the purposes of our analysis.

To determine the value of penetration depth from the critical current density measurements, we fit the $J_C(B)$ data with an exponential function up to the applied field value of $B = 1\,\mathrm{T}$. This suffices because none of the applied or trapped magnetic fields in our crossed-field decay measurements exceed this value. The fitted $J_C(B)$ dependence can, subsequently, be inserted into Ampere's law, with which the value of λ can be calculated and compared with the values, predicted by the fit of the analytical model to the decay data.

The exponential function, fitted to the $J_C(B)$ data, is of the form

$$J_C(B) = J_1 + J_2 \exp\left(-\frac{B}{B_1}\right), \tag{4.27}$$

where J_1, J_2 and B_1 are fitting parameters. The two fits are represented as black lines in Figure 4.9 (b), and are defined by the parameters $J_1 = 1.65 \times 10^8\,\mathrm{A\,m^{-2}}$, $J_2 = 1.46 \times 10^8\,\mathrm{A\,m^{-2}}$, $B_1 = 0.32\,\mathrm{T}$ for the isotropic case, and $J_1 = 0.27 \times 10^8\,\mathrm{A\,m^{-2}}$, $J_2 = 0.70 \times 10^8\,\mathrm{A\,m^{-2}}$, $B_1 = 0.19\,\mathrm{T}$ for the anisotropic case.

Once the critical current density is shown to obey the dependence 4.27 in the relevant applied field range, the expression can be substituted into Ampere's law,

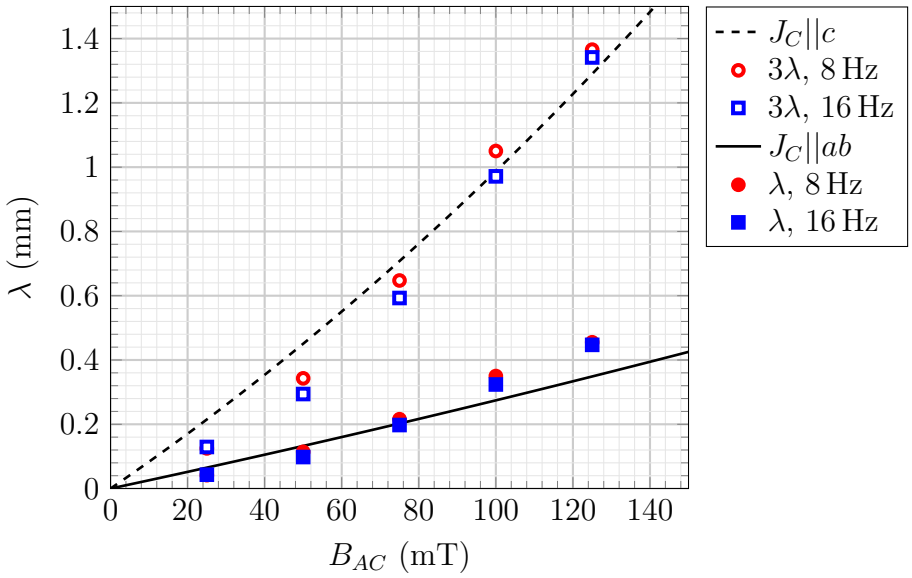

Fig. 4.10 The values of penetration depth λ, as determined by the analytical model fit to the decay measurements (symbols), compared to the values, calculated from the measured $J_C(B)$ data (equation 4.29). The values of 3λ (open symbols) appear in agreement with the value of λ, calculated from the $J_C(B)||c$ data.

$\nabla \times \mathbf{B} = \mu_0 \mathbf{J_C}(\mathbf{B})$, which can be solved in the cartesian coordinate system provided the value of λ is sufficiently smaller than the bulk radius. Subsequently, Ampere's law can be integrated with respect to B from zero to the amplitude of the applied field B_{AC}, giving the magnetic field profile as

$$B(z) = B_1 \log\left[\left\{1 + \frac{J_2}{J_1}\exp\left(-\frac{B_{AC}}{B_1}\right)\right\}\exp\left(\frac{B_0 - J_1\mu_0 z}{B_1}\right) - \frac{J_2}{J_1}\right], \tag{4.28}$$

where z is the distance measured inwards from the superconductor surface. Hence, the penetration depth, λ, can be calculated by substituting $B(z) = 0$, and solving for z, giving the result

$$\lambda = \frac{B_{AC}}{\mu_0 J_1} - \frac{B_1}{\mu_0 J_1}\log\left(\frac{J_1 + J_2}{J_1 + J_2\exp\left(-B_{AC}/B_1\right)}\right), \tag{4.29}$$

which reduces to the Bean penetration depth for a constant J_C, $B_{AC}/\mu_0 J_C$, by substituting $J_1 = J_C$ and $J_2 = 0$. The result can be used to validate the values of λ, given by the analytical model fit to the crossed-field decay data. This is shown in Figure 4.10.

The values of λ given by the model appear in excellent agreement with those given by $J_C(B)$ data. In essence, this means that measurements of crossed-field decay can be

used to determine unambiguously the size of the shielding regions in the superconductor provided the geometry of the superconductor and its critical current anisotropy is known.

Also shown in Figure 4.10 is the comparison between the penetration depth, calculated from the $J_C(B)||c$ data, and the value of $\alpha\lambda$, given by the model fit (where $\alpha = 3$). The agreement, here, implies that the choice of $\alpha = 3$ is justified.

4.5.3 FEM simulation

To justify the assumptions about the geometry of shielding regions in the derivation of the analytical model, FEM simulations were performed using the commercial package Comsol Multyphysics 5.3a. The majority of the modelling work was done with the help of Fernando Perez.

For the purposes of simplifying the FEM simulation, and to reduce the computation time, the bulk was approximated in the 2D infinite slab geometry, shown schematically in Figure 4.11. The dimensions of the slab were chosen so that the slab cross-section was equal to the cross-section of the bulk: 30 mm in width (along the x-axis) and 6 mm thick (along the z-axis). This geometry is convenient for modelling the real 3D geometry of bulk superconductors as it is sufficiently physical to capture qualitatively the superconductor behaviour caused by changing magnetic fields. However, a drawback of this method is its inability to capture the critical current anisotropy of the material. As an example, in the crossed-field configuration the shielding regions formed due to the external AC magnetic fields will have currents flowing both in the ab-plane and in the c-direction. This cannot be modelled in the 2D infinite slab geometry.

The slab was magnetised by zero-field cooling (ZFC) with the magnetic field applied along the z-axis, and the trapped field parallel to z calculated 0.5 mm above the top surface of the slab (this is to account for the active area of the Hall sensor in the experimental setup being slightly above the bulk surface). The critical current density was assumed independent of magnetic field (Bean model), and its value chosen so that the trapped field of the model matched the experimentally measured trapped field of a fully magnetised bulk.

The ZFC procedure itself consisted of ramping the applied magnetic field from zero to 3 T over 150 s, and subsequently ramping it back to zero with the same ramp rate. The temperature of the slab was set to 77 K and was assumed constant, hence no thermal model was employed (the heat generation $Q = \mathbf{E} \cdot \mathbf{J}$ was assumed negligible).

After the magnetisation procedure the slab was allowed to undergo flux creep for a period of 900 s (to match with experiment), after which the external AC magnetic

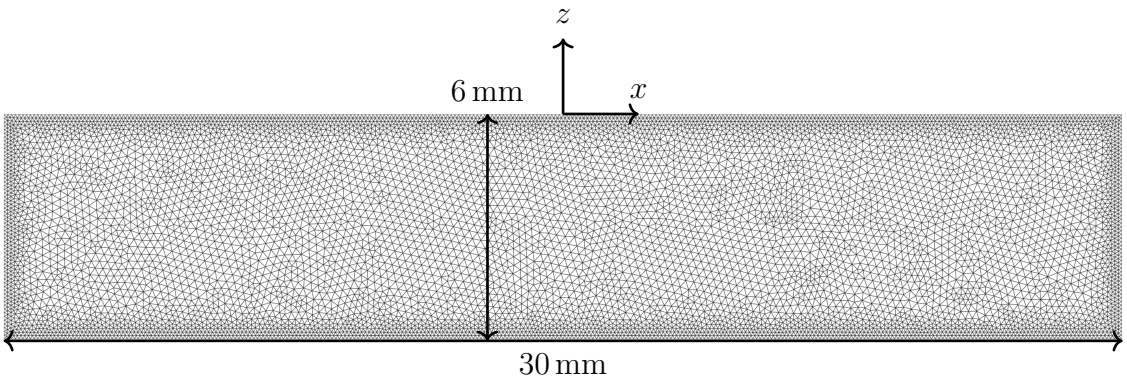

Fig. 4.11 The meshed slab with 7829 degrees of freedom (nodes), along with the chosen coordinate system. The mesh is finer close to the edge of the slab as there the current density is expected to vary the most after the crossed-field is applied.

field (crossed-field) was applied perpendicular to the z-axis at a frequency of 8 Hz and varying amplitudes from 25 mT to 125 mT. The resulting decay of trapped field is shown in Figure 4.12.

The trapped field decay was simulated for a total duration of 50 s, or 400 cycles at a frequency of 8 Hz. Qualitatively the FEM simulation captures the experimental data well as the simulated decay rate and amount both increase with the crossed-field amplitude.

Quantitatively there is some discrepancy between the model and the data. The measured initial decay rate immediately after the start of the crossed-field application is much lower than predicted by FEM, whereas, at $t = 950$ s, the measured decay rate is greater than predicted by FEM. In terms of the analytical model this means that the FEM predicts a more rapid decay of current in the shielding regions, than what is indicated by experiment.

A possible explanation for this discrepancy is the choice of field-independent value of J_C. In reality, as the trapped magnetic field decays, the local magnetic field everywhere in the superconductor will change, hence the value of J_C can change as well. This means that the shielding ability of the superconductor will likely change throughout the duration of the application of crossed-field.

Another possible source of error is the constant value of $N = 20$ in the **E-J** power law, which determines the rate of decay in the regions beyond the penetration depth of shielding currents. In reality the value of N may depend on the local magnetic field, as well as the crossed-field amplitude and frequency. Additionally, while the **E-J** power law serves as a good approximation of the Bean model, it remains only an

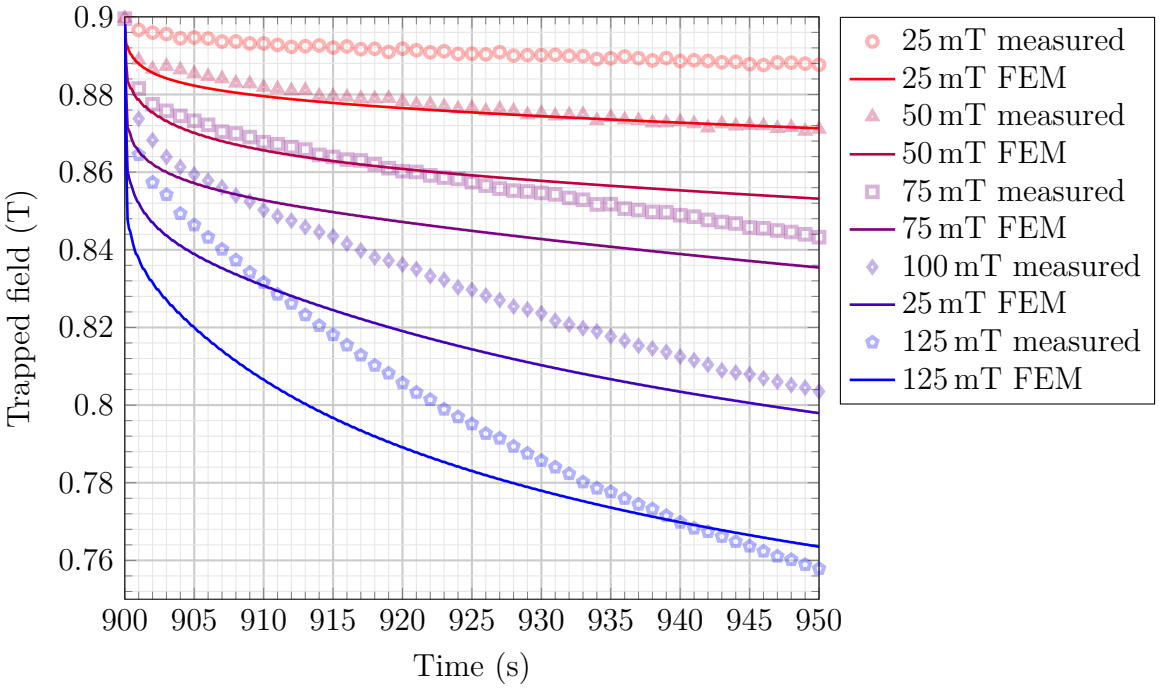

Fig. 4.12 The comparison of trapped field decay, predicted by FEM, with the measured decay.

approximation. It is possible that the exact relation between electric field and current density differs from the **E-J** power law, which will lead to a discrepancy between the observed and simulated rate of decay.

The FEM analysis assumes there is no temperature rise in the bulk and, while the measured temperature on the bulk surface remains lower than 200 mK at all crossed-field amplitudes (Figure 4.8 (c)), the temperature rise in the centre of the superconductor will be higher. Hence, the value of J_C will likely decrease with time and this behaviour will not be captured by the FEM simulations.

Finally, the FEM simulation is two-dimensional, approximating the bulk superconductor with an infinite slab geometry. This means that, while in reality the current loops must always be completed, this is not the case in the infinite-slab geometry. Hence, there will be no current flowing in the c-direction and there is no way to capture the critical current anisotropy.

In addition to the decay of trapped field over time, the current distribution across the slab cross-section can be compared with the assumed shielding regions in the derivation of the analytical model. The distribution of current density after 10 cycles of applied crossed-field is shown in Figure 4.13. The distribution labelled 0 mT is of a

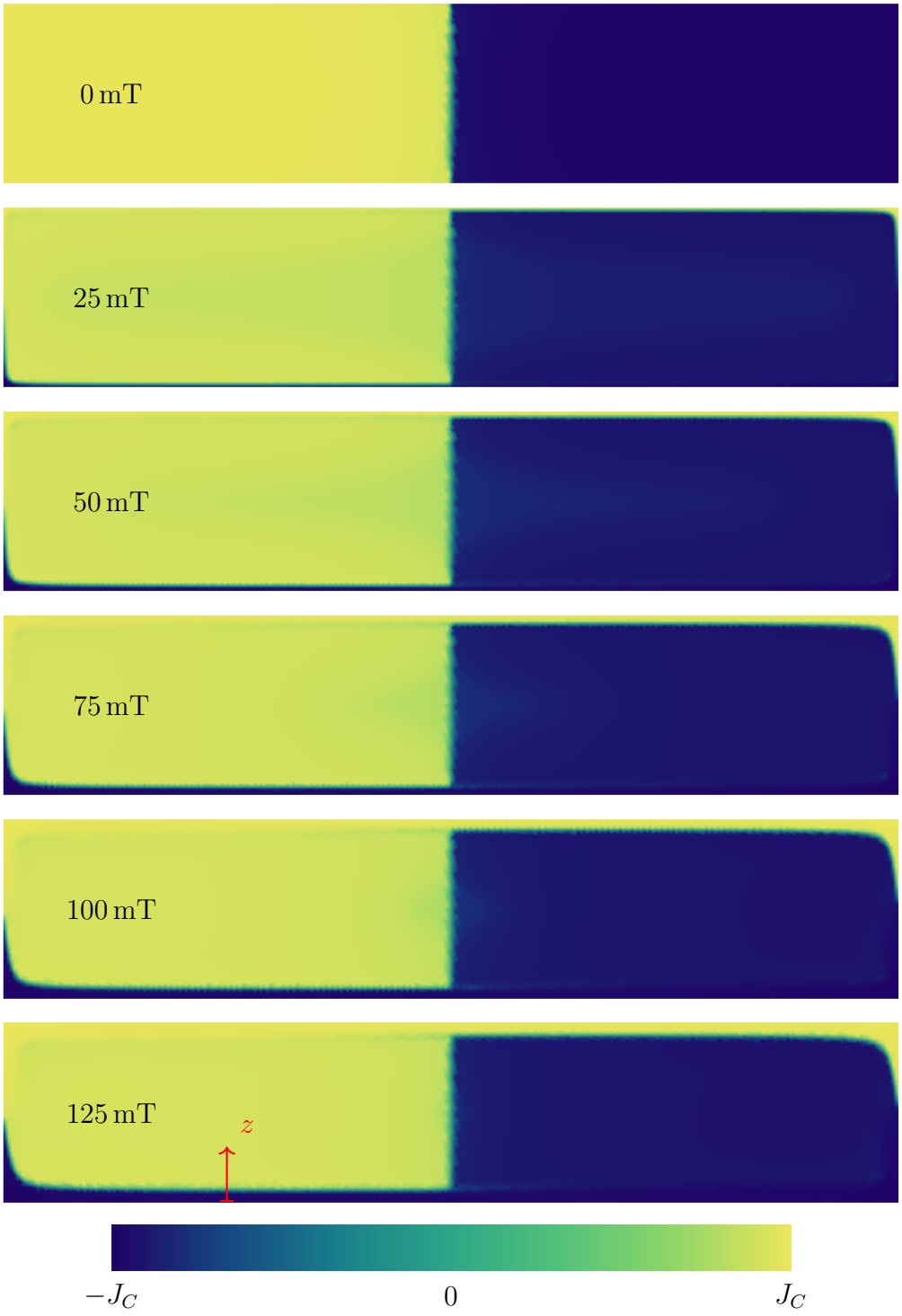

Fig. 4.13 The current density distribution after 10 cycles of crossed-field with varying amplitudes at 8 Hz. The arrow in red corresponds to the z-axis in Figure 4.14 (a).

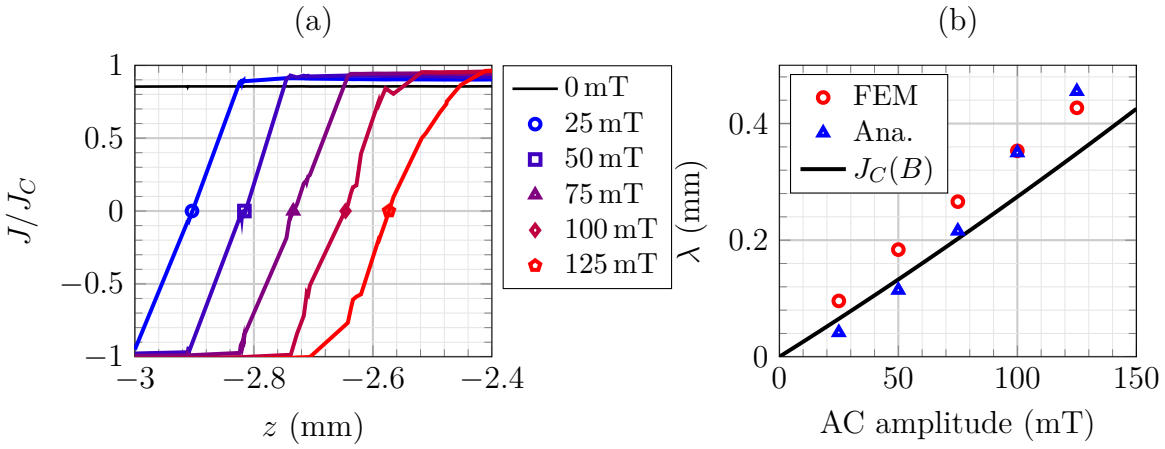

Fig. 4.14 (a) The current density as a function of distance (parallel to z; red arrow in Figure 4.13), averaged over the area $x = -8\,\text{mm}$ to $x = -7\,\text{mm}$. (b) The values of penetration depth given by FEM simulation, the analytical model, and calculation from the measured $J_C(B)$ dependence.

fully magnetised slab immediately before the crossed-field is applied. As expected, the current approaches its maximum value $\pm J_C$ everywhere across the cross-section. This is equivalent to the azimuthal current flow in a cylindrical bulk.

The current distribution labelled from 25 mT to 125 mT are of the slab after 10 cycles of applied crossed-field at each respective amplitude. It is apparent that the shielding regions are induced from the top and bottom surfaces of the slab, corresponding to the shielding regions of thickness λ in the derivation of the analytical model. The thickness, here, is almost constant across the width of the slab due to the slab's aspect ratio - there are only minor demagnetisation effect due to the field lines curving at the edges of the slab.

As predicted by the analytical model, the thickness of the shielding regions increases with the crossed-field amplitude. The circulating current beyond the thickness of the shielding regions appears unperturbed which is, again in alignment with the analytical model. What remains is to compare the values of the penetration depth, predicted by the model, with the values, given by FEM. Here, we define the penetration depth as the average distance from the slab surface, at which the current density changes sign (shown in Figure 4.14 (a)). The comparison of the penetration depth given by the analytical model and FEM, is shown in Figure 4.14 (b). They appear in good agreement.

4.6 Discussion

In this chapter I derived an analytical model with which the decay of trapped field in the crossed-field configuration can be analysed. The model is based on the different time dependence of the current, contributing to the trapped field, depending on whether it is within the penetration depth of the crossed-field of the surface of the superconductor.

The model, initially general, is applied to the case of a cylindrical bulk superconductor and the specific geometry of the induced shielding regions. The time dependence of trapped field is derived using the Biot-Savart law, giving an analytical expression, which itself can be fitted to measured data.

I have shown that the model is able to reproduce the measured data remarkably well, or, equivalently, is able to determine the value of its parameters, namely the penetration depth λ, by a least-square fit to the measurements. I have shown that the values of λ, predicted by the analytical model, FEM simulations, and calculated from the measured $J_C(B)$ dependence, are all in good agreement.

I have derived the analytical model under the assumption of isothermal conditions. This will not always be the case, as demonstrated by our temperature measurements on the surface of the bulk. As shown in Figure 4.8 (c), the temperature rise increases with the crossed-field amplitude and frequency. Hence, if the crossed-field amplitude or frequency increase sufficiently to cause the generated heat, $Q = \mathbf{E} \cdot \mathbf{J}$, to overcome the cooling power of the cryogenic system, the temperature of the superconductor will increase and the assumption of the isothermal conditions will become invalid.

Regardless, if the temperature of the superconductor stabilises at a temperature $T < T_C$, the model may still be valid, with only minor reconsiderations in its derivation. Once the temperature stabilises isothermal conditions may, again, be assumed since the heat will be generated in the shielding regions close to the superconductor surface, where the cooling power of the cooling system is highest. Then, once the initial transient has stabilised and the superconductor temperature stabilises, the model can be derived as above, provided that the $J_C(B)$ dependence at that temperature is known.

In terms of the wider scope of this thesis, the results presented here are important as they elucidate the mechanism of decay of trapped field within the range of AC amplitudes and frequencies studied. Current redistribution is shown to be the main cause for decay, with temperature rise due to AC losses not playing as significant a role. Hence, the decay of trapped field at long times increases approximately linearly with the AC field amplitude due to the linear increase of the Bean penetration depth, λ_B, and, with it, the thickness of the shielding regions in the periphery of the sample.

Thus, potential mitigation measures can be discussed in terms of the reduction of λ_B; if λ_B decreases, the shielding regions decrease and the decay of trapped field will be lower. One way of accomplishing this (without changing the material studied) is simply by reducing the operating temperature of the superconductor. This will lead to an increase in the critical current density, and a lower penetration depth. Controlling the temperature as an effective way of mitigating trapped field decay is discussed in the following chapter.

Chapter 5

Parallel-field decay in bulk superconductors

5.1 Background

In this chapter the decay of trapped field in the parallel configuration will be discussed. Here, the AC magnetic field is applied parallel to the direction of the trapped field of a bulk superconductor. The effect of the parallel field on the superconductor will be discussed in terms of trapped-field decay and of temperature rise due to heat generation. In the second half of the chapter the parallel field configuration will be compared with the crossed-field configuration in terms of decay of trapped field, and an effective decay mitigation measure - controlling the temperature of the superconductor - will be discussed.

The parallel-field configuration is an axially symmetric problem provided that the geometry of the superconductor is also axially symmetric. The applied magnetic field is perpendicular to the current density everywhere, meaning that the Lorentz force on the flux vortices in the superconductor is simply $F_L = BJ$, where B is the magnetic field amplitude and J the current density.

Hence, the simplest model with which the parallel-field configuration can be described is that of a cylinder of infinite height (Figure 5.1) in which the currents flow in the azimuthal direction and the external magnetic field is applied parallel to the cylindrical axis (z-axis). Due to symmetry this can be treated as a one-dimensional problem because the only non-zero component of trapped magnetic field (and of magnetisation) will be parallel to z. Equivalently, the only non-zero component of induced current density will be in the azimuthal direction. Ampere's law in one dimension in

cyllindrical coordinates, (r, ϕ, z), can be written as

$$-\frac{\partial B_Z}{\partial r} = \mu_0 J_\phi. \tag{5.1}$$

Within the Bean model framework the current density, J_ϕ, can assume the values $\pm J_C$ and zero, giving the trapped magnetic field of a fully magnetised cylinder as

$$B(r) = \mu_0 J_C(r_0 - r) = B_0 - \mu_0 J_C r, \tag{5.2}$$

where $B_0 = \mu_0 J_C r_0$ is the centre trapped magnetic field (and is equal to the penetration field, B_P), and r_0 is the cylinder radius. This is shown in Figure 5.1 (a) (black line).

Consequently, if the cylinder is exposed to an external AC magnetic field of amplitude B_A, the trapped field will decay by B_A in the first quarter period during which the applied magnetic field is anti-parallel to the trapped field (the decayed trapped field profile is shown in red in Figure 5.1 (a)). Subsequently, the trapped field will remain at a constant value and will be no longer affected by the applied AC magnetic field. This is due to the formation of shielding regions below the surface of the superconductor up to the Bean penetration depth of the applied magnetic field (shielding regions are shown in gray shading in Figure 5.1 (a)). The decay of trapped field over time is shown in Figure 5.1 (b).

Going from the infinite-cylinder geometry to a cylinder of height h complicates the problem because the magnetic field lines will now be curved based on the current density distribution in the superconductor, which will, itself, now become a function of the z-coordinate ($J = J_C$ for $|z| \leq h/2$, $J = 0$ elsewhere). The problem remains cylindrically-symmetric, however, which means that the magnetic field due to an arbitrary current density distribution can be calculated using the Biot-Savart law in two dimensions. As an example, the z-component of magnetic field due to a fully magnetised bulk superconductor of height h and radius r_0, is shown in Figure 5.2 (a). This distribution is calculated by numeric integration of the Biot-Savart law. For comparison, Figure 5.2 (b) shows the magnetic field of the same bulk, but in which the current density is zero for $r > 0.8r_0$. This will be the case, for example, when the external AC magnetic field penetrates from the outer surface and causes the currents in the shielding region of thickness $0.2r_0$ to go to zero (on average, over one period of AC field). The corresponding magnetic field profiles are shown in Figure 5.2 (c) and (d).

In principle, the calculation of magnetic field from a given current density distribution is straightforward. However, for an accurate simulation of change of trapped field

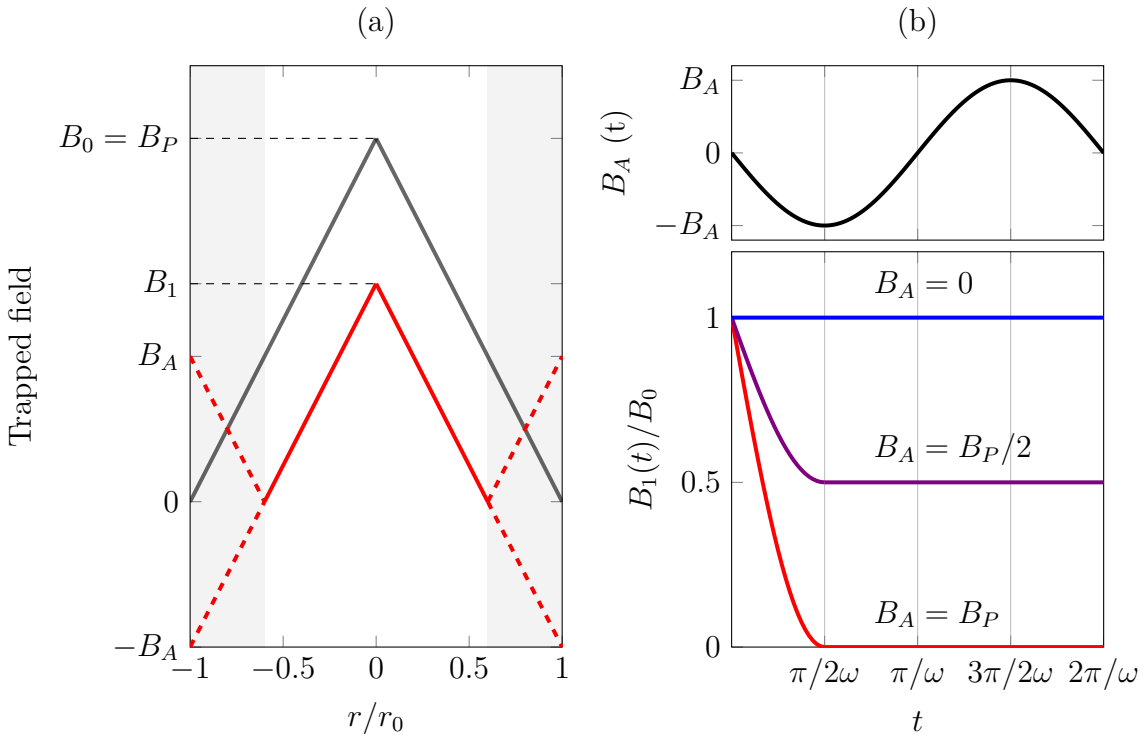

Fig. 5.1 (a) The trapped field profile of a fully magnetised infinite cylinder (black), and the profile after the application of an AC magnetic field (amplitude B_A) parallel to the direction of trapped field. The gray shading indicates shielding regions in which the trapped field profile oscillates between the upper and lower red dashed lines. (b) Top: the applied AC magnetic field waveform. Bottom: The decay of trapped field for different amplitudes of applied AC field.

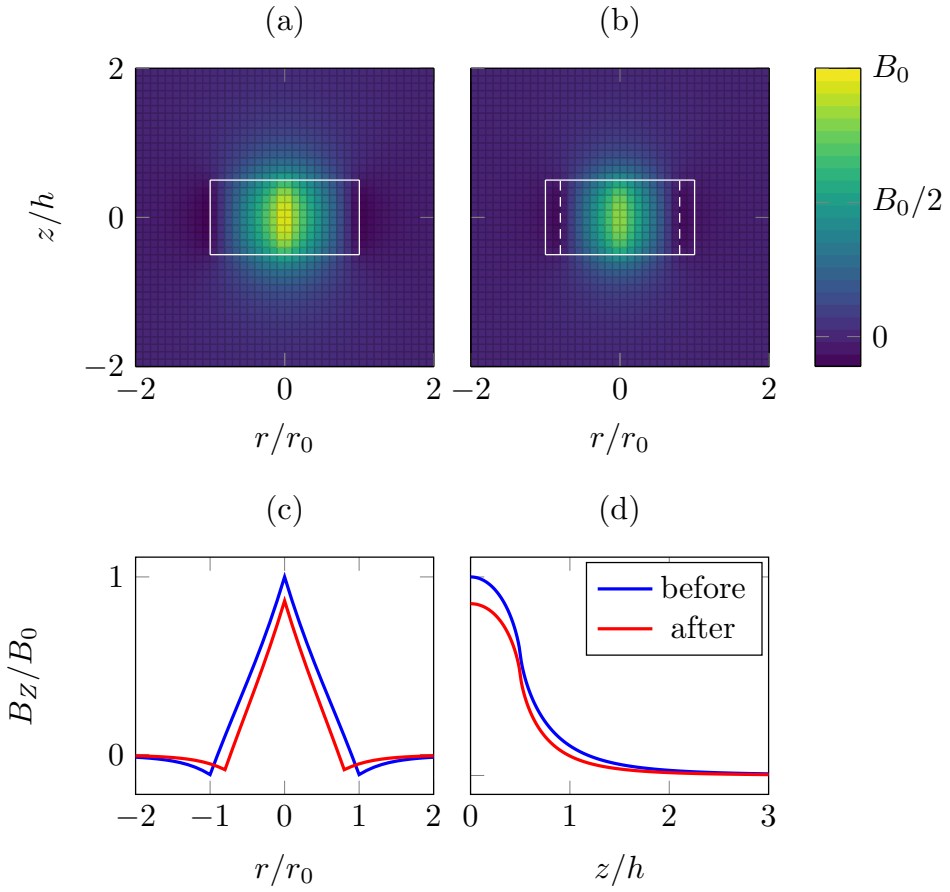

Fig. 5.2 (a) The B_Z distribution in a fully magnetised bulk. (b) The B_Z distribution in a bulk in which the current density for $r > 0.8r_0$ has gone to zero (indicated by the white dashed lines). (c) The magnetic field profile for a fully magnetised bulk from (a) (blue) and a partially demagnetised bulk from (b) (red) (at $z = 0$). (d) The dependence of B_Z on the distance from the centre, z, for both cases (at $r = 0$).

due to an external changing magnetic field, the induced current density itself must first be calculated. For this reason the Biot-Savart law has to be used in conjunction with Faraday's law, Ampere's law, and an **E-J** relation. To this end FEM simulations are typically employed in a 2D axially-symmetric formulation [98–100].

Based on this analysis above, the initial trapped field, B_0, will decay to zero if the amplitude of applied magnetic field is equal to or greater than the penetration field, $B_A \geq B_P$. However, experiments also show that an applied magnetic field with an amplitude much smaller than the penetration field can cause a full decay of trapped field [57]. The reason for this is temperature rise.

Due to the hysteretic behavior of the superconductor the AC magnetic field will induce losses in the superconductor, which can be calculated from the area of the magnetisation loop or, equivalently, from the scalar product of the induced electric field and current density,

$$Q = \int \mathbf{M}\, d\mathbf{B} = \mathbf{E} \cdot \mathbf{J}. \tag{5.3}$$

For an infinite cylinder the losses per unit volume per cycle evaluate to

$$Q = \begin{cases} \frac{2B_A^2}{\mu_0}\left(\frac{2\beta}{3} - \frac{\beta^2}{3}\right) & \beta < 1, \\ \frac{2B_A^2}{\mu_0}\left(\frac{2}{3\beta} - \frac{1}{3\beta^2}\right) & \beta > 1, \end{cases} \tag{5.4}$$

where $\beta = B_A/B_P$. This is derived in Appendix B in two ways, demonstrating the equivalence 5.3.

The heat generated, Q, is an increasing function of the applied AC magnetic field amplitude. Additionally, since it is evaluated per cycle, the total heat generation will increase with AC frequency. Hence, if the amplitude or frequency of the AC field is sufficient, the heat generation may overcome the cooling power of the cryogenic system, causing a temperature rise in the superconductor. This, in turn, will lead to a reduction in J_C, and to decay of trapped magnetic field. Controlling the temperature of the superconductor, therefore, remains an important problem to be addressed.

In the following section the relevant literature will be discussed. The studies focus in large part on the experimental determination of trapped field decay due to an applied parallel AC magnetic field, where heat generation and temperature rise are pivotal parameters to be understood. Next, the measurement data of trapped field decay in a GdBCO bulk are presented and discussed. Here, discussion focuses on the means by which controlling the temperature helps to reduce decay. Lastly, the parallel configuration will be compared with the crossed-field configuration in terms of trapped field decay and its mitigation.

5.2 Previous studies

In order to ascertain the viability of high temperature bulk superconductors to act as quasi-permanent trapped-field magnets in rotating machines, Tsuda *et al.* [101] investigated the influence of a parallel AC magnetic field on the trapped field in an YBCO bulk superconductor in a liquid nitrogen bath at 77 K.

In their experiment the authors used FC to magnetise a 45 mm diameter, 3 mm thick YBCO bulk, giving a peak trapped field of 80 mT. The bulk was subsequently exposed to a parallel AC magnetic field and the decay of trapped field was measured. The trapped field was shown to decay significantly in the first few periods of AC field application, after which the decay rate reduced markedly. This is attributed to the formation of shielding regions, as discussed in the previous section, and to the successful removing of heat, generated in the superconductor, avoiding a significant temperature rise.

Ohyama *et al.* [102] performed additional experiments with the same setup to ascertain the influence of the amplitude and frequency of applied field on the decay of trapped field. It was found that increasing the amplitude of the AC magnetic field leads to a greater total decay of trapped field (due to the increased thickness of the shielding regions). Increasing the frequency was found to lead to a greater decay rate per unit time, but to a lower decay rate per unit cycle. This is explained as being due to a lower penetration depth at a higher frequency. In particular, a higher rate of change of magnetic field, $\partial B/\partial t$, leads, as per Faraday's law, to a larger electric field, E. This corresponds, in turn, to a larger value of current density (as per the EJ-power law). Hence, the penetration depth at a higher frequency of AC magnetic field will be decreased, leading to a lower decay per cycle.

As an example, from Faraday's law it follows that

$$E \propto \frac{dB}{dt}\Delta x \propto \omega B \Delta x, \tag{5.5}$$

where Δx is a distance over which E changes and ω is the frequency of AC magnetic field. Simultaneously, the relation between the electric field, E, and the Bean penetration depth, $\lambda = B/(\mu_0 J)$, can be approximated with the EJ-power law

$$\frac{E}{E_0} = \left(\frac{J}{J_C}\right)^N. \tag{5.6}$$

Substituting Faraday's law into the EJ-power law, the induced current density reads

$$J \propto J_C \left(\frac{\omega B \Delta x}{E_0} \right)^{1/N}, \tag{5.7}$$

from which it can be seen that the penetration depth is a decreasing function of frequency

$$\lambda \propto \omega^{-1/N}. \tag{5.8}$$

Ogawa *et al.* [103] performed measurements of AC loss in a 45 mm diameter, 20 mm thick YBCO bulk using a pick-up coil method. They found that the losses are hysteretic and they are larger if the bulk has previously been magnetised, than if it is in a non-magnetised state. This is explained as being due to a reduced penetration field B_P as a consequence of a lower critical current density in the presence of a trapped field.

Subsequently, the authors [57] compared the influence of a crossed-field to that of a parallel field on the trapped field decay. They found that, while generally the crossed-field configuration leads to a greater amount of decay of trapped field, the trapped field can be completely erased by the parallel field even if its amplitude is lower than the full penetration field. This is attributed to the temperature increase above T_C in the superconductor. A study by Yamagishi *et al.* [104] confirms this by noting that the temperature of the superconductor can indeed rise to above T_C as a consequence of an applied AC magnetic field, provided its frequency and amplitude are sufficient (with the amplitude still below B_P).

It can be inferred from these studies that there are two regimes of decay in the parallel field configuration. The first is one in which the temperature rise is negligible, this leads to the decay of trapped magnetic field in the first few cycles of applied AC field, after which the decay rate decreases significantly. This is explained well within the Bean model framework. The second regime is one in which the decay is dominated by the temperature rise. The AC field generates heat in the superconductor, which itself overcomes the cooling power, leading to an increase in temperature and a decrease in J_C. This leads to a decay of trapped field, in some cases to zero (if the temperature exceeds T_C). Hence, it is shown that controlling the temperature is crucial in controlling the decay of trapped field. Moreover, as we shall see below, reducing the operating temperature below that at which the superconductor is magnetised, proves an efficient measure for markedly reducing decay.

Zushi *et al.* [105] showed the importance of effective cooling of the superconductor in reducing the decay of trapped field. The authors compared the decay of trapped field

for a bulk in a liquid nitrogen bath first without and then with a layer of polystyrene insulation. An epoxy-impregnated YBCO bulk with a peak trapped field of 0.31 T was exposed to a parallel AC magnetic field at varying amplitudes. For the non-insulated case the decay was limited to no more than 20 % for all amplitudes of AC field up to 100 mT (peak). Conversely, the decay of trapped field in the polystyrene-insulated case reached 100 % at a threshold AC field amplitude of 50 mT. Several later studies [106–109] have focused on analysing the dependence of trapped field decay on temperature, with similar conclusions about the detrimental effect of an increased temperature in the superconductor.

5.3 Results

The bulk sample used in this part of the study was a 16 mm diameter, 8 mm thick $GdBa_2Cu_3O_{7-\delta}$ bulk superconductor, manufactured with the top-seeded melt growth technique. Its centre trapped field following FC at 77 K was 0.6 T. This sample was chosen because its smaller diameter and smaller penetration field (as compared with the likely size of bulks used in real practical applications) allowed for a sweep of a larger portion of the parameter space since the range of AC magnetic field amplitudes up to the penetration field is of interest.

5.3.1 Determining the maximum trapped field using PFM

Firstly, PFM was used to magnetise the bulk at different temperatures, and using different pulse sequences, in order to find a condition as close as possible to the fully magnetised bulk after magnetisation with FC - subsequently, this would be used to magnetise the bulk prior to exposing it to AC magnetic fields and measuring decay. Magnetising with PFM (instead of FC) gives a more realistic picture of the performance of the bulk in a real machine where FC would not be practical.

Since temperature rise in the superconductor during PFM impedes the maximum achievable trapped field, it has been shown [110] that a multi-pulse PFM process, in which the heat is generated in sequential steps (leading to a lower maximum temperature rise) helps to increase the final trapped field. For this reason, both the single-pulse and the multi-pulse PFM techniques were employed and the subsequent trapped fields compared. As we shall see below, single-pulse PFM proved sufficient to magnetise the sample to its full capacity.

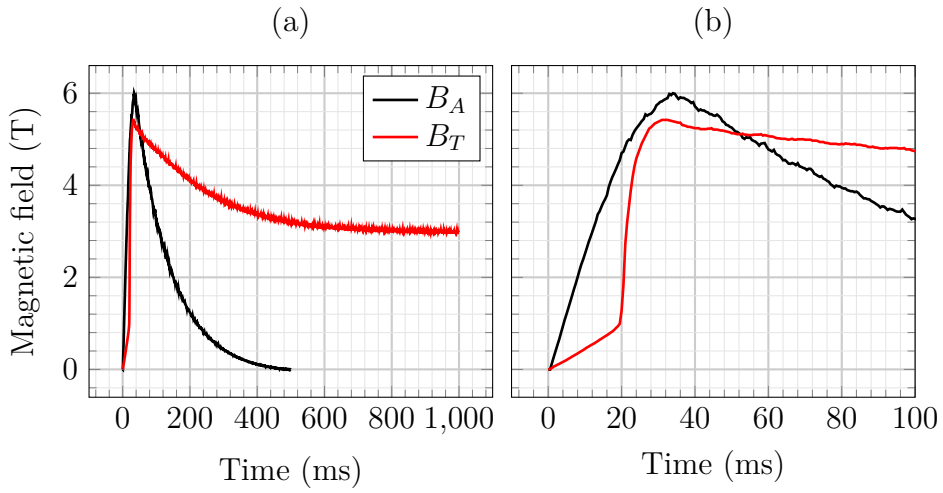

Fig. 5.3 The time dependence of the applied (B_A) and trapped (B_T) field during the first (a) 1000 ms and (b) 100 ms after the start of the pulse. In (b) the cusp of the red line at 20 ms represents the start of the flux jump.

An example time dependence of the trapped field during PFM, as measured with a Hall sensor mounted on the centre of the top surface of the sample, is shown in Figure 5.3. Here, the temperature of the bulk is 30 K, the applied pulse amplitude is 6 T and the trapped field after PFM is 3 T. Typically with zero field cooled magnetisation (ZFC), of which PFM is a variant, the applied magnetic field has to be twice the final trapped field. However, with PFM the trapped field can be significantly reduced due to additional heat generation during the rapid rise of external magnetic field. It can be seen, here, how the flux jump effect (especially evident in Figure 5.3 (b), red line, at 20 ms) can be utilised with PFM in order to maximise the final trapped magnetic field. Despite the likely additional heat generation the trapped field remains half the maximum applied field. This is attributed, in part, to the sample volume, which appears sufficiently small so as not to cause the total heat generation to lead to a significant temperature rise.

This PFM procedure, of which the above is an example, was performed across a range of different temperatures from 30 K to 77 K, and pulse amplitudes up to 6.5 T. The resultant centre trapped magnetic fields in the bulk are shown in Figure 5.4 (a). The data points shown were obtained by averaging the measured Hall voltage over a period of 10 s, and the error bar is smaller than the point size.

The trapped field at a given temperature initially increases with the applied pulse amplitude, reaches a peak value, and subsequently decreases when the pulse amplitude

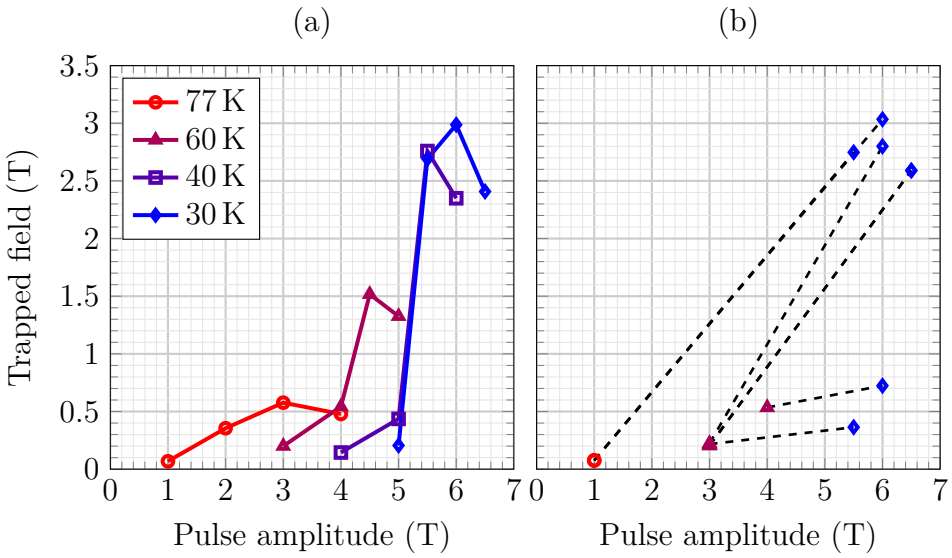

Fig. 5.4 (a) The centre trapped fields in bulk A after single-pulse PFM, at different temperatures. (b) The trapped fields after a two-pulse sequence. The trapped field values after each of the respective pulses in a sequence are connected with the dashed line.

is further increased. This is a commonly observed feature of trapped field after PFM [35, 111].

At small pulse amplitudes the magnetic field does not penetrate into the centre of the superconductor, leading to a small field trapped in the centre. Increasing the pulse amplitude leads to an increased trapped field as predicted by the Bean model. Subsequently, at a critical value of pulse amplitude [67] there is a sudden significant increase in trapped field. This is due to the applied field penetrating the superconductor suddenly in what is known as the flux jump effect (as seen in Figure 5.3). At this critical value of applied field amplitude the trapped field reaches its peak value. Increasing the amplitude further is detrimental to the trapped field because, while the flux jump still occurs, the heat generation is increased due to an increase in applied field, leading to further temperature rise and to a lower trapped field.

The trapped field can be seen to increase with decreasing temperature. Lowering the temperature will lead to an increase in J_C and, in turn, to an increase in trapped field. However, the heat generation, $Q = \mathbf{E} \cdot \mathbf{J}$, increases with J_C as well, thus there likely exists a threshold temperature below which the value of J_C is high enough so as to be detrimental to the trapped field.

Next, to maximise the trapped field a two-pulse magnetisation study was performed. Here, the bulk was partially magnetised at temperature T_1, where the aim was not to fully magnetise the superconductor, but rather to initially establish some flux in the periphery of the bulk. This will lead to less flux movement during the second pulse, and, in turn, to a lower temperature rise and a higher trapped field. After the first pulse the temperature was lowered to $T_2 < T_1$, at which a much larger pulse was applied with the intention of fully magnetising the bulk. Typically, the pulse amplitude during the first pulse was just below the flux jump threshold, whereas the second pulse was at the threshold, or slightly higher.

Several pulse and temperature combinations were tried, but none led to a markedly increased trapped field. The results are shown in Figure 5.4 (b). This is attributable to the size of the sample and the total heat generation within. Because the sample dimensions are comparatively small compared to the larger bulks in which the multi-pulse technique was shown to be effective [53, 110], it is likely that the heat generated is sufficiently well removed from the bulk so that the temperature rise is limited and not as detrimental to the trapped field as it might be in larger bulks.

Noticeably, in some cases the two-pulse technique leads to a significant decrease in the final trapped field. Compare, for example, the trapped field of 0.36 T after the two pulse sequence of 3 T at 60 K and 5.5 T at 30 K, with the trapped field of 2.75 T after a single pulse of 5.5 T at 30 K. The reason for this decrease in trapped field is that, while the two-pulse sequence likely is effective in reducing the maximum temperature rise in the bulk, the temperature does not increase sufficiently so as to trigger the flux jump effect, which, as discussed above, can be used to greatly increase the trapped field.

The maximum trapped field profile achieved at each temperature after a single pulse is shown in Figure 5.5 (a). This was measured by an array of five Hall sensors at radial positions −5 mm, −2.5 mm, 0, 2.5 mm, and 5 mm from the top surface centre, 10 s after PFM (the data points at $r = \pm 8$ mm are assumed zero as they are at the bulk edge). It was found that, due to good temperature control, the trapped field decayed less than 1 % in the first 10 min after magnetisation.

The trapped field profile does not appear to be symmetric with respect to $r = 0$. The most likely reason for this is a misalignment of the Hall sensor array with the centre of the magnetic field distribution. Since the trapped magnetic field decreases from 3 T to zero in the span of 8 mm, the average field gradient on the surface will be equal to 375 mT mm^{-1}. Hence, a misplacement of the Hall sensor by a fraction of a millimetre can lead to a significant change in the measured trapped field.

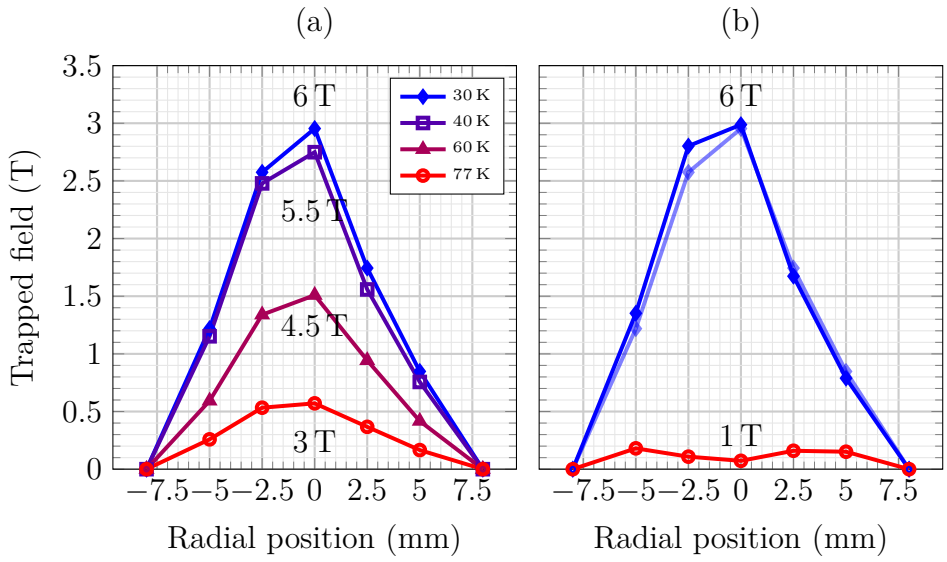

Fig. 5.5 (a) The maximum trapped field profiles following single-pulse PFM at different temperatures. The applied pulse amplitudes are indicated next to the data. (b) The trapped field profiles after the first (red) and second (blue) pulse during two-pulse PFM. In light blue is the trapped field after a single 3 T pulse at 30 K.

In Figure 5.5 (b) is the trapped field after a two-pulse, two-temperature PFM procedure. It can be seen that the improvement in trapped field is only marginal with respect to single-pulse PFM, hence single PFM was used to magnetise the bulk in the remainder of this part of the study.

Next, the field trapping capabilities of the superconductor for different applied pulse amplitudes by PFM in liquid nitrogen at 77 K were determined. Here, the temperature was kept constant, and the applied pulse amplitude was varied, and the subsequent trapped field recorded. This was done for the purposes of the study described in the following section, in which the influence of the previously established trapped field on the induced losses is discussed.

The procedure consisted of PFM with a pulse of varying amplitude up to 4 T in 0.5 T increments, followed by the measurement of trapped field 1 min after the pulse. The measurement was done using three Hall sensors at radial positions 0, 2 mm, and 4 mm from the centre of the top surface. The local trapped field vs pulse strength is shown in Figure 5.6 (a), with the trapped field profile for different pulse amplitudes illustrated in Figure 5.6 (b). Here, the trapped field at $r = 8$ mm was assumed to be zero, and the trapped fields for $r < 0$ were mirrored from the data for $r > 0$ to better illustrate the shape of the profile.

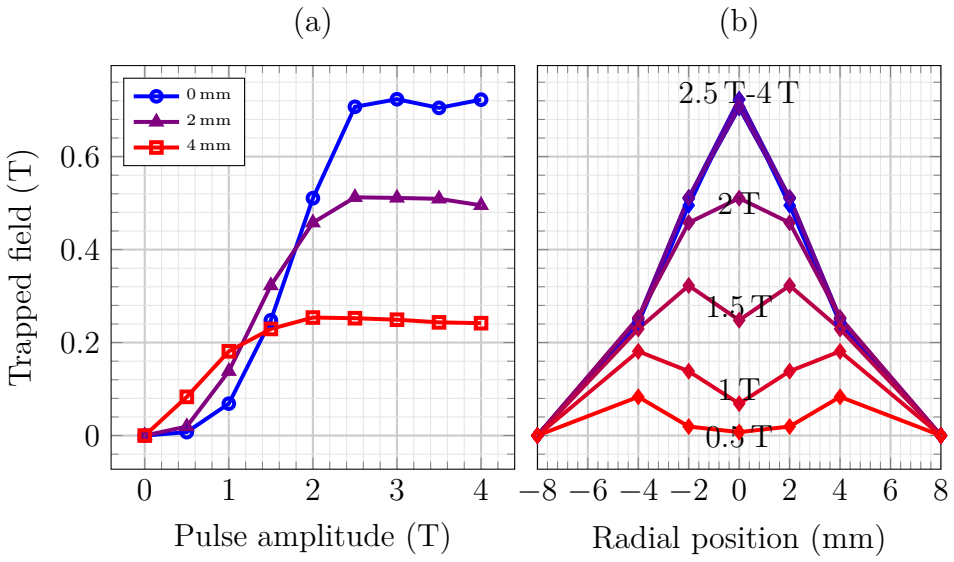

Fig. 5.6 (a) The trapped field as a function of applied field amplitude, measured at three different radial positions at 77 K in liquid nitrogen. (b) The same data as in (a), presented in the form of trapped field profiles across the bulk diameter. The data at $r < 0$ are mirrored from $r > 0$.

The positions of Hall sensors here are different to those in Figure 5.5, so there is a the slight difference in the trapped-field values. Also, the cooling, here, was supplied by the liquid nitrogen bath, as opposed to the GM cryocooler used for the measurements in Figure 5.5. This is noticeable in the lower reduction of trapped field at applied field amplitudes greater than 3 T in Figure 5.6 (a).

5.3.2 Decay of trapped field: frequency effect

After the field-trapping abilities of the bulk were established, measurements were undertaken to determine the effect of parallel AC magnetic fields on the decay of trapped field. It has been established elsewhere [108] that the losses induced in the superconductor will depend on whether the bulk has previously been magnetised. This is due, in part, to the direction of the Lorentz force which will depend on the current distribution in the bulk (see Appendix C). For this reason I performed a study, in which the bulk was magnetised to different levels (full, partial, or sub-partial magnetisation; see Figure 5.7 (a)), after which it was exposed to several thousand cycles of AC magnetic field at various amplitudes and frequencies. The time-dependence of trapped field was measured using three Hall sensors at radial positions 0, 2 mm and 4 mm from the centre of the top surface.

Firstly, the frequency dependence of decay was studied at 77 K. The amplitude of the AC magnetic field was kept constant at 45 mT and its frequency varied from 6 Hz to 48 Hz. The magnetic field was applied for 5000 cycles, after which the remaining trapped field was measured. The decay of trapped field due to flux creep in this time period was observed to be lower than 1 % for all frequencies. The normalised magnetic field after applying 5000 cycles is shown in Figure 5.7 (b)-(d).

The trapped field values after 5000 cycles are normalised to their initial values at each respective radial position. For all initial trapped fields the normalised remaining trapped field, B/B_0, decreases with increasing radial position. This can be shown to correspond to a reduction of critical current density to zero at radii up to which the external magnetic field penetrates (the formation of shielding regions).

As an example, the centre surface trapped field of a fully magnetised bulk with a constant current density, J_C, can be written as

$$B_0 = \frac{\mu_0 J_C}{2} h \log\left(\frac{r_0}{h} + \sqrt{1 + \left(\frac{r_0}{h}\right)^2}\right), \tag{5.9}$$

where r_0 and h are the bulk radius and height, respectively. From this equation the value of J_C can be estimated, given that for a fully magnetised bulk $B_0 = 0.6\,\mathrm{T}$. This gives the value $J_C = 1.35 \times 10^8\,\mathrm{A\,m^{-2}}$.

Hence, the radius, beyond which the circulating currents have reached zero after 5000 cycles of AC field, can be estimated by inserting the final centre trapped field, $B = 0.558\,\mathrm{T}$, and solving for the radius, r (here, as an example, we take the value of B from Figure 5.7 (b), blue symbol at 6 Hz). This gives the value of the new effective radius as $r_{new} = 7.32\,\mathrm{mm}$ (meaning the AC field penetration depth is $8\,\mathrm{mm} - 7.32\,\mathrm{mm} = 0.68\,\mathrm{mm}$).

Substituting the value r_{new} as the bulk radius into the Biot-Savart law, the magnetic field profile of the bulk after the application of 5000 cycles of AC magnetic field can be calculated numerically (as has been done above, shown in Figure 5.2 (c)). The ratio of the two profiles can be compared with measurements of B/B_0, which is shown in Figure 5.8. Since the measurement agrees well with calculation, I conclude that the main mechanism, driving the decay of trapped field, is current redistribution in the shielding regions at radial positions $r > r_{new}$.

In contrast, if heating and the subsequent reduction of J_C were the driving mechanism of decay, the normalised trapped field after 5000 cycles, B/B_0, would be independent of radial position. If the value of J_C is independent of field and position in the bulk (Bean model), and if the AC fields cause its decrease from J_{C1} to J_{C2}

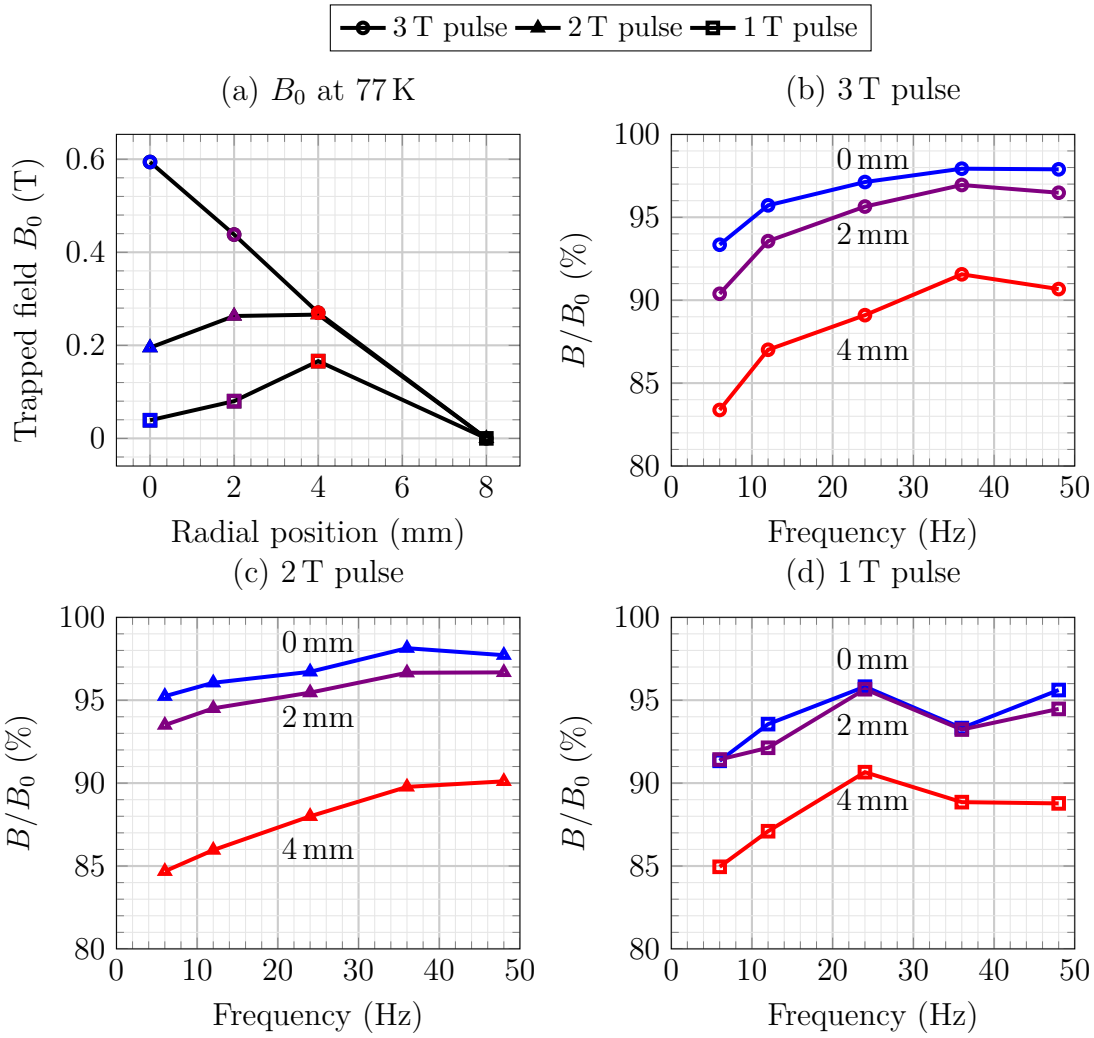

Fig. 5.7 (a) The trapped field profile as measured with the Hall sensor array after three different pulse amplitudes. The value at $r = 8\,\text{mm}$ is assumed zero. (b) The normalised trapped field after 5000 cycles of 48 mT amplitude AC field at different radial positions following a 3 T pulse. (c) After 2 T pulse. (d) After 1 T pulse.

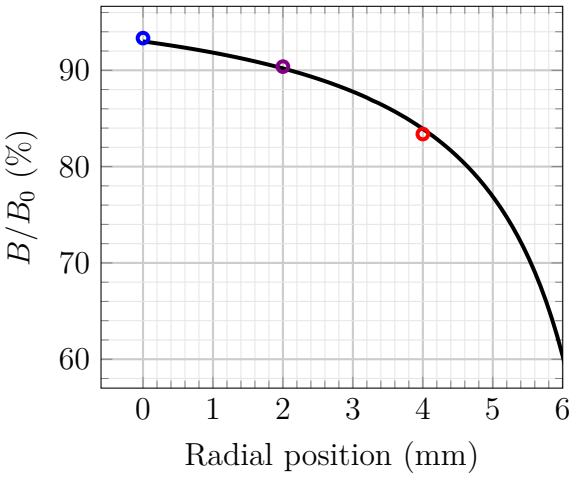

Fig. 5.8 The normalised magnetic field after the current beyond $r = r_{new} = 7.32\,\text{mm}$ has gone to zero, calculated with the Biot-Savart law (black line), compared with the measured data (symbols). The data corresponds to the 6 Hz measurements in Figure 5.7 (b).

everywhere in the bulk, then the final trapped field profile is equal to the initial profile, multiplied by the constant factor J_{C2}/J_{C1} everywhere. This behaviour would manifest itself in the measured data as a constant value of B/B_0 for all radii. This is evidently not the case in Figure 5.7 (b)-(d).

Returning to the results in Figure 5.7, the final normalised field increases with frequency or, equivalently, the decay per cycle decreases with frequency. As discussed above, the penetration depth of shielding currents is a decreasing function of frequency, which means that, in the absence of heating, the decay of trapped field per cycle will decrease with frequency as well. The data in Figure 5.7 (d) appears with more noise than in (b) and (c) because the initial trapped field value B_0 was lower and varied more, in relative terms, from pulse to pulse, than it did following 2 T and 3 T pulses. However, the overall trend of decay with frequency is still clear from Figure 5.7 (d).

As for the influence of the established circulating current on the total induced losses in the superconductor, the quantitatively similar results in Figure 5.7 (b), (c), and (d) imply that the effect is minimal for our measured AC field amplitude and frequencies. This further corroborates the explanation that current redistribution, and not AC loss $Q = EJ$, is the main driver of trapped field decay.

To further illustrate this, the temperature of the superconductor was measured during the application of AC field. The measurement was performed with a Cernox® temperature sensor, mounted atop the surface of the bulk with Apiezon N vacuum

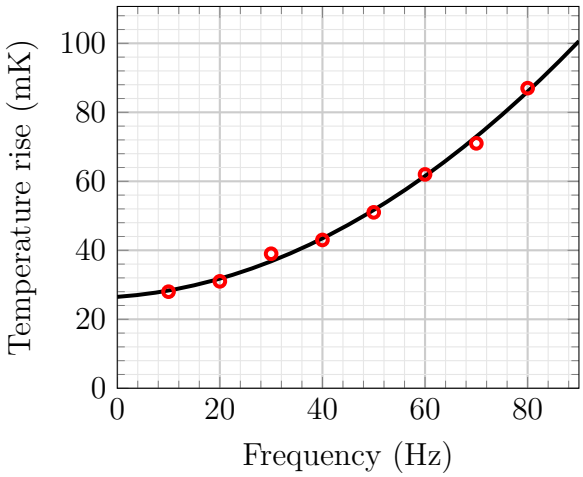

Fig. 5.9 The temperature rise measured on the surface of the bulk during the application of AC magnetic field, at various frequencies. In black is a $\propto \omega^2$ fit to the data.

grease, and insulated from the liquid nitrogen with a 1 mm layer of polystyrene. Here, the amplitude of the AC field was kept constant at 25 mT, and its frequency varied from 10 Hz to 80 Hz. The temperature of the bulk was measured 180 s after the start of AC field application, at which time the temperature stabilised for all frequencies measured. The result is shown in Figure 5.9.

The temperature rise increases with frequency due to a higher number of completed cycles of AC magnetic field. The dependence on frequency appears to be quadratic ($\Delta T \propto \omega^2$), as indicated by the black line. This is because the generated heat per cycle, $Q = EJ$, is proportional to the frequency of the AC field due to Faraday's law ($E \propto \partial B/\partial t \propto \omega B$). Additionally, the number of cycles elapsed, N, is proportional to the frequency. Hence,

$$\Delta T \propto Q_{total} = NQ \propto \omega^2. \tag{5.10}$$

The maximum temperature rise at all frequencies is below 100 mK. This leads to the conclusion that, within the range of AC field amplitudes and frequencies analysed here, the heat generation in the superconductor is sufficiently well removed such that it does not lead to a significant reduction in J_C due to heating. Instead, the trapped field decays as a consequence of the redistribution of current in the shielding regions in the periphery of the superconductor. This is well explained within the Bean critical state model.

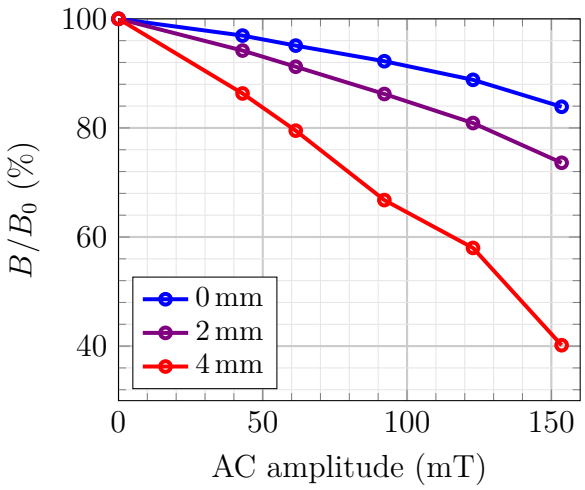

Fig. 5.10 The normalised trapped field at different radial positions after the application of 1000 cycles of AC magnetic field at a frequency of 6 Hz and varying amplitudes up to 150 mT.

5.3.3 Decay of trapped field: amplitude effect

Next, the influence of the AC magnetic field amplitude on trapped field decay was studied. For this purpose the bulk was fully magnetised with a 3 T pulse at 77 K, and subsequently exposed to 1000 cycles of AC magnetic field at a constant frequency of 6 Hz and varying amplitudes up to 150 mT. The low frequency of 6 Hz was chosen because of the limitations of the current supply - due to the inductance of the AC coil the maximum current that could be supplied was inversely proportional to the frequency at which it was supplied. Lowering the frequency meant that a higher amplitude was achievable. Additionally, 1000 cycles were chosen as this amount prooved sufficient to cause measurable decay even at the lowest applied AC field amplitudes. The trapped field profile on the surface of the bulk was measured with three Hall sensors at radial positions 0, 2 mm, and 4 mm from the centre. The normalised trapped field after 1000 cycles is shown in Figure 5.10.

The normalised decay is, again, a function of the radial position at which it was measured, indicative of decay due to current redistribution. Additionally, the normalised magnetic field decreases with increasing amplitude of the AC field. This is due to the increase of the Bean penetration and, with it, the increase of the thickness of the shielding regions in the bulk periphery. A higher-amplitude AC magnetic field, hence, leads to a greater degree of decay of trapped field.

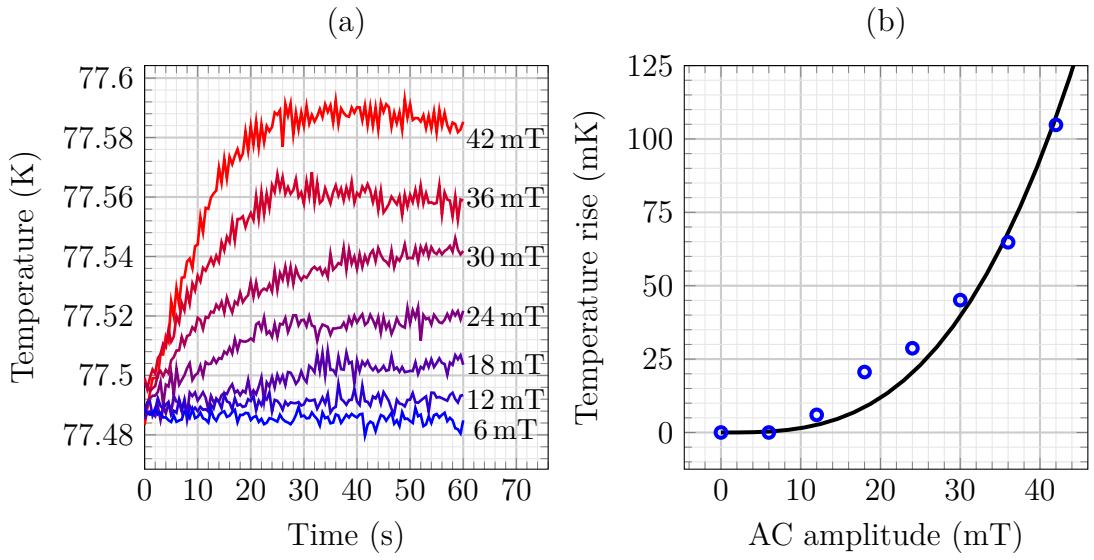

Fig. 5.11 (a) The time dependence of the bulk temperature during the application of AC magnetic field (start at $t = 0$), at different AC amplitudes. (b) The temperature increase, taken at $t = 60\,\mathrm{s}$. The black line represents a least-squares fit of equation 5.3 to the data.

The dependence of surface temperature rise on the AC field amplitude was measured with a Cernox® temperature sensor mounted on the centre of the top surface of the bulk and insulated from the liquid nitrogen bath using polystyrene. Here, the AC frequency was kept constant at 48 Hz and the amplitude was varied. The higher frequency of 48 Hz was chosen to produce more heat, leading to a larger temperature rise and a cleaner signal. The temperature initially started to increase with a rate, proportional to the amplitude of the AC magnetic field, and stabilised after 30 s (Figure 5.11 (a)). The measurement of the increased temperature was made 60 s after the start, averaged over a period of 5 s. The result is shown in Figure 5.11 (b). Here, the error for all data points does not exceed 2 mK.

Assuming the temperature increase is directly proportional to the generated heat - which will be the case if the cooling power remains independent of the temperature of the superconductor - then the temperature rise can be written as proportional to the heat in equation 5.4, which is shown in Figure 5.11 in black line. The dependence is defined as

$$\Delta T = a \cdot \left(2B_A^3 - \frac{B_A^4}{B_P} \right), \tag{5.11}$$

where B_A is the applied AC field amplitude, $B_P = B_0 = 0.6\,\mathrm{T}$ is the full penetration field for the sample (equal to the maximum trapped field), and $a = 751.34\,\mathrm{K\,T^{-3}}$ is a fitting parameter. There is some discrepancy between the fit and the data, largest around the AC amplitude 20 mT. A possible reason for this is a potential leak of the polystyrene insulation on the temperature sensor, decreasing the measured temperature rise. Additionally, equation 5.4 describes the heat generation for an infinite cylinder, and not for a single-grain of finite size, which might be contributing to the discrepancy as well.

While for the measured amplitudes of applied AC field the temperature rise does not exceed $\sim 100\,\mathrm{mK}$, the dependence 5.11 is a rapidly increasing function of B_A. For example, extrapolating to the AC field amplitude $B_A = B_P/3 = 200\,\mathrm{mT}$, the corresponding temperature rise would reach the value $\Delta T = 10\,\mathrm{K}$, and at $B_A = B_P$ the predicted temperature rise would be $\Delta T \approx 160\,\mathrm{K}$, well over the critical temperature of the material.

5.3.4 Decay of trapped field: temperature effect

Decreasing the operating temperature of the superconductor is expected to reduce the decay of trapped field, since this will lead to an increase in the value of critical current density. In turn, the penetration depth of shielding currents will decrease and so too will the volume in which heat is generated by the AC magnetic field. Simultaneously, however, the heat generated per unit volume, $Q = EJ$, will increase as well due to the higher value of J_C. Additionally, the heat capacity and thermal conductivity of the superconductor are both temperature dependent [112, 113]. Hence, the total combined effect of a change in operating temperature remains a complex problem to analyse.

Here, the influence of temperature on trapped-field decay was studied as follows. The bulk was fully magnetised using PFM, with its temperature kept at 77 K using a GM cryocooler. After PFM a waiting period of 10 min was allowed for flux creep at 77 K, or the bulk was cooled down to 20 K, 40 K, or 60 K. Subsequently, the bulk was exposed to 5000 cycles of parallel AC magnetic field of amplitude 150 mT at a frequency of 6 Hz. The trapped field was monitored using an array of five Hall sensors mounted on the top surface of the bulk at radial positions −5 mm, −2.5 mm, 0, 2.5 mm, and 5 mm from the centre. The result is shown in Figure 5.12 (a). Due to significant pick-up noise induced by the AC magnetic field the final trapped field was measured once the AC magnetic field was turned off.

When the AC magnetic field was applied at the temperature at which the bulk has previously been magnetised (77 K, red circles in Figure 5.12 (a)), the decay is

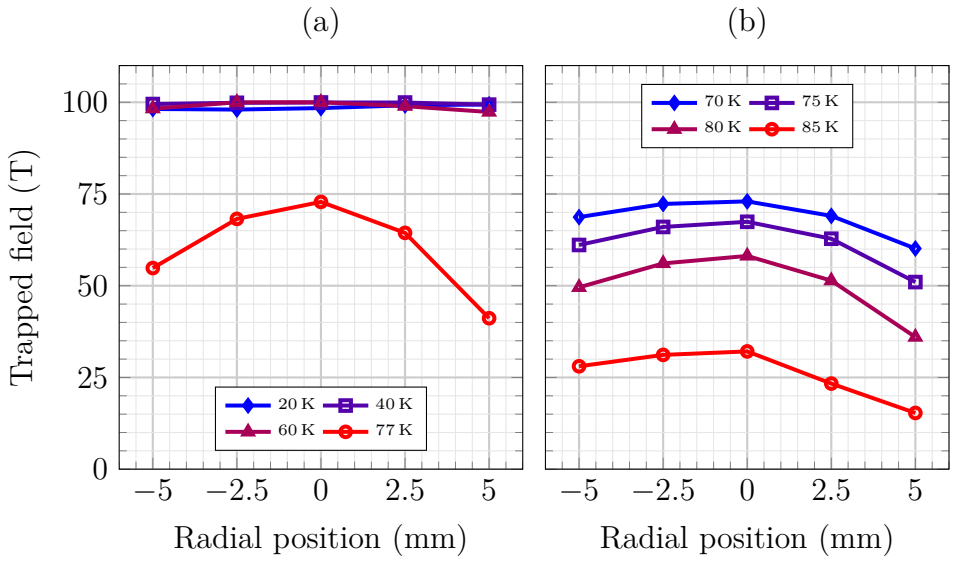

Fig. 5.12 (a) The normalised trapped field after 5000 cycles of 150 mT amplitude, 6 Hz AC magnetic field at different temperatures. Here, the bulk was previously magnetised at 77 K. (b) The normalised trapped field as in (a), but with the bulk magnetised at 40 K and warmed to each respective temperature.

significant, surpassing 50 % at the edges of the bulk. This is to be expected, since the applied field amplitude $B_A = 150\,\text{mT}$ is a quarter of the full penetration field $B_P = 600\,\text{mT}$. Correspondingly, the decay of trapped field at the centre is 25 %.

Decreasing the temperature after PFM leads to a markedly decreased decay of trapped field. At 20 K, 40 K, and 60 K the trapped field is virtually unaffected by the parallel field, with the decay remaining below 3 % at all radii. This reduction in decay is due primarily to the increase in critical current density, J_C.

Firstly, the increased value of J_C leads to a higher penetration field, $B_P = \mu_0 J_C r_0$, and a lower Bean penetration depth, $\lambda = B_A/(\mu_0 J_C)$. At a given applied field amplitude B_A the thickness of the shielding regions will decrease with increasing J_C, thus leading to a lower decay of trapped field.

Secondly, increasing the value of J_C when the bulk has previously been magnetised, renders the circulating current sub-critical, i.e. $J = J_C(T_1) < J_C(T_2)$, where $T_1 > T_2$. This means that the bulk is no longer fully magnetised to its maximum capability at the lower temperature T_2 if PFM was performed at T_1. Consequently, any current redistribution need not necessarily lead to decay of trapped field.

To determine the effect of temperature on the decay of a bulk that is fully magnetised, PFM was performed at 40 K and subsequently the temperature was increased to between

70 K and 85 K. Warming the superconductor after PFM insured that the bulk was fully magnetised at the increased temperature, since the decreasing the value of J_C would limit the circulating current in the superconductor. After warming the bulk, it was exposed to an AC magnetic field of 150 mT amplitude at 6 Hz. The normalised trapped field after 5000 cycles is shown in Figure 5.12 (b).

The decay at $T = 85$ K is significant, 70 % in the centre of the bulk, and up to 85 % at the edges. However, even for a fully magnetised bulk it is evident that reducing the temperature leads to a significant reduction in decay. Cooling the bulk by only 15 K, for example, reduces the decay in the centre by a factor of 3 and on the edges by a factor of 2. I conclude that, regardless of the degree of magnetisation of the superconductor, lowering its temperature will lead to a reduction in trapped field decay.

5.3.5 Comparison with crossed-field decay

In order to compare quantitatively the amount of decay of trapped field caused by parallel AC magnetic fields, and by crossed-fields, the above experiments were repeated in the crossed-field configuration. The goal, here, was to ascertain the difference in decay due to the different geometries, and to compare the measurement with theoretical predictions that can be made with the Biot-Savart law.

Firstly, the trapped field after all the current in the shielding regions has gone to zero can be compared for both geometries. To recall, in the parallel geometry the shielding region is a tube of thickness λ, the Bean penetration depth, from the outside surface of the bulk. In the crossed-field geometry, there are additional shielding regions of thickness $\alpha\lambda$ from the top and bottom surfaces ($\alpha = 3$ for our material). Recalling the logarithmic function

$$f(x) = \log\left(x + \sqrt{1 + x^2}\right), \tag{5.12}$$

the ratio of the remaining trapped fields in the two geometries, $B_\perp/B_\parallel$ (subscript $B_\perp$ for crossed-field, $B_\parallel$ for parallel), can be written as

$$\frac{B_\perp}{B_\parallel} = \left[(h - \alpha\lambda) f\left(\frac{r_0 - \lambda}{h - \alpha\lambda}\right) - \alpha\lambda f\left(\frac{r_0 - \lambda}{\alpha\lambda}\right)\right] \Big/ \left[h f\left(\frac{r_0 - \lambda}{h}\right)\right], \tag{5.13}$$

where r_0 and h are the bulk radius and height, respectively. The ratio is calculated by integrating the Biot-Savart law in both geometries over the volume of the superconductor beyond the penetration depth of the shielding currents. The result is shown in Figure 5.13.

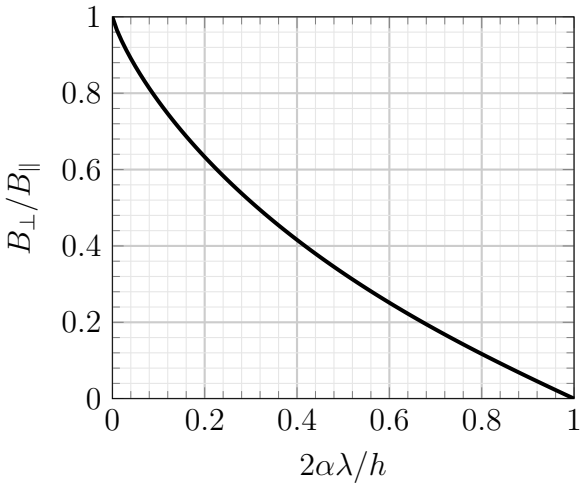

Fig. 5.13 The ratio of the trapped fields after the current in the shielding regions has gone to zero for the two geometries, as a function of the normalised penetration depth.

Here, it is assumed that $r_0 = h$, as is the case with our bulk sample. Due to the critical current anisotropy $\alpha = 3$ the decay in this case is complete ($B_\perp = 0$) when the Bean penetration depth reaches $\alpha\lambda = h/2$. At that point the penetration from the top and bottom surfaces is equal to $h/2$, hence all the circulating current goes to zero. Conversely, if $h > 2\alpha r_0$, then the shielding currents from the sides of the bulk reach the centre first, and $B_\perp = 0$ when $\lambda = r_0$.

The comparison of the frequency effect on trapped-field decay in both geometries is shown in Figure 5.14. Here, the applied field amplitude was 45 mT and the temperature was kept constant at 77 K. The AC field was applied for 5000 cycles at each frequency.

While the overall dependence of decay on frequency appears similar in both configurations, its value in the crossed-field configuration is about twice the value in the parallel configuration. Taking the average ratio $B_\perp/B_\parallel$ across all frequencies at the centre (blue triangle values, divided by respective blue circle values from Figure 5.14), the result is

$$\frac{B_\perp}{B_\parallel} = 87\,\%. \tag{5.14}$$

This can be compared with the value predicted by the Biot-Savart law (Figure 5.13). First, approximating the critical current density from the trapped field of a fully magnetised bulk gives the value (see equation 5.9, above)

$$J_C = 1.35 \times 10^8\,\mathrm{A\,m^{-2}}. \tag{5.15}$$

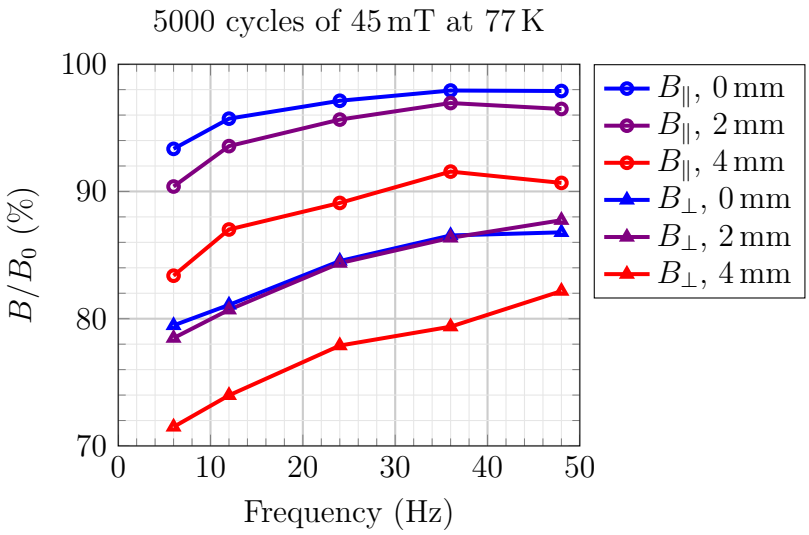

Fig. 5.14 The comparison of normalised trapped field after 5000 cycles of applied AC magnetic field in the parallel (circles) and the crossed-field (triangles) configuration, measured at different radial positions.

Hence, the penetration depth for the applied field amplitude $B_A = 45\,\text{mT}$ can be calculated as $\lambda = B_A/\mu_0 J_C = 0.27\,\text{mm}$. Substituting this value into equation 5.13, the calculated ratio reads

$$\frac{B_\perp}{B_\parallel} = 63\,\%. \tag{5.16}$$

The discrepancy between the calculated and measured values of $B_\perp/B_\parallel$ likely stems from the estimate of the value of J_C. Since the real J_C is a decreasing function of magnetic field, estimating its value from the Biot-Savart expression for a constant J_C will give an estimate lower than the value of J_C at self-field. In turn, the calculated value of the Bean penetration depth will bee too high, and the ratio $B_\perp/B_\parallel$ too low. This is what we see in our comparison, and is illustrated more clearly in the amplitude analysis, below.

The dependence of trapped-field decay on applied field amplitude in the two configurations is shown in Figure 5.15. Here, the frequency was kept constant at 6 Hz, and the amplitude varied up to 153 mT. The AC magnetic field was applied for 1000 cycles at 77 K.

At all radii, the decay increases with increasing amplitude of the applied field - this is true for both configurations. This is due to the increase of the shielding region volume with increased penetration depth. As with the frequency analysis, above, the decay in

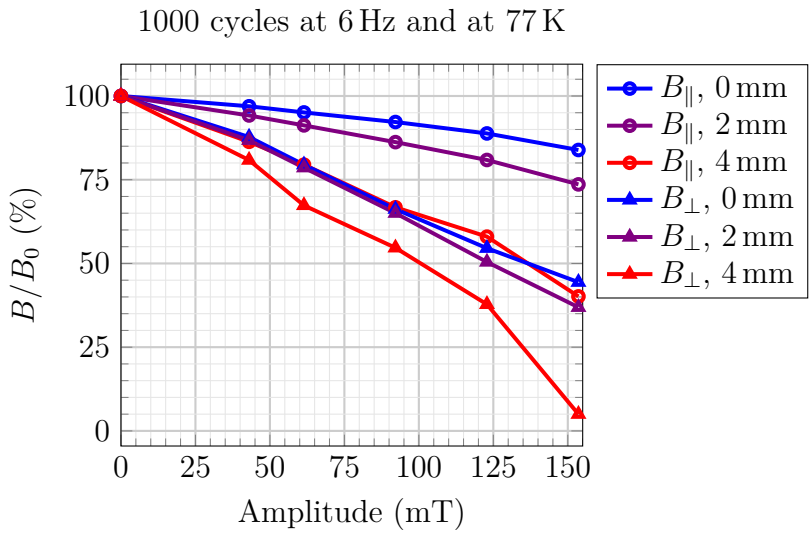

Fig. 5.15 The comparison of normalised trapped field after 1000 cycles of applied AC magnetic field in the parallel (circles) and the crossed-field (triangles) configuration, measured at different radial positions.

the crossed-field configuration is significantly higher than in the parallel configuration - reaching almost 100 % at 4 mm at the highest amplitude of applied field.

The ratio of the measured trapped field in the crossed-field and the parallel configuration after 1000 cycles of AC field can, again, be compared with the theoretical $B_\perp/B_\parallel$ ratio. To estimate the penetration depth at a given applied field amplitude, the value of $J_C = 1.35 \times 10^8\,\mathrm{A\,m^{-2}}$ - estimated with the Biot-Savart law - can be used. The ratio $B_\perp/B_\parallel$ for this case is shown in Figure 5.16 (a) in blue triangles. In a similar way to the discussion above, the values are much higher than the theoretically predicted ratio $B_\perp/B_\parallel$ - again, due to the underestimation of the value of J_C.

For a more accurate analysis the value of λ at each respective applied field amplitude can be estimated from actual measured values of the $J_C(B)$ dependence. An example of such a dependence, which is representative of high quality bulk superconductors [28], is shown in Figure 5.16 (b), red circles. Up to the applied field value of 1 T the data can be approximated with the function

$$J_C(B) = J_1 + J_2 \exp\left(-B/B_1\right), \tag{5.17}$$

where $J_1 = 2.41 \times 10^8\,\mathrm{A\,m^{-2}}$, $J_2 = 2.49 \times 10^8\,\mathrm{A\,m^{-2}}$, and $B_1 = 0.2\,\mathrm{T}$ (Figure 5.16 (b), black line). Using this dependence to approximate the penetration depth at a given

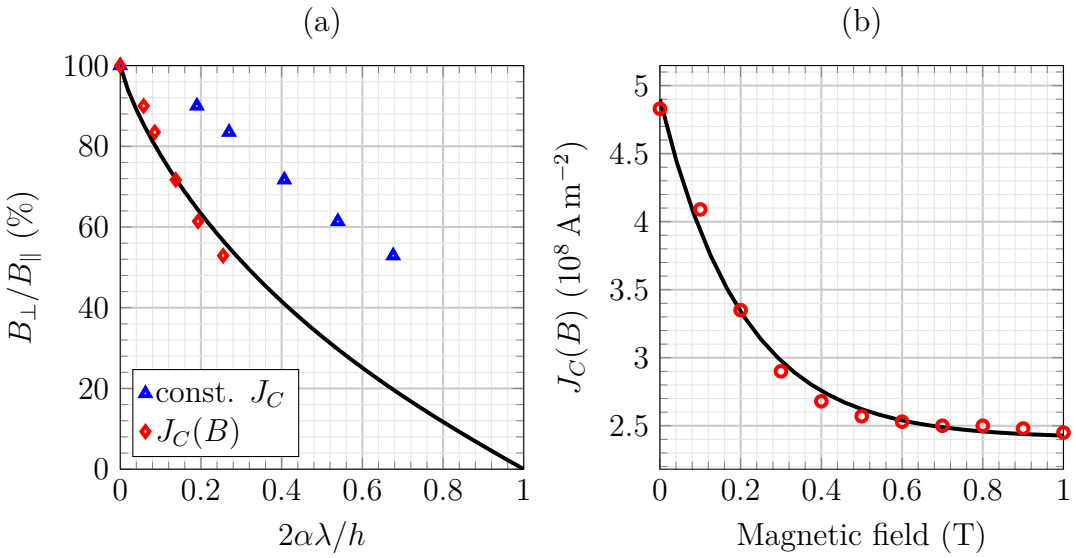

Fig. 5.16 (a) The theoretical ratio $B_\perp/B_\parallel$ (black line), compared with the values extracted from decay measurements using constant J_C (blue triangles), and a using a measured $J_C(B)$ dependence (red diamonds). (b) The measured $J_C(B)$ dependence of a representative bulk superconductor [28] (red circles) and a least-squares fit to the data (black line, equation 5.17).

applied field amplitude, B_A, as

$$\lambda = \frac{B_A}{\mu_0 J_C(B_A)}, \tag{5.18}$$

gives more accurate values of the ratio $B_\perp/B_\parallel$, shown in Figure 5.16 (a) as red diamonds. Here, the agreement between measurement and theory appears excellent. This means that the value of J_C uniquely determines the ratio $B_\perp/B_\parallel$, provided that there is little reduction of its value due to temperature rise. Conversely, from the measurements of trapped-field decay in the parallel and crossed-field configurations, the $J_C(B)$ dependence can be extracted accurately.

5.3.6 Anti-parallel pulsing

In addition to the presence of AC magnetic fields, the bulk in a rotating-machine environment will likely be exposed to singular parasitic pulses of magnetic field, provided the magnetisation technique is PFM. For example, in a rotor consisting of bulk superconductors the magnetisation procedure might consist of sequential PFM of each bulk in series, using the stator coil to generate a pulse of magnetic field. Since

previously magnetised bulks will remain in close vicinity of the pulsing coil during PFM of subsequent bulks, they likely will be exposed to single pulses of magnetic field, leading to decay. For this reason a study was performed of the effect of sequential pulses on the trapped field of a fully magnetised bulk, in the anti-parallel configuration. Here, the pulses were applied opposite the direction of trapped field because this configuration will lead to a largest decay of trapped field.

The bulk was initially fully magnetised using PFM at 77 K in a liquid nitrogen bath, after which a waiting period of 5 min duration was established to allow for flux creep and the dissipation of heat. Subsequently, the bulk was exposed to a series of pulses, of varying amplitude, at a rate of $\approx 2\,\mathrm{min}^{-1}$. The trapped field was monitored using a Hall sensor at the centre of the top surface. The result is shown in Figure 5.17.

The time dependence of normalised trapped field, B/B_0, during the sequential application of an anti-parallel pulse of amplitude $B_A = 0.75\,\mathrm{T}$ is shown in Figure 5.17 (a). The trapped field decreases by 40 % following the initial pulse, after which the decay due to each subsequent pulse decreases. Once the shielding regions are established after the first few pulses, the trapped field decay rate per pulse decreases markedly. Despite heating likely being a cause of decay in addition to current redistribution, the trapped field is not completely erased even after more than ten pulses of amplitude greater than the penetration field for the sample, $B_P = 0.6\,\mathrm{T}$.

The decay as a function of the number of applied pulses, at different pulse amplitudes, is shown in Figure 5.17 (b). The same qualitative dependence on number of pulses is present for all amplitudes: the decay of trapped field is large initially, and decreases with each subsequent applied pulse. Quantitatively, the decay increases with pulse amplitude, a feature that is well explained within the Bean model framework.

In Figure 5.17 (c) and (d) the time dependence of B/B_0 is shown during the first and tenth pulse, respectively, from Figure 5.17 (a). During the first pulse most of the current redistribution occurs, hence the value of B/B_0 decreases in a step-like fashion. Conversely, during the tenth pulse most of the current has already been redistributed and, while during the pulse the trapped field follows the shape of the applied pulse, the total decay after the pulse is much smaller and likely due to heating.

5.4 Discussion

In this chapter I investigated the effect of parallel AC magnetic fields on the trapped field in bulk superconductors. First, I presented a magnetisation study in which the trapped field after pulsed field magnetisation (PFM) was maximised. This was done by

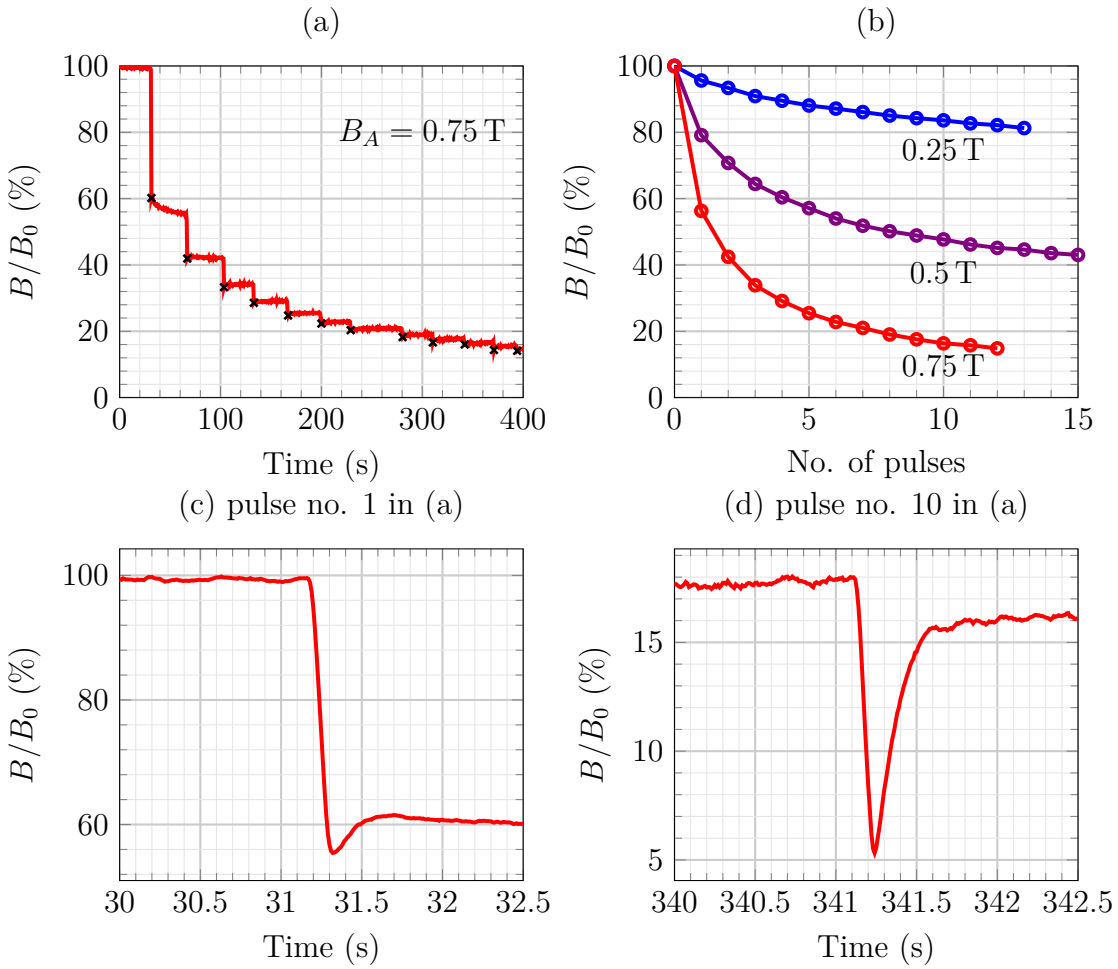

Fig. 5.17 (a) Normalised trapped field B/B_0 as a function of time for $B_A = 0.75\,\mathrm{T}$ The marks indicate when the pulses were applied. (b) B/B_0 vs number of pulses for different B_A. (c) Magnification of pulse no. 1 from (a). (d) Magnification of pulse no. 10 from (a).

a systematic scan of the pulse amplitude and pulsing temperature parameters space, both by single- and multi-pulse PFM. My conclusion, here, was that, while there is heat generated during PFM, it is sufficiently well removed from the bulk so that the subsequent temperature rise does not reduce the trapped field significantly. This I explain as being due to the comparatively small volume of the superconductor, and sufficient cooling power.

After the field-trapping capability of the bulk was established, the focus moved to the analysis of decay of trapped field due to external AC magnetic fields, applied parallel to the direction of trapped field, of varying amplitudes and frequencies. I showed that, in the absence of temperature rise, increasing the frequency of the AC magnetic field leads to a lower decay of trapped field per cycle, likely due to a lower penetration depth at a higher frequency. Conversely, increasing the amplitude of the AC magnetic field will lead to an increased decay due to a higher penetration depth and the formation of larger shielding regions in the bulk periphery, in which the current no longer contributes to the trapped field.

Throughout the application of the AC magnetic field the temperature of the superconductor was monitored. I have shown that, within the parameter space of this study, the temperature rise due to AC loss in insignificant, hence current redistribution remains the governing mechanism of decay. Additionally, I have shown that controlling the temperature of the superconductor subsequent to magnetisation can lead to effective ways of mitigating decay. In particular, lowering the temperature of the superconductor and, in turn, increasing its critical current density will lead to a lower penetration depth, lower degree of current redistribution, and a lower decay of trapped magnetic field.

Finally, the decay of trapped field in the parallel configuration was compared with its value in the crossed-field configuration at the same set amplitudes and frequencies of AC magnetic field. It was found that the overall dependence of decay on amplitude and frequency is qualitatively similar in both configurations, yet quantitatively the decay in the crossed-field configuration is significantly greater than in the parallel configuration. I have shown that, provided the critical current density $J_C(B)$ is known, the ratio of the trapped fields after the application of the AC magnetic field in both configurations, $B_\perp/B_\parallel$, can be predicted accurately with the Biot-Savart law.

Chapter 6

The Campbell penetration depth

6.1 Background

In this chapter the focus will shift from the macroscopic behaviour of type-II superconductors in the presence of time-varying magnetic fields to the underlying microscopic picture. For this purpose the limitations of the Bean model will be discussed, and its extension as proposed by Campbell will be outlined.

The Bean critical state model presupposes a maximum value of critical current, J_C, and assumes that any electromotive force exerted upon the flux vortices will induce the full J_C. The model, in essence, averages the current contribution of many individual vortices, leading to a bulk critical current density which is proportional to the vortex density gradient. In this way, as discussed in previous chapters, numerous macroscopic observables can be accounted for. However, the microscopic picture remains one of an interaction of an ensemble of flux vortices, which needs to be taken into account when outside the domain of validity of the Bean model. An example of this is a superconductor exposed to very low-amplitude AC magnetic fields.

The Bean model assumes that any electromotive force, regardless of its amplitude, will displace pinned vortices from their pinning centres and establish the critical state. This neglects the finite sizes of pinning centres and the reversible movement of flux vortices within the pinning centres themselves. In reality, a sufficiently small electromotive force (e.g. due to a low-amplitude AC magnetic field) will not unpin the vortices from their pinning sites; instead, the vortices will be made to oscillate within their respective pinning sites. Since this movement is reversible, this effect falls out of the domain of the Bean model. The Campbell model, instead, can be used to analyse

the vortices as coupled linear harmonic oscillators, which, as we shall see, leads to a more accurate prediction of the hysteretic losses in the superconductor.

In the following section the relevant body of work is discussed. Next, I derive an expression for the time dependence of magnetic flux, Φ_M, in a superconductor due to an applied AC magnetic field, provided the magnetic field profiles in the superconductor can be described within the Campbell model. Subsequently, the time dependence of induced voltage, $U_i = -\partial\Phi_M/\partial t$, is calculated, and I show that the slope of the voltage signal, as it passes through zero, is directly determined by the Campbell penetration depth. This proves convenient for the comparison of theory with experiment. Next, the experimental setup is described, and the measurement results presented. Finally, the domain of validity of the Campbell model is discussed.

6.2 Previous studies

The reversible movement of flux vortices within their pinning potentials was first introduced by Campbell [8, 36]. In an AC susceptibility measurements of a type-II superconductor, in which a sample of PbBi was exposed to AC magnetic fields and its response measured using a pick-up coil, it was found that the pick-up voltage signal at small amplitudes of applied field was directly proportional to the applied field amplitude, $U_i \propto B_A$. This is in contrast to the critical state prediction $U_i \propto B_A^2$ (see the subsequent section for derivation). The linear signal, observed by Campbell, was attributed to reversible motion of flux vortices. For instance, in the normal state, in which there is no irreversibility, the induced voltage due to a changing magnetic flux, Φ_M, would be $U_i = -\partial\Phi_M/\partial t \propto B_A$.

Subsequent to Campbell's work there have been numerous studies published on the measurement of AC susceptibility of type-II superconductors (see the review paper [114]). The basic experimental setup always consists of a superconducting sample exposed to AC magnetic fields at a constant value of DC magnetic field. Then, the superconductor response is acquired using a pick-up coil wound tightly round the sample, with the pick-up voltage measured with a lock-in amplifier. This allows for the analysis of the pick-up signal in phase and out of phase with the generated AC waveform. Hence, the reversible and irreversible behaviour of the vortices can be established.

6.2.1 Determining the pinning potential curvature from λ_C

On the experimental side, Campbell's framework has been used typically to establish the magnetic field profiles below the superconductor surface and, hence, the surface critical currents [115]. This is possible because the magnetic field profiles in the sample can be established with a high degree of accuracy, whence the critical current density can be extracted as the slope of the profile.

Another important parameter, that can be measured through the measurement of the Campbell penetration depth, is the Labusch parameter α_L [41], the effective curvature of the vortex pinning potential at its minimum. This is useful as the dependence of α_L on temperature and applied magnetic field can be used to determine the dominant pinning mechanism in a given material.

Recalling from Chapter 2, the Labusch parameter is given as

$$\alpha_L = \frac{B_0 J_C}{d}, \tag{6.1}$$

where B_0 is the applied DC magnetic field, J_C the critical current density, and d the effective size of the pinning potential (sometimes referred to as the vortex interaction distance [37]). The value of α_L, in essence, determines the slope of the pinning force at zero displacement - $B_0 J_C$ is the maximum pinning force and d is the maximum displacement up to which the pinning force is linear. Hence, the ratio of the two quantities gives the slope of the linear force.

The value of α_L can span a large range; from $10^{12}\,\mathrm{N\,m^{-4}}$ in sintered ceramic materials to $10^{20}\,\mathrm{N\,m^{-4}}$ in thin films [116]. This is not surprising as the intrinsic flux pinning may vary significantly among different materials with different microstructures and with different inclusions and imperfection responsible for providing the flux pinning centres. The units of α_L are due to it being essentially a spring constant, determined by a volumetric force density ($B_0 J_C$ is in units $\mathrm{N\,m^{-3}}$).

Since the Campbell penetration depth is defined as

$$\lambda_C^2 = \frac{B_0 d}{\mu_0 J_C} = \frac{B_0^2}{\mu_0 \alpha_L}, \tag{6.2}$$

its measurements can be used to determine the value of α_L. In studies focusing on the dependence of α_L on magnetic field [117–119], a typical result in (RE)BCO has been a peak-effect-type dependence. The value of α_L at low magnetic fields, and at fields close to the irreversibility field, B_{irr}, is observed to be low, whereas at intermediate magnetic field values α_L exhibits a broad maximum. This likely has to do with the

value of J_C being a decreasing function of B_0 - the product $B_0 J_C$ will be low when $B_0 \to 0$, and when $B_0 \to B_{irr}$ (see the results section, below).

The temperature dependence of α_L in (RE)BCO has been studied extensively as well [120–123]. Since the effective pinning potential, U, is expected to decrease exponentially with increasing temperature due to thermal fluctuations [124],

$$U(T) \propto \exp\left(-\frac{T}{T_0}\right), \tag{6.3}$$

it is expected that $\alpha_L = d^2U/dx^2$ will exhibit a similar dependence on temperature. This is, indeed, what has been observed in experiments. It is clear that, at a given value of B_0, J_C will decrease with increasing temperature and so, too, will α_L.

6.2.2 Theoretical studies

As discussed previously, the equation governing vortex motion, the Langevin equation, is [23]

$$\eta_v \mathbf{v} = \mathbf{F}_L + \mathbf{F}_P + \mathbf{F}_{th}, \tag{6.4}$$

where η_v is the vortex flow viscosity, $\mathbf{F}_L = \mathbf{J} \times \mathbf{B}$ is the Lorentz force, $\mathbf{F}_P$ is the pinning force, and $\mathbf{F}_{th}$ is the thermal actuation force. In its completely general form the equation is non-trivial to solve, but can be analysed readily from the standpoint of the Campbell model after some simplifications are made.

Assuming the superconductor is in a field-cooled state in a constant DC magnetic field, B_0, the vortex lattice will be uniform throughout and $J = 0$ everywhere. Thus, the Lorentz force can be neglected in the virgin state. Additionally, assuming a low enough temperature to allow for stationary conditions, there will be no flux creep and the thermal activation force can be neglected as well. Then, we are left with the pinning force, determined by α_L, and the viscous drag force, determined by η_v. Since the pinning force is linear and elastic in the Campbell regime, its interplay with the viscous force will lead to a kind of wave propagation, modulated by the movement of flux vortices.

This was established by Brandt [125, 126], who analysed the effect of AC magnetic fields on the vortex lattice from a theoretical standpoint. Brandt noted that the external AC magnetic field interacts with the vortices only at the surface of the superconductor, where they themselves are bent or the vortex lattice is compressed (depending on the direction of the AC field). Then, due to the inter-vortex coupling via the Lorentz force - now not zero, since the vortex lattice is no longer uniform - the vortex deformation will

propagate into the interior of the superconductor in the form of tilt or compressional waves, with the characteristic wavelength given by the Campbell penetration depth. Brandt showed that, at a low enough frequency of AC magnetic field, such that the elastic force ($\propto \alpha_L$) has not been overcome by the viscous force ($\propto \eta_v$), the complex AC penetration depth can be written as

$$\lambda_{AC}^2 = \lambda_C^2 + \lambda_L^2, \tag{6.5}$$

where λ_L is the London penetration depth. Subsequently, van der Beek [127] looked at the effect of frequency on the penetration depth, and showed that the value of λ_{AC} decreases with increasing frequency. Its value is largest in the thermally assisted flux flow (TAFF) regime, in which the frequency is sufficiently low (and the temperature sufficiently low) so that the thermal activation force, $\mathbf{F}_{th}$, is dominant. Increasing ω sees the system transition first into the Campbell regime, in which the elastic force is dominant, and subsequently into the flux flow (FF) regime, in which the viscous force is dominant. Generally, $\lambda_{TAFF} > \lambda_C > \lambda_{FF} > \lambda_L$.

6.3 The time dependence of Φ_M in the Bean and Campbell models

6.3.1 The Bean model waveform

To establish the induced voltage waveform due to the changing flux in the superconductor, first the magnetic field profile must be calculated as a function of the applied AC magnetic field, and subsequently integrated over the cross-section of the sample, giving the time dependence of magnetic flux, $\Phi_M(t)$. Then, its time derivative will give the induced voltage, $U_i = -\partial\Phi_M/\partial t$.

In an infinite slab geometry (Figure 6.1 (a)), in which the superconductor occupies the space $|x| \leq a/2$, the Bean model gives the magnetic field profile in the superconductor as

$$b(x') = \begin{cases} \mu_0 J_C x'; & x' \leq x_1, \\ B_A(t) - \mu_0 J_C (x' - x_P); & x' > x_1, \end{cases} \tag{6.6}$$

which is shown in Figure 6.1 (a) in red. Here, the coordinate system is shifted $x \to x' = x - x_P$ for the purposes of simplifying the integral of $b(x)$ (x_P is the

penetration depth of the AC magnetic field). The lower case choice for $b(x)$ is to emphasise that throughout this part of the study $b \ll B_0$, where B_0 is the applied DC magnetic field. In the above equation the applied AC magnetic field is

$$B_A(t) = B_A \cos(\omega t) \tag{6.7}$$

and its penetration depth is

$$x_P = \frac{B_A}{\mu_0 J_C}, \tag{6.8}$$

and

$$x_1 = x_P - \frac{B_A - B_A(t)}{2\mu_0 J_C}. \tag{6.9}$$

Once the magnetic field profile is known (as a function of the applied AC magnetic field), the time dependence of the total flux in the slab can be calculated as

$$\Phi_M(t) = 2l \int_0^{x_P} b(x')\, dx' = \frac{B_A^2 l}{2\mu_0 J_C} \left(1 + 2\cos(\omega t) - \cos^2(\omega t)\right), \tag{6.10}$$

where l is the dimension of the slab perpendicular to the paper in Figure 6.1 (a). The factor before the integral is due to its evaluation over one half of the slab width. This expression is valid for $0 \leq \omega t < \pi$, after which it is repeated with a negative sign every half-period. It is shown in Figure 6.1 (c) alongside the normal-state magnetic flux, which is simply $\Phi_M = alB_A \cos(\omega t)$.

Hence, the induced voltage can be calculated as $U_i = -\partial\Phi_M/\partial t$, giving

$$U_i^{SC}(t) = \frac{B_A^2 l\omega}{2\mu_0 J_C} \left(2\sin(\omega t) - \sin(2\omega t)\right), \tag{6.11}$$

which is shown in Figure 6.1 (d), and appears similar in shape to the measured waveform in [115]. The above expression reaches maximum, U_{SC}, at $\omega t = 2\pi/3$, which is

$$U_{SC} = \frac{3\sqrt{3}}{4} \frac{B_A^2 l\omega}{\mu_0 J_C}. \tag{6.12}$$

Additionally, the signal, S, as would be measured with a lock-in amplifier, can be calculated as

$$S = \frac{1}{2\pi} \int_0^{2\pi} U_i^{SC}(t) \cdot \sin(\omega t)\; d(\omega t) = \frac{B_A^2 l\omega}{2\mu_0 J_C}, \tag{6.13}$$

which goes as $S \propto B_A^2$, in direct contrast with Campbell's observation $S \propto B_A$.

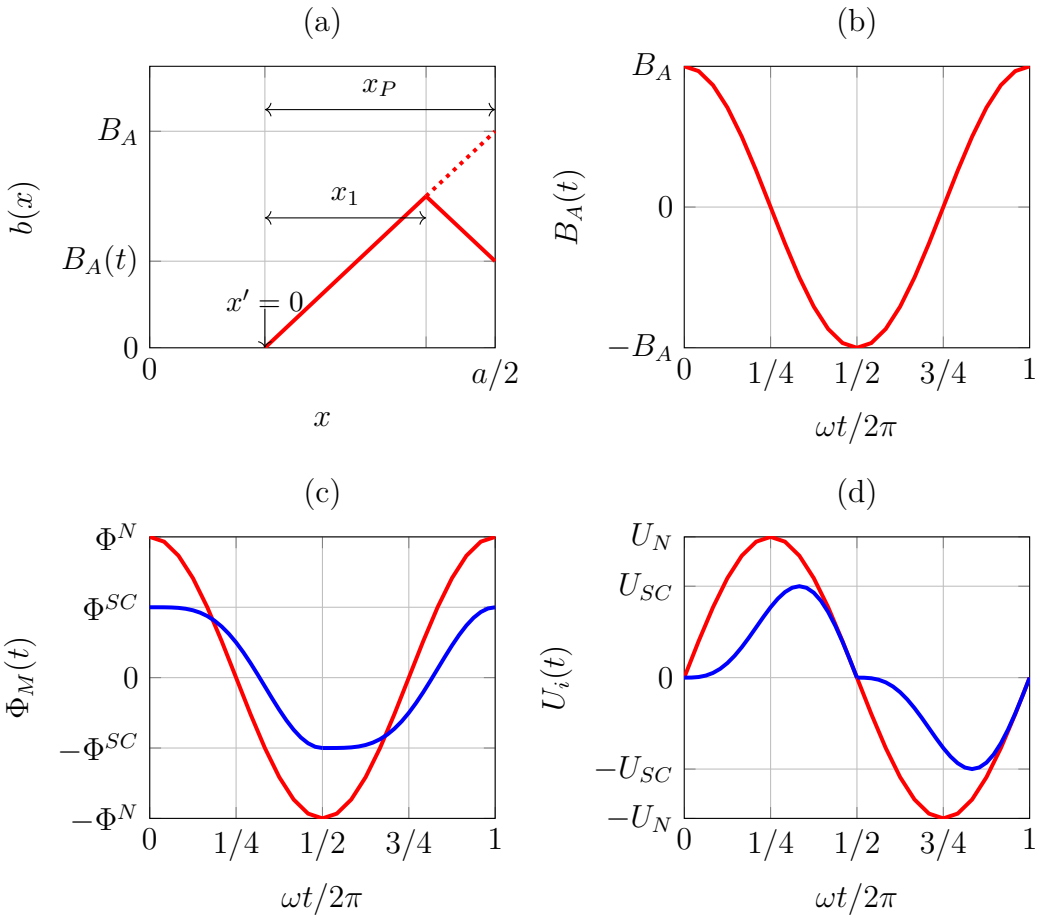

Fig. 6.1 (a) The schematic of the magnetic field profile in the $x > 0$ half of the infinite slab (the profile is symmetrical at $x < 0$). (b) One period of the applied AC field. (c) The comparison of the changing magnetic flux in the normal (N) and superconducting (SC) states. (d) The corresponding induced voltage waveform for the N and SC states.

6.3.2 The Campbell model waveform

To calculate the time dependence of induced voltage within the Campbell model framework, the dynamic equations for vortex displacement, $y(x)$, must first be calculated numerically, whence the total flux can be calculated by integration. Recalling from Chapter 2, the dynamic equations for vortex displacement can be written as

$$\frac{dy(x)}{dx} = -\frac{b(x)}{B_0} \tag{6.14}$$

$$\frac{db(x)}{dx} = -\frac{\mu_0}{B_0} F_P, \tag{6.15}$$

where $y(x)$ is the vortex displacement from its equilibrium position at position x, $b(x)$ the local change of magnetic field due to the displacement $y(x)$ (as dictated by flux conservation), B_0 the DC magnetic field with which the mixed state is established (and on top of which the AC magnetic field is superposed), and F_P is the pinning force - linear for small displacements and constant for large displacements $y(x)$.

Upon integration of the above equations the solution for $b(x)$, the magnetic field profile inside the superconductor, can be integrated over the sample cross-section, giving the total magnetic flux. If the sample is a cylinder of radius r_0, and the applied magnetic field amplitude is much smaller than the penetration field, the flux can be calculated simply as

$$\Phi_M = \int b(r) dS = 2\pi r_0 \int_0^{r_0} b(r) dr, \tag{6.16}$$

where we transformed from the Cartesian to the cylindrical coordinate system, $b(x) \rightarrow b(r)$. The above expression is true if $b(r)$ is non-zero only in a narrow region of thickness dx close to the surface, since, then, the field-penetrated area can be written as $dS = 2\pi r_0 dx$, leading to the above integral. The expression can be simplified further by calculating the antiderivative of $b(r)$ via the flux conservation equation 6.14, giving

$$\Phi_M = -2\pi r_0 B_0 \left(y(r_0) - y(0)\right) = -2\pi r_0 B_0 y(r_0), \tag{6.17}$$

where the simplification is due to the boundary condition $y(r = 0) = 0$ for a cylinder. Hence, the induced voltage can be calculated by numerical time-derivation of the flux, which result is shown schematically in Figure 6.2.

It can be seen from Figure 6.2 (b) and (c) that, while both the Bean and Campbell model waveforms are shifted by one quarter period with respect to the applied field, they differ in slope as the signal passes zero. In the Bean model the slope immediately

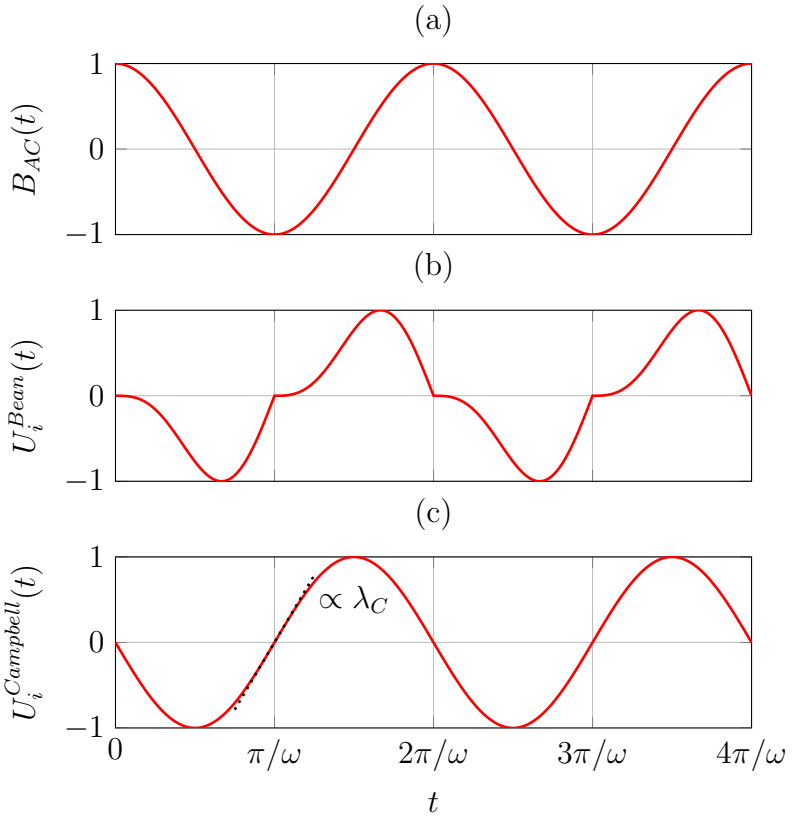

Fig. 6.2 (a) The normalised AC magnetic field waveform. The corresponding induced voltage waveforms, calculated within (b) the Bean model framework, and (c) the Campbell model framework.

after the reversal of the applied field (e.g. after $t = \pi/\omega$) is zero. This is because at that point only a small part of the trapped field profile closest to the surface will be affected ($x' > x_1$ in Figure 6.1 (a)). Immediately before $t = \pi/\omega$, however, almost all the trapped field up to the penetration depth of the AC field will be affected, with its rate of change approaching the rate of change of the applied AC field. For this reason there is a cusp in the induced voltage waveforms at zero.

Conversely, in the Campbell model framework the area affected immediately after the applied field reversal will be much larger due to the smoothing of the trapped field profile over the Campbell penetration depth, λ_C. For this reason the cusp in the voltage waveform gets smoothed as well, approaching in shape the induced voltage waveform in the normal state with no irreversibility. As wee shall see below, the slope of the voltage, as it passes zero, is proportional to the value of λ_C.

6.3.3 Analytical approximation of the induced voltage

Due to the expression 6.17 being non-analytical (because $y(r_0)$ is obtained by numerical integration), its comparison with experimental data remains cumbersome. It is desirable to derive an analytical expression, approximating the induced voltage waveform, which can be compared with measurement in a straightforward manner. An obvious choice for this is the slope of the induced voltage signal. Since in stationary conditions the signal will be periodic, it is possible to obtain a high signal-to-noise ratio simply by measuring, and subsequently averaging, the waveform over a large number of periods. For this reason, extracting information from the waveform shape, will lead, ideally, to accurate measurements of the parameters of interest.

Looking again at the pinning force hysteresis, its dependence on vortex displacement, y, can be written as

$$F_P(y) = \begin{cases} B_0 J_C \left(2\exp\left(\frac{y-y_0}{2d}\right) - \exp\left(-\frac{y_0}{d}\right) - 1\right); & y \text{ increasing}, \\ B_0 J_C \left(-2\exp\left(-\frac{y+y_0}{2d}\right) + \exp\left(-\frac{y_0}{d}\right) + 1\right); & y \text{ decreasing}, \end{cases} \tag{6.18}$$

where y_0 is the maximum vortex displacement before the field is reversed (shown in Figure 6.3). The displacement reaches its maximum value, $y = y_0$, when the applied AC magnetic field is at its peak value. At that point the induced voltage signal will pass through zero (see the waveforms at $t = \pi/\omega$ in Figure 6.2). Hence, if we approximate the pinning force hysteresis with a linear function at $y = y_0$, and substitute it subsequently into the dynamic equations for $b(x)$, an analytical expression for the voltage signal at zero can be obtained.

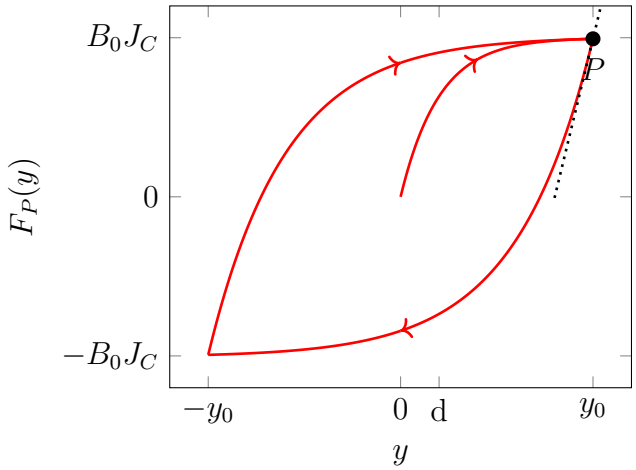

Fig. 6.3 The F_P hysteresis and its linear approximation in the point $P = (y_0, F_0)$.

At the peak of the applied magnetic field the hysteresis loop reaches its reversal point, $P = (y_0, F_0)$, where $F_0 = F_P(y_0)$. The slope at $y = y_0$ can be shown to equal $B_0 J_C/d$, hence the tangent will be

$$F_{linear} = B_0 J_C \left(\frac{y - y_0}{d}\right) + F_0, \tag{6.19}$$

which is shown in dotted line in Figure 6.3. This expression can be inserted into the dynamic equations, which will now have an analytical solution. Integration gives the expression for vortex displacement as

$$y(r) = \left(y_0 - \frac{F_0 d}{B_0 J_C}\right)\left(1 - \cosh\frac{r - r_0}{\lambda_C}\cosh^{-1}\frac{r_0}{\lambda_C}\right) - \lambda_C \frac{B_{AC}(t)}{B_0}\sinh\frac{r}{\lambda_C}\cosh^{-1}\frac{r_0}{\lambda_C}. \tag{6.20}$$

This can be inserted into equation 6.17, giving the magnetic flux, the time derivative of which is the induced voltage. Since in the above expression only the second term is a function of time, the induced voltage expression simplifies to

$$U_i = 2\pi r_0 \lambda_C \frac{\partial}{\partial t} B_A(t), \tag{6.21}$$

which is the approximation for the slope of the voltage signal as it passes zero. In comparison, the induced voltage in the normal state is given by

$$U_i^N = -\pi r_0^2 \frac{\partial}{\partial t} B_A(t). \tag{6.22}$$

Hence, the ratio of the two voltages is

$$\frac{|U_i|}{|U_i^N|} = 2\frac{\lambda_C}{r_0}. \tag{6.23}$$

This is shown in dotted line in Figure 6.2 (c). I have shown that by measuring the induced voltage signal when the superconductor is normal, and when it is in the superconducting state, their ratio for a given value of r_0 is determined by λ_C. Hence, the measurement of the slope of the induced voltage signals can be used to determine the value of λ_C.

6.3.4 Comparison of hysteretic losses in the two models

The Campbell model can also be used to predict the hysteretic losses per cycle due to the AC magnetic field. Since some of the vortex movement in the Campbell model is reversible, the hysteretic losses predicted will be lower than those, given by the Bean model. For example, the Bean model losses per vortex per cycle, Q_B, can be written simply as

$$Q_B = 4B_0 J_C y_0. \tag{6.24}$$

This can be verified by considering that during one cycle of applied AC field, the vortex will move from $-y_0$ to y_0, and the vortex pinning force will jump from $-B_0 J_C$ to $B_0 J_C$. Hence, in the force-displacement diagram the hysteresis loop will be a rectangle of sides $2y_0$ and $2B_0 J_C$, its area giving the value of Q_B, above.

Conversely, the Campbell model losses per cycle per vortex, Q_C, can be obtained by integration of the pinning force from $-y_0$ to y_0,

$$Q_C = \int_{-y_0}^{y_0} F_P(y)dy, \tag{6.25}$$

where the expression for F_P is for the increasing portion of y in equation 6.18. Evaluating the result, and dividing by the Bean losses, Q_B, gives

$$\frac{Q_C}{Q_B} = 2\frac{d}{y_0}\left(\exp\left(-\frac{y_0}{d}\right) - 1\right) + \left(\exp\left(-\frac{y_0}{d}\right) + 1\right). \tag{6.26}$$

The hysteresis loops for different values of maximum displacement, y_0, are shown in Figure 6.4. It is apparent that by increasing the value of y_0 (the half-width of the loop) the hysteresis loop in the Campbell model approaches the rectangular shape predicted by the Bean model. At $y_0 \to \infty$ the area of the reversible region will be negligible

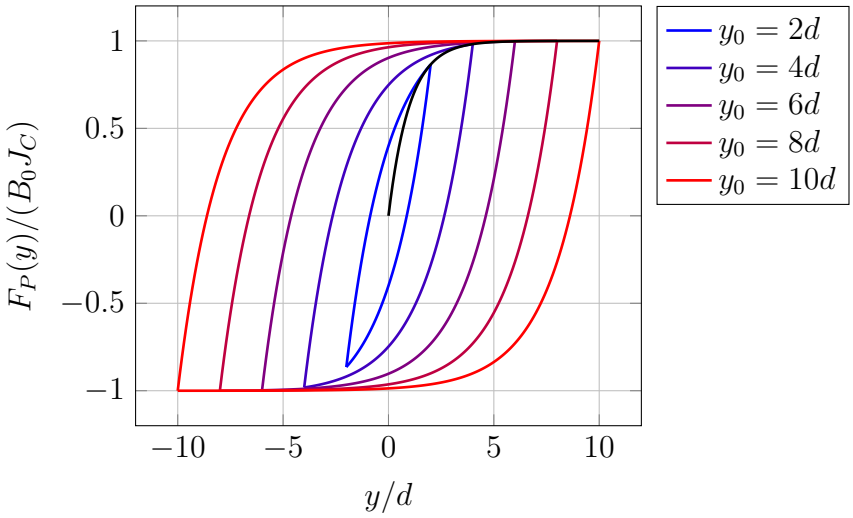

Fig. 6.4 The pinning force-displacement hysteresis for various values of maximum displacement, y_0.

in comparison with the area in which $F_P \approx B_0 J_C$, and so $Q_C = Q_B$. Conversely, at $y_0 \to 0$ it can be shown that

$$\frac{Q_C}{Q_B} \to \frac{1}{6}\frac{y_0^2}{d^2}. \tag{6.27}$$

6.4 Results

The sample used in this part of the study was a $GdBa_2Cu_3O_{7-\delta}$ bulk, grown by the top-seeded melt growth technique. Initially, the as-grown sample was of a standard cylindrical shape, 30 mm in diameter and 10 mm thick. Subsequently, a 5 mm by 5 mm by 10 mm cuboid, with the longest side parallel to the c-axis, was cut from the bulk. This was done in order to approximate the long and thin geometry for which the above theory had been derived. Since the width to height ratio of the sample is still only one half, it is likely there will be some finite-size effects present, introducing a systematic error to the measurement (discussed in Section 6.5, below). Reducing the sample cross-section further, however, likely would lead to a lower signal-to-noise ratio as the pick-up voltage is directly proportional to the sample cross-section.

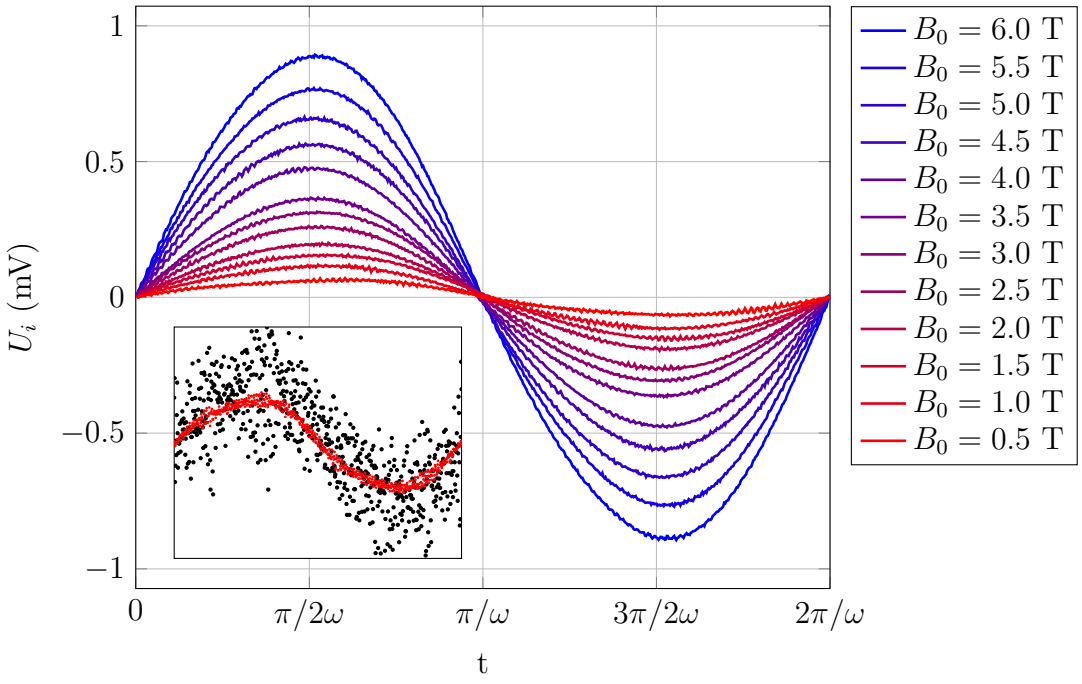

Fig. 6.5 The induced voltage waveform for different values of DC magnetic field. The AC magnetic field amplitude is 1 mT, frequency 300 Hz, and the temperature is 70 K. The inset shows the signal for $B_0 = 0.5$ T before averaging over 1000 periods.

6.4.1 Induced voltage waveforms

The induced pick-up voltage signal was measured at various values of DC magnetic field; in 0.5 T increments up to the maximum 6 T. The induced voltage waveforms are shown in Figure 6.5.

Initially the voltage waveforms were shifted in phase, indicating vortex viscosity (η_v in the Langevin equation 6.4), which was zeroed for the purposes of comparison of the waveforms at different values of B_0. The shape of the waveform at all values of B_0 is slightly asymmetrical as can be seen by the slight shift of the voltage peaks from the quarter and three quarter period marks. This indicates that, while there appears some irreversibility in the vortex movement, mostly the vortices are in the reversible regime due to the similarity of the waveform to a pure sine wave. Compare the waveform shape, for instance, with the large shift in the Bean model waveform, Figure 6.2.

From the slope of the signal at zero, and from the measured voltage signal when the superconductor is normal (not shown in Figure 6.5), the values of Campbell penetration depth can be extracted via equation 6.23. This is shown in Figure 6.6 (a).

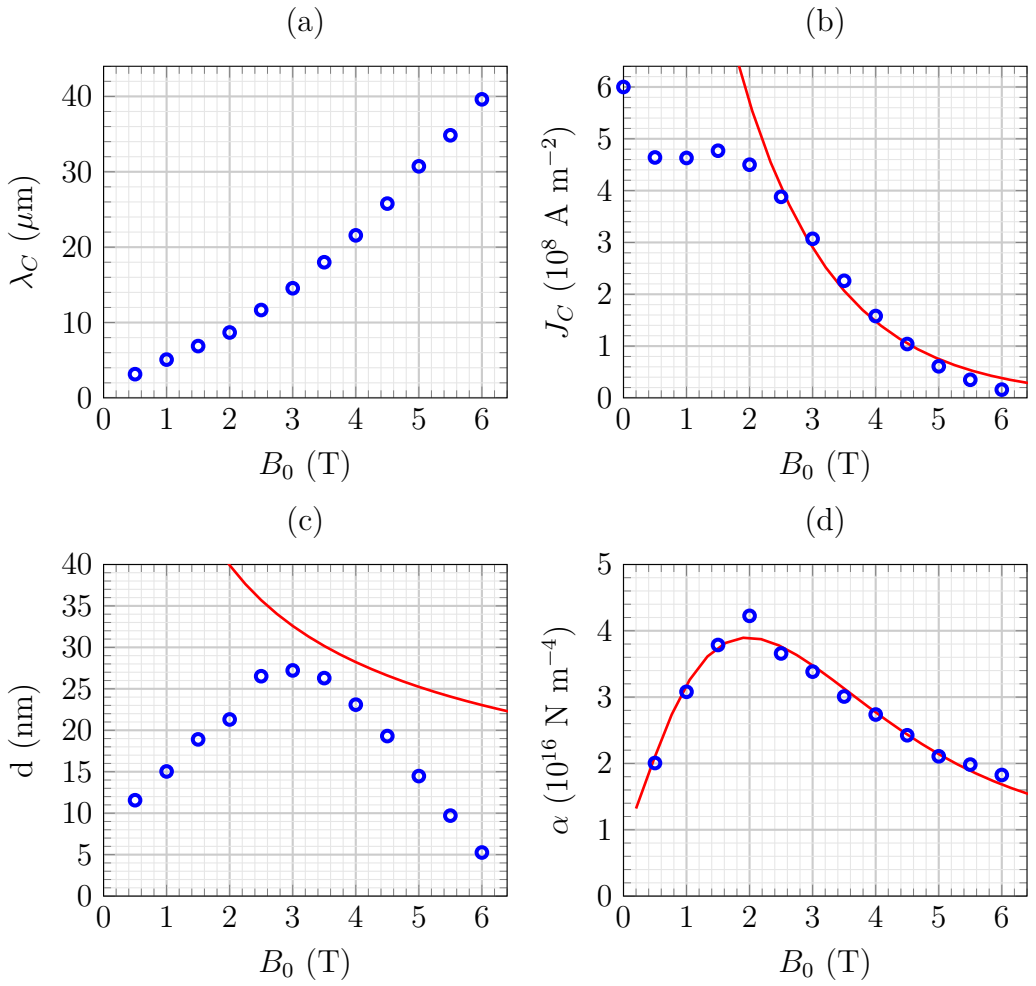

Fig. 6.6 (a) The dependence of the Campbell penetration depth on the applied DC magnetic field. (b) The $J_C(B_0)$ dependence extracted from magnetisation loops of a representative sample. The red line is a purely exponential dependence in the absence of the peak effect. (c) The dependence of d on magnetic field. The red line represents the vortex spacing in an ideal triangular lattice. (d) The curvature of the pinning potential at its minimum, the Labusch parameter. The red line is a least square fit of the function $\alpha(B_0) = c_1 + c_2\, B_0^{3/2} \exp\left(-B_0/c_3\right)$, where $c_1 = 0.95$ N m^{-4}, $c_2 = 4.76$ N m^{-4} T$^{-3/2}$, and $c_3 = 1.31$ T.

The values of λ_C at varying DC magnetic fields, as extracted from the induced voltage waveforms, increase with increasing B_0, reaching $\approx 40\,\mu\text{m}$ at $B_0 = 6\,\text{T}$. In comparison, the London penetration depth for these materials is $\approx 100\,\text{nm}$ [18]. This means that once the mixed state establishes itself in the superconductor the penetration depth of the AC magnetic field suddenly increases by two orders of magnitude, as compared to the London penetration. This is because the flux line lattice mediates the penetration by means of compressional waves, as discussed in [125]. The local vortex density - and, hence, the magnetic field - changes due to the movement of vortices in their pinning centres.

From the measured values of λ_C the effective pinning centre size, d, can be determined as

$$d = \frac{\mu_0 J_C \lambda_C^2}{B_0}, \tag{6.28}$$

provided that the dependence of J_C on magnetic field, B_0, is known. A $J_C(B_0)$ dependence, measured on a representative sample via magnetisation loop measurements [28], is shown in Figure 6.6 (b). The corresponding values of d are shown in Figure 6.6 (c).

Similarly to the data presented in the existing literature, discussed in the previous section, the dependence of d on magnetic field exhibits a peak at intermediate values of B_0 between zero and the irreversibility field, B_{irr}. At magnetic fields approaching zero the vortex pinning - and critical current density - will be high. The vortices will be pinned firmly in place, their movement impeded by the deep pinning potentials. For this reason the value of d will be low. Conversely, at magnetic fields approaching the irreversibility field the vortex pinning - and critical current density - will be low; the vortex density, however, will be high. This means that inter-vortex interactions will dominate, whereby the vortex movement is impeded by adjacent vortices. Hence, at high magnetic fields the value of d will be low as well. At intermediate fields, there will, therefore, be a trade-off between these two extremes, leading to a peak in the values of d.

The red line in Figure 6.6 (c) is the vortex spacing in an ideal triangular lattice with the vortex lattice corresponding to the magnetic field B_0. The spacing, a, can be written as a function of B_0 as

$$a(B_0) = \left(\frac{8}{3\sqrt{3}} \frac{\phi_0}{B_0} \right)^{\frac{1}{2}}, \tag{6.29}$$

where ϕ_0 is the flux quantum. There is a comparatively large discrepancy between the measured values of d and the predicted $a(B_0)$, especially in high magnetic fields where the inter-vortex interactions are expected to dominate. A possible reason for this is the sensitivity of our measurement method to an exact measurement of sample size: equation 6.23, by which the value of λ_C - and subsequently d - is determined from the induced voltage waveforms, depends on r_0, the radius of the examined sample. Since it is difficult to determine the effective cross-section of the superconducting material in the sample, the error in determining r_0 will possibly be non-negligible. This, in turn, will affect the measurement of λ_C and d. We are interested, however, in the overall dependences of λ_C and d on magnetic field - as discussed above the relevant parameter values can span orders of magnitude across different samples measured. Additionally, the parameter d represents the largest distance the vortices can move reversibly, and is defined in a very specific way via the choice of pinning force dependence on displacement (equation 6.18). A different choice of displacement dependence of F_P will likely lead to a different prediction of d. Qualitatively, however, the dependence of d on the magnetic field should remain similar, provided the pinning force captures the transition between the reversible Campbell regime and the hysteretic Bean regime.

After establishing the values of d at different magnetic fields B_0, the Labusch parameter, α_L, can be calculated as the curvature of the pinning potential (or the slope of the pinning force at $y = 0$), as

$$\alpha_L = \frac{B_0 J_C}{d}, \tag{6.30}$$

which is shown in Figure 6.6 (d). Interestingly, despite its value being inversely proportional to d, and d exhibiting a peak at intermetiate magnetic field, α_L exhibits a peak as well - at $B_0 = 2\,\mathrm{T}$. This is likely because of the peak effect in the dependence of J_C on magnetic field (Figure 6.6 (b)). For example, in the absence of the peak effect the $J_C(B_0)$ dependence likely will be exponential [128],

$$J_C(B_0) = J_{C0} \exp\left(-\frac{B_0}{B_1}\right), \tag{6.31}$$

where J_{C0} and B_0 are constants (the red line in Figure 6.6 (b) is evaluated with $J_{C0} = 22.0 \times 10^8\,\mathrm{A\,m^{-2}}$ and $B_1 = 1.48\,\mathrm{T}$). Similarly, a good measure for the vortex interaction distance, d, will be the inter-vortex spacing, $a(B_0)$ - especially at high magnetic fields at which the inter-vortex interaction dominates. Hence,

$$d \propto a(B_0) \propto B_0^{-1/2}. \tag{6.32}$$

Inserting the above expressions for J_C and d into the definition of α_L gives

$$\alpha_L = \frac{B_0 J_C}{d} \propto \frac{B_0 \exp(-B_0/B_1)}{B_0^{-1/2}} = B_0^{3/2} \exp(-B_0/B_1). \tag{6.33}$$

This result is shown in red in Figure 6.6 (d) and appears in good agreement with the measurements. This good agreement is despite the departure of d and J_C from the idealisations, shown in red in Figure 6.6 (b) and (c). The implication, here, is that the underlying cause of the peak-effect in the $J_C(B_0)$ dependence possibly is the reason for the peak in d as well.

6.4.2 Prediction of losses

Once the value of d at different magnetic fields is established, the losses predicted with the Campbell (Q_C) and Bean (Q_B) frameworks can be compared. Recalling equation 6.26, the relevant parameter, determining the ratio Q_C/Q_B, is the maximum vortex displacement from equilibrium normalised to the size of the reversible region, y_0/d. If $y_0 \ll d$ all vortex movement will remain in the reversible region and the hysteretic losses will approach zero (see the area of the hysteresis loop in Figure 6.4 for low values of y_0). Conversely, if $y_0 \gg d$ most of the vortex movement will be in the regime with a constant frictional pinning force, $F_P \approx B_0 J_C$. In evaluating the area of the hysteresis loop the linear region will be negligible and the losses will approach those predicted by the Bean model, Q_B.

The maximum vortex displacement in an AC cycle, y_0, will be largest vor vortices at the surface of the superconductor, since there the applied AC magnetic field amplitude is completely unshielded. At the surface the vortex displacement is determined by the boundary condition discussed above, which is identical for the Bean and Campbell models. For this reason, the maximum vortex displacement can be calculated within the Bean model framework and the solution will give the correct result when substituted into the Campbell model. As we shall see, a first-order approximation for the value of y_0 is simply the Bean penetration depth, $\lambda_B = B_A/(\mu_0 J_C)$, where B_A is the applied magnetic field amplitude.

For a superconductor in a constant magnetic field, B_0, with a superposed AC magnetic field, B_A, the Bean model gives the magnetic field profile in the superconductor as

$$b(r) = B_0 + \mu_0 J_C r, \tag{6.34}$$

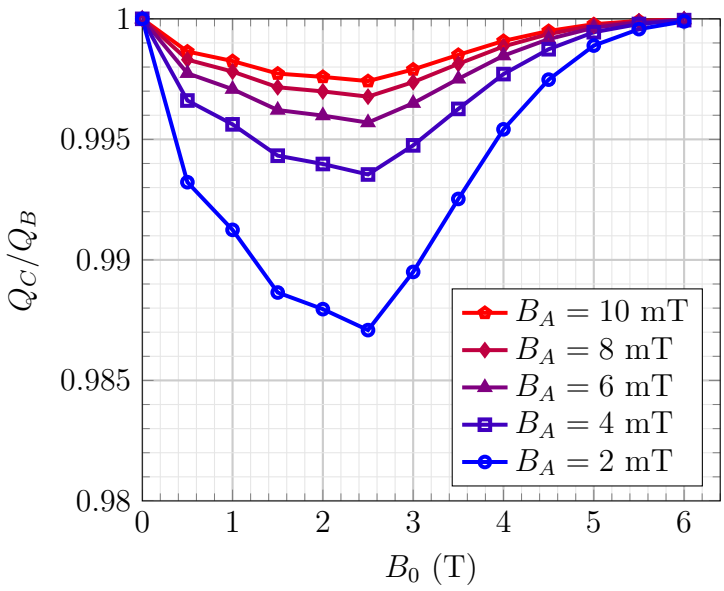

Fig. 6.7 The comparison of losses per vortex per cycle in the two models for different amplitudes of applied magnetic field.

which is valid when B_A reaches maximum. Setting $r = 0$ at the penetration depth of B_A, the above expression goes from $r = 0$ to $r = \lambda_B$. Then, the flux conservation equation 6.14 gives

$$y(r) = -\int \frac{b(r)}{B_0} dr = -\int_0^r \left(1 + \frac{\mu_0 J_C}{B_0} r'\right) dr' = -\left(r + \frac{\mu_0 J_C}{2B_0} r^2\right) + C, \tag{6.35}$$

where $C = 0$ because $y(r = 0) = 0$. Substituting $r = \lambda_B$, the result is

$$y_0 = |y(r = \lambda_B)| = \lambda_B + \frac{\mu_0 J_C}{2B_0} \lambda_B^2, \tag{6.36}$$

which approaches $y_0 = \lambda_B$ when $B_A \ll B_0$. Substituting this result into equation 6.26, and rewriting in terms of the measured parameters d and λ_C, the ratio of the Campbell and Bean losses is

$$\frac{Q_C}{Q_B} = 2\frac{B_0}{B_A}\frac{d^2}{\lambda_C^2}\left(\exp\left(-\frac{B_A}{B_0}\frac{\lambda_C^2}{d^2}\right) - 1\right) + \exp\left(-\frac{B_A}{B_0}\frac{\lambda_C^2}{d^2}\right) + 1. \tag{6.37}$$

This result is shown in Figure 6.7.

It is clear that the difference in the prediction of losses by the two models is comparatively low - this is because the maximum vortex displacement at the chosen

amplitudes of applied magnetic field is much larger than the respective values of d. For example, the largest difference between the Bean and Campbell models - the lowest value of $Q_C/Q_B = 0.987$ - appears at $B_0 = 2.5\,\mathrm{T}$ and $B_A = 2\,\mathrm{mT}$. The corresponding maximum vortex displacement is $y_0 = B_A/(\mu_0 J_C) = 4\,\mu\mathrm{m}$. In contrast, the measured value of pinning size is $d = 26\,\mathrm{nm}$, which is a factor of 150 lower. For this reason the linear region is negligible in the calculation of the hysteresis losses and the Bean model remains an adequate approximation. However, at lower applied magnetic field amplitudes, B_A, the Campbell model would have to be taken into account.

6.5 Discussion

In this chapter I discussed the validity and limitations of the Bean critical state model, and its extension by Campbell to include reversible movement of pinned vortices within their pinning centres. The allowance for a finite pinning centre size introduces new vortex dynamics into the mixed state, whereby the flux line lattice can be viewed as an ensemble of coupled linear harmonic oscillators. Their oscillations can be viewed as compressional waves, which will mediate flux penetration beyond what is predicted by the Bean model. Therefore, a new length-scale, called the Campbell penetration depth, λ_C, must be taken into account. Its value is determined by the effective size of the pinning centres and does not depend on the amplitude of the changing magnetic field. I have shown that, since λ_C determines the time dependence of the magnetic flux due to an AC magnetic field in the superconductor, its value can be measured via the observation of the induced voltage waveforms. I have also shown that the slope of the induced voltage signal, as it passes zero, will be determined by the value of λ_C, which allows for convenient data analysis. Additionally, I have extracted the size of the pinning potential, d, and its curvature, the Labusch parameter, α_L, from measurements, which appear to be in agreement with values reported in the existing literature.

Some aspects of the underlying microscopic picture, however, remain unclear. In particular, the shape of the force-displacement hysteresis loop was only assumed and not explicitly justified. It is clear that in the virgin state the slope of the force-displacement curve for small displacements is determined by the curvature of the pinning potential. This is because in the virgin state the vortices will rest in the minima of their potential wells and will - upon being displaced - experience a linear restoring force back to equilibrium.

Conversely, at the peak, and subsequent reversal, of the applied magnetic field the vortices will not start from the virgin-state equilibrium; instead, having previously established the critical state, they will move from one edge of the pinning potential to the opposite before re-establishing the critical state with the current in the opposite direction. This behaviour will lead to a different hysteresis loop shape than what is assumed here. A possible alternative picture is one of a vortex pinned on several point-like defects with the unpinned segments allowed to oscillate in the manner of vibrations on a string. Then, regardless of the magnetic history of the vortex lattice, its response is dictated by the elastic modulus of the string-like segments of the vortices.

The aspect ratio of the sample used for pick-up measurements was 5 mm/10 mm = 0.5. The theory, however, was derived for an infinitely long sample, which means that there are likely some finite-size effects not accounted for. Due to the finite size of the sample the magnetic field lines will not be completely parallel throughout the sample, but will curve towards the axis at the top and bottom of the sample. For this reason the field penetration - and consequently its contribution to the induced voltage - will be higher at the edges of the sample, leading to an overestimated value of λ_C. Ideally, however, this effect will be small since the contribution to the induced voltage is averaged over the entire height of the sample, in most of which the infinite-height approximation remains valid.

Finally, I assumed that at the applied AC magnetic field frequency of 300 Hz the effect of vortex viscosity η_v could be neglected (for comparison, in Campbell's original work the AC frequency used was 200 Hz). However, the induced voltage waveforms (Figure 6.5) were initially shifted in phase, indicating non-negligible viscosity effects. As an example, the Langevin equation taking into account the viscous force can be written as

$$\eta_v \frac{\partial y}{\partial t} = F_L - F_P. \tag{6.38}$$

It can be shown [129, 130] that the solution of the above (generalised) equation decays over a (generalised) Campbell penetration depth, given by

$$\lambda_C = \frac{B_0}{\sqrt{\alpha_L - \mathrm{i}\omega\eta_v}}, \tag{6.39}$$

where i is the imaginary unit. Hence, the phase shift will be on the order of

$$\Delta\phi \propto \arctan\frac{\omega\eta_v}{\alpha_L}, \tag{6.40}$$

from which the value of η_v can be extracted.

The results presented in this chapter, while not immediately related to the main theme of this work, are important as they shed light on the underlying physics of flux pinning in (RE)BCO bulk superconductors. In turn, this can aid future manufacturing processes in which the ultimate goal will be to increase the current carrying capabilities of the material. The Campbell framework provides a convenient way of investigating the effective size of the pinning centres in the material, d, which is a parameter on a nanometre scale. This method, combined with the analysis of the microstructure of the material, will lead to a better understanding of the interaction between the flux vortices and the material.

Chapter 7

Conclusions and further work

7.1 Conclusions

The behaviour of type-II superconductors in AC magnetic fields remains a complex problem to study as it will depend on multiple parameters. These include the superconductor's temperature, the cooling power of the cryogenic system, the AC magnetic field amplitude and frequency, as well as the geometry of the configuration studied. To this end I have presented a comprehensive experimental study of the parameter space of interest and presented novel analytical solutions giving insight to the underlying physics.

I studied the crossed-field configuration, whereby the trapped magnetic field in a bulk superconductor is made to decay due to an external AC magnetic field, applied perpendicular to the direction of the trapped field. I derived an analytical model based on the observation that the rate of decay of trapped magnetic field appears large immediately after the start of AC field application, and is reduced subsequently at larger times. This I explained as being due to the formation of shielding regions, as predicted approximately by the Bean critical state model, in which shielding regions the trapped magnetic field will decay exponentially in time. This exponential decay combined with the intrinsic logarithmic decay caused by flux creep is what leads to the two rates of decay, observed in experiments.

I have corroborated the model with experimental data and with FEM simulations and all were found to be in excellent agreement. I have shown that, provided the value of J_C of the superconductor is known, the decay of trapped magnetic fields at large times can be predicted with accuracy. The model is general enough so that it may be applied to an arbitrary geometry and, while it is derived formally for isothermal

conditions, it can readily be extended to account for temperature rise. Hence, the model provides a useful tool with which the decay of trapped field can be predicted in a straightforward way and, being analytical, it can be evaluated much more quickly than corresponding simulations employing FEM.

I have also performed a comprehensive study of the time dependence of trapped field in the parallel configuration, in which the AC magnetic field is applied parallel to the direction of trapped magnetic field. Here, the focus was on the effect of heat generation in the superconductor on the decay of trapped field. While the way in which shielding currents are induced in the superconductor is well understood and can be simulated using FEM in a simplified 2D geometry due to symmetry, it has been observed that AC magnetic fields with amplitudes much lower than the penetration field B_P of a given sample can lead to the total decay of trapped magnetic field. This can be attributed to the temperature rise in the superconductor, caused by the losses induced by the AC magnetic field. Hence, understanding the effect of temperature and of the amplitude and frequency of the applied AC magnetic field on the decay of trapped field remains an important problem to be studied. In this study I have shown that the Bean model is sufficient to predict qualitatively the temperature rise in a bulk superconductor. I have also shown that the reduction of the operating temperature at which the superconductor is kept is an efficient way of mitigating the decay of trapped magnetic field.

Finally, I have studied the microscopic behaviour of type-II superconductors in the mixed state and have shown the limitations of the validity of the Bean critical state model at small-amplitude applied AC magnetic fields. Since the Bean model does not account for the reversible movement of flux vortices within the pinning potential, it fails to predict the superconductor response to AC magnetic fields that are sufficiently low so as not to displace the vortices from the pinning centres and establish the critical state. Instead, the Campbell model, which takes into account the reversible movement of the vortices by introducing a linear pinning force for small displacements from equilibrium, can be used to predict the behaviour of the mixed state. I have shown that, while the governing partial differential equations for flux movement in the Campbell model can be solved only numerically, in their linearised form they can be used to predict the slope of the induced voltage signal, as caused by the changing magnetic flux in the superconductor. I used this simplified method to extract the value of Campbell penetration depth from induced voltage measurements in a bulk superconductor, and, with it, the effective size of the pinning potential. The extracted values agree well with the data reported in the literature.

From the results of this work several conclusions can be drawn, which pertain to the overarching goal of improving electric motors with the use of bulk superconducting materials. The decay of trapped field in bulk superconductors, exposed to AC magnetic fields, is significant at high operating temperatures (approaching T_C), and at high AC magnetic field amplitudes and frequencies. This is true for both geometries studied; the parallel and the crossed-field configuration. However, it is likely that the parameter space, studied here, represents the worst case scenario and the measured decay represents the upper limit to what is likely to be expected in a real application.

As an example, the operating temperature of a real motor is likely to be around 20 K if liquid hydrogen is to be used as coolant [131]. As we have seen, reducing the operating temperature of the superconductor will lead to a marked decrease in the rate of decay trapped field. Additionally, the amplitude of the AC magnetic field, felt by the bulks in a real rotor, is likely to be much smaller than the amplitudes investigated in this work. This is because in an ideal rotating machine the rotor magnetic field will follow exactly the rotating magnetic field, generated by the stator. Hence, the AC fields will arise due to the non-ideal nature of the machine (e.g. higher harmonics generated by the stator coils), or due to misalignments between the rotor and stator magnetic fields (e.g. due to externally applied torque on the shaft). The combined effect of a lower operating temperature and a lower amplitude of external AC magnetic fields will lead to a marked reduction in the rate of decay of trapped magnetic field in bulks. However, it remains difficult to predict accurately the exact magnetic environment of the bulks because it will depend on the exact design of the machine in question. This problem is addressed in the next section.

7.2 Further work

The present study attempts to simulate the likely magnetic environment in a superconducting rotating machine by considering, separately, the parallel and the crossed-field configurations. In reality, however, the magnetic environment will be a combination of the two configurations, depending on the exact construction of the machine in question. For this reason a more representative study must include the machine design before measurements can be performed.

With this purpose in mind an ersatz motor was designed with which the performance of bulk superconductors can be tested in a realistic environment. The design schematic of the motor is shown in Figure 7.1.

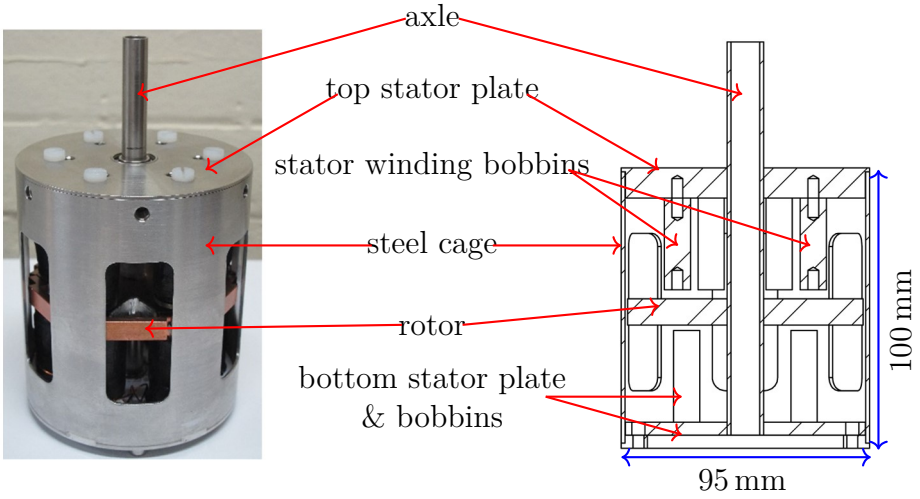

Fig. 7.1 The ersatz motor photograph and schematic.

The design is of a dual stator, axial-gap type machine with six bulk superconductors acting as trapped-field magnets in the rotor. The primary aim of the motor is to provide the magnetic environment to test the bulk performance in. In the simplest form of operation the bulks can be magnetised with FC by inserting the entire ersatz motor into the bore of a DC magnet. The magnetic field 5 mm above rotor assembly, magnetised in this way, is shown in Figure 7.2. The stator coils, wound in series in opposite sense, can be connected to a DC current supply, generating a DC magnetic field that changes direction between two adjacent stator coils (six coils making three pole pairs).

After magnetisation the rotor can be rotated by connecting the axle to an external motor. Due to the rotation the bulks will be exposed effectively to an AC magnetic field, which will be a linear combination of a parallel and crossed-field (since the DC magnetic field, generated by the stator coils, will not be perfectly aligned with the coil axis). Subsequently, the time dependence of the trapped field can be measured by means of an Hall sensor array and a slip-ring through which the Hall voltages can be acquired.

Alternatively, the bulks can be magnetised individually using FC, and subsequently inserted into the rotor assembly. This is more difficult as the whole procedure must be done at cryogenic temperatures. However, once the rotor is assembled, the stator coils can be connected to an AC current supply, making the machine effectively a single-phase electric motor. Again, the trapped magnetic field of the bulks can be monitored using Hall sensors and a slip-ring.

Another possible mode of operation is the magnetisation of bulks in-situ using the stator coils as pulsing coils for PFM. To this end, a single stator coil pair can be connected to a capacitor bank, with which a pulse of magnetic field can be generated. Subsequently, the stator coils can be connected to an AC current source, as above. In principle, this is how a practical machine would operate, and so this procedure would approximate most closely the magnetic environment bulk superconductors would be exposed to in real applications.

Regardless of the mode of operation this design can be used to predict the time-varying magnetic fields felt locally by the bulks as a consequence of their rotation in the stator magnetic field. In particular, the magnetic field components parallel and perpendicular to the direction of trapped magnetic field can be measured directly in-situ with an array of Hall sensors. The data obtained can be used subsequently to estimate the rate of decay of trapped field based on the results presented here in Chapters 4 and 6.

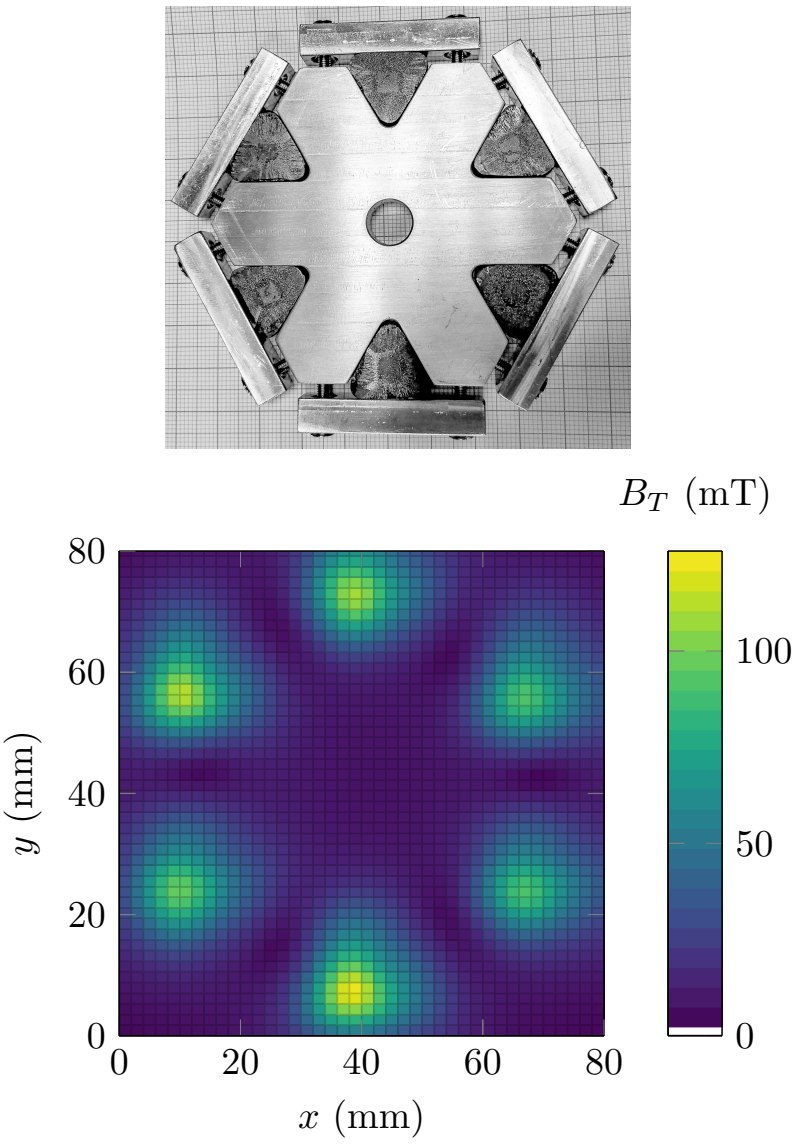

Fig. 7.2 (top) A photograph of the rotor with the six bulks. (bottom) The magnetic field amplitude, B_T, measured 5 mm above the surface of the rotor assembly.

References

[1] A. Anger. Including aviation in the European emissions trading scheme: Impacts on the industry, CO_2 emissions and macroeconomic activity in the EU. *Journal of Air Transport Management*, 16(2):100 – 105, 2010. Selected Papers from the Air Transport Research Society Conference Athens, 2008.

[2] A. Tsakalidis and C. Thiel. Electric vehicles in Europe from 2010 to 2017: is full-scale commercialisation beginning? *Publications Office of the European Union*, 2018.

[3] J. H. Durrell, M. D. Ainslie, D. Zhou, P. Vanderbemden, T. Bradshaw, S. Speller, M. Filipenko, and D. A. Cardwell. Bulk superconductors: a roadmap to applications. *Superconductor science and technology*, 31(10), 2018.

[4] A. M. Campbell and D. A. Cardwell. Bulk high temperature superconductors for magnet applications. *Cryogenics*, 37, 1997.

[5] J. H. Durrell, A. R. Dennis, J. Jaroszynski, M. D. Ainslie, K. Palmer, Y. Shi, A. M. Campbell, J. Hull, M. Strasik, E. E. Hellstrom, et al. A trapped field of 17.6 T in melt-processed, bulk Gd-Ba-Cu-O reinforced with shrink-fit steel. *Superconductor Science and Technology*, 27(8):082001, 2014.

[6] C. P. Bean. Magnetization of hard superconductors. *Physical review letters*, 8(6):250, 1962.

[7] K. Sawano, M. Morita, M. Tanaka, T. Sasaki, K. Kimura, S. Takebayashi, M. Kimura, and K. Miyamoto. High magnetic flux trapping by melt-grown YBaCuO superconductors. *Japanese Journal of applied physics*, 30(7A):L1157, 1991.

[8] A. M. Campbell. The response of pinned flux vortices to low-frequency fields. *Journal of Physics C: Solid State Physics*, 2(8):1492, 1969.

[9] L. D. Landau and E. M. Lifshitz. Chapter 4 - static magnetic field. In *Electrodynamics of Continuous Media (Second Edition)*, volume 8 of *Course of Theoretical Physics*, pages 105 – 129. Pergamon, Amsterdam, 1984.

[10] A. M. Campbell. Magnetic fields in superconductors and ferromagnetic materials. *Journal of superconductivity and novel magnetism*, 24(1-2):895–903, 2011.

[11] A. A. Abrikosov. The magnetic properties of superconducting alloys. *Journal of Physics and Chemistry of Solids*, 2(3):199–208, 1957.

[12] D. Varshney, R. K. Singh, and S. Shah. Coherence lengths and magnetic penetration depths in $YBa_2Cu_3O_7$ and $YBa_2Cu_4O_8$ superconductors. *Journal of superconductivity*, 9(6):629–635, 1996.

[13] Z. Hao, J. R. Clem, M. W. McElfresh, L. Civale, A. P. Malozemoff, and F. Holtzberg. Model for the reversible magnetization of high-κ type-II superconductors: Application to high-T_C superconductors. *Physical Review B*, 43(4):2844, 1991.

[14] W. Meissner and R. Ochsenfeld. Ein neuer effekt bei eintritt der supraleitfähigkeit. *Naturwissenschaften*, 21(44):787–788, 1933.

[15] H. Kamerlingh Onnes. The superconductivity of mercury. *Comm. Phys. Lab. Univ. Leiden. Suppl.*, 29, 1911.

[16] J. File and R. G. Mills. Observation of persistent current in a superconducting solenoid. *Physical Review Letters*, 10(3):93, 1963.

[17] F. London and H. London. The electromagnetic equations of the supraconductor. *Proceedings of the Royal Society of London. Series A-Mathematical and Physical Sciences*, 149(866):71–88, 1935.

[18] T. Pereg-Barnea, P. J. Turner, R. Harris, G. K. Mullins, J. S. Bobowski, M. Raudsepp, R. Liang, D. A. Bonn, and W. N. Hardy. Absolute values of the london penetration depth in $YBa_2Cu_3O_{6+y}$ measured by zero field ESR spectroscopy on Gd doped single crystals. *Physical review B*, 69, 2004.

[19] F. B. Silsbee. A note on electrical conduction in metals at low temperatures. *Journal of the Washington Academy of Sciences*, 6, 1916.

[20] V. L. Ginzburg and L. D. Landau. On the theory of superconductivity. *Zh. Eksp. Theor. Fiz*, 20:1064, 1950.

[21] M. Cyrot. Ginzburg-Landau theory for superconductors. *Reports on Progress in Physics*, 36(2):103, 1973.

[22] L. D. Landau. On the theory of phase transitions. *Zh. Eksp. Theor. Fiz*, 7:19–32, 1937.

[23] V. A. Shklovskij and O. V. Dobrovolskiy. AC-driven vortices and the Hall effect in a superconductor with a tilted washboard pinning potential. *Physical Review B*, 78(10):104526, 2008.

[24] J. Bardeen and M. J. Stephen. Theory of the motion of vortices in superconductors. *Physical review*, 140, 1965.

[25] Y. Shi, J. H. Durrell, A. R. Dennis, K. Y. Huang, D. K. Namburi, D. Zhou, and D. A. Cardwell. Multiple seeding for the growth of bulk GdBCO–Ag superconductors with single grain behaviour. *Superconductor Science and Technology*, 30(1):015003, 2016.

[26] Y. B. Kim, C. F. Hempstead, and A. R. Strnad. Magnetization and critical supercurrents. *Physical Review*, 129(2):528, 1963.

[27] L. T. Haag, G. Zechner, W. Lang, M. Dosmailov, M. A. Bodea, and J. D. Pedarnig. Strong vortex matching effects in YBCO films with periodic modulations of the superconducting order parameter fabricated by masked ion irradiation. *Physica C: Superconductivity and its Applications*, 503:75–81, 2014.

[28] M. D. Ainslie, H Fujishiro, H Mochizuki, K Takahashi, YH Shi, D. K. Namburi, J Zou, D Zhou, A. R. Dennis, and D. A. Cardwell. Enhanced trapped field performance of bulk high-temperature superconductors using split coil, pulsed field magnetization with an iron yoke. *Superconductor science and technology*, 29(7):074003, 2016.

[29] B. J. Senkowicz, R. J. Mungall, Y. Zhu, J. Jiang, P. M. Voyles, E. E. Hellstrom, and D. C. Larbalestier. Nanoscale grains, high irreversibility field and large critical current density as a function of high-energy ball milling time in c-doped magnesium diboride. *Superconductor Science and Technology*, 21(3):035009, 2008.

[30] P. W. Anderson. Theory of flux creep in hard superconductors. *Physical Review Letters*, 9(7):309, 1962.

[31] P. W. Anderson and Y. B. Kim. Hard superconductivity: theory of the motion of abrikosov flux lines. *Reviews of modern physics*, 36(1):39, 1964.

[32] S Arrhenius. Über die dissociationswärme und den einfluss der temperatur auf den dissociationsgrad der elektrolyte. *Zeitschrift für physikalische Chemie*, 4(1):96–116, 1889.

[33] E. Zeldov, N. M. Amer, G. Koren, A. Gupta, M. W. McElfresh, and R. J. Gambino. Flux creep characteristics in high-temperature superconductors. *Applied physics letters*, 56(7):680–682, 1990.

[34] M. D. Ainslie and H. Fujishiro. Modelling of bulk superconductor magnetization. *Superconductor Science and Technology*, 28(5):053002, 2015.

[35] M. D. Ainslie, J. Srpcic, D. Zhou, H. Fujishiro, K Takahashi, D. Cardwell, and J. H. Durrell. Toward optimisation of multi-pulse, pulsed field magnetisation of bulk high-temperature superconductors. *IEEE transactions of applied superconductivity*, 28(10), 2018.

[36] A. M. Campbell. The interaction distance between flux lines and pinning centres. *Journal of Physics C: Solid State Physics*, 4(18):3186, 1971.

[37] T. Matsushita, T. Fujiyoshi, K. Toko, and K. Yamafuji. Flux creep and irreversibility line in high-temperature oxide superconductors. *Appl. Phys. Lett*, 56, 1990.

[38] R. A. Doyle and A. M. Campbell. Direct observation of intrinsic pinning in YBCO thin films. *Physical review letters*, 71, 1993.

[39] T. Matsushita. Pinning force density in strongly pinned superconductors. *Physica C*, 243, 1995.

[40] A. M. Campbell. A new method of determining the critical state in superconductors. *Superconductor science and technology*, 20, 2007.

[41] R. Labusch. Calculation of the critical field gradient in type-2 superconductors. Technical report, Univ., Goettingen, Ger., 1969.

[42] J. G. Bednorz and K. A. Müller. Possible high-T_c superconductivity in the Ba-La-Cu-O system. *Zeitschrift für Physik B Condensed Matter*, 64(2):189–193, 1986.

[43] M.-K. Wu, J. R. Ashburn, C. J. Torng, P. H. Hor, R. L. Meng, L. Gao, Z. J. Huang, Y. Q. Wang, and C. W. Chu. Superconductivity at 93 K in a new mixed-phase Y-Ba-Cu-O compound system at ambient pressure. *Physical review letters*, 58(9):908, 1987.

[44] P. Benzi, E. Bottizzo, and N. Rizzi. Oxygen determination from cell dimensions in YBCO superconductors. *Journal of Crystal Growth*, 269(2-4):625–629, 2004.

[45] H. Liao, J. Zheng, L. Jin, H. Huang, Z. Deng, Y. Shi, D. Zhou, and D. A. Cardwell. Dynamic levitation performance of Gd–Ba–Cu–O and Y–Ba–Cu–O bulk superconductors under a varying external magnetic field. *Superconductor Science and Technology*, 31(3):035010, 2018.

[46] K. Matsunaga, M. Tomita, N. Yamachi, K. Iida, J. Yoshioka, and M. Murakami. YBCO bulk of the superconducting bearing for a 10 kWh flywheel. *Superconductor Science and Technology*, 15(5):842, 2002.

[47] K. Takahashi, H. Fujishiro, and M. D. Ainslie. A new concept of a hybrid trapped field magnet lens. *Superconductor Science and Technology*, 31(4):044005, 2018.

[48] T. Nakamura, D. Tamada, Y. Yanagi, Y. Itoh, T. Nemoto, H. Utumi, and K. Kose. Development of a superconducting bulk magnet for NMR and MRI. *Journal of Magnetic Resonance*, 259:68–75, 2015.

[49] S. Nishijima, F. Mishima, T. Terada, and S. Takeda. A study on magnetically targeted drug delivery system using superconducting magnet. *Physica C: Superconductivity and its applications*, 463:1311–1314, 2007.

[50] D. K. Namburi, Y. Shi, A. R. Dennis, J. H. Durrell, and D. A. Cardwell. A robust seeding technique for the growth of single grain (RE) BCO and (RE) BCO–Ag bulk superconductors. *Superconductor Science and Technology*, 31(4):044003, 2018.

[51] K. Konstantopoulou, Y. Shi, A. R. Dennis, J. H. Durrell, J. Y. Pastor, and D. A. Cardwell. Mechanical characterization of GdBCO/Ag and YBCO single grains fabricated by top-seeded melt growth at 77 and 300 K. *Superconductor Science and Technology*, 27(11):115011, 2014.

[52] D. A. Cardwell. Processing and properties of large grain (RE)BCO. *Materials Science and Engineering: B*, 53(1):1 – 10, 1998.

[53] H. Fujishiro, T. Tateiwa, A. Fujiwara, T. Oka, and H.i Hayash. Higher trapped field over 5T on HTSC bulk by modified pulse field magnetizing. *Physica C: Superconductivity and its Applications*, 445-448:334 – 338, 2006.

[54] D. Zhou, M. D. Ainslie, J. Srpčič, K. Huang, Y. Shi, A. R. Dennis, D. A. Cardwell, J. H. Durrel, M. Boll, and M. Filipenko. Exploiting flux jumps for pulsed field magnetisation. *Superconductor Science and Technology*, 31(10):105005, 2018.

[55] P. S. Swartz and C. P. Bean. A model for magnetic instabilities in hard superconductors: The adiabatic critical state. *Journal of Applied Physics*, 39(11):4991–4998, 1968.

[56] K.-H. Müller and C. Andrikidis. Flux jumps in melt-textured Y-Ba-Cu-O. *Phys. Rev. B*, 49:1294–1307, Jan 1994.

[57] J. Ogawa, M. Iwamoto, K. Yamagishi, O. Tsukamoto, M. Murakami, and M. Tomita. Influence of AC external magnetic field perturbation on trapped magnetic field in HTS bulk. *Physica C: Superconductivity*, 386:26 – 30, 2003.

[58] D. G. Walmsley. Force free magnetic fields in a type-II superconducting cylinder. *Journal of Physics F: Metal Physics*, 2(3):510–528, 1972.

[59] J. H. Durrell, M. J. Hogg, F. Kahlmann, Z. H. Barber, M. G. Blamire, and J. E. Evetts. Critical current of $YBa_2Cu_3O_{7-\delta}$ low-angle grain boundaries. *Phys. Rev. Lett.*, 90:247006, Jun 2003.

[60] A. M. Campbell. Flux cutting in superconductors. *Superconductor Science and Technology*, 24(9):091001, 2011.

[61] J. V. J. Congreve, Y. Shi, A. R. Dennis, J. H. Durrell, and D. A. Cardwell. Microstructure and composition of primary and recycled single grains of YBCO, GdBCO-Ag, and SmBCO-Ag bulk superconductors. *J. Am. Ceram. Soc.*, 99, 2016.

[62] K. Y. Huang, D. Zhou, J. Srpcic, Y. Shi, D. K. Namburi, A. Dennis, M. D. Ainslie, M. Boll, R. Bause, M. Filipenko, J. H. Durrell, and D. A. Cardwell. Spatial distribution of flexural strength in Y-Ba-Cu-O bulk superconductors. *IEEE transactions on applied superconductivity*, 28, 2018.

[63] J. Q. Dai, Z. X. Zhao, and A. Hu. Melt processing and superconducting properties of single-domain $GdBa_2Cu_3O_y$, $(Sm_{0.5}Gd_{0.5})YBa_2Cu_3O_y$ and $(Sm_{0.33}Eu_{0.33}Gd_{0.33})Ba_2Cu_3O_y$ superconductors fabricated in air. *Physica C: Superconductivity*, 406(1):63 – 71, 2004.

[64] N. Ogawa, M. Yoshida, I. Hirabayashi, and S. Tanaka. Preparation of YBCO bulk superconductor by platinum doped melt growth method. *Superconductor Science and Technology*, 5(1S):S89–S92, jan 1992.

[65] W. Lo, D. A. Cardwell, S. L. Dung, and R. G. Barter. Processing of bulk $YBa_2Cu_3O_{7-\delta}$ ceramics prior to peritectic solidification. *Journal of materials science*, 30, 1995.

[66] H. Fujishiro, T Naito, and M Oyama. Three-dimensional simulation of magnetic flux dynamics and temperature rise in HTSC bulk during pulsed field magnetization. *Physics Procedia*, 36:687 – 692, 2012.

[67] D. Zhou, M. D. Ainslie, J. Srpčič, K. Huang, Y. Shi, A. R. Dennis, D. A. Cardwell, J. H. Durrell, M. Boll, and M. Filipenko. Exploiting flux jumps for pulsed field magnetisation. *Superconductor Science and Technology*, 31(10), 2018.

[68] M. Qiu, H. K. Huo, Z. Xu, D. Xia, L. Z. Lin, and G. M. Zhang. Technical analysis on the application of HTS bulk in permanent magnet motor. *IEEE transactions on applied superconductivity*, 15(2), 2001.

[69] M. A. R. LeBlanc and H. G. Mattes. New magnetic phenomenon in type-II superconductors. *Journal of Applied Physics*, 41(4):1567–1572, 1970.

[70] K. Funaki and K. Yamafuji. Abnormal transverse-field effects in nonideal type-II superconductors I. A linear array of monofilamentary wires. *Japanese journal of Applied Physics*, 21(2):299–304, 1982.

[71] K. Funaki, T. Nidome, and K. Yamafuji. Abnormal transverse-field effects in nonideal type-ii superconductors ii. influence of dimension ratios in a superconducting ribbon. *Japanese journal of Applied Physics*, 21(8):1121–1126, 1982.

[72] K. Funaki, M. Noda, and K. Yamafuji. Abnormal transverse-field effects in nonideal type-II superconductors II. A theory for an ac-induced decrease in the semi-quasistatic magnetisation parallel to a DC bias field. *Japanese journal of Applied Physics*, 21(11):1580–1587, 1982.

[73] S. J. Park and Kouvel J. S. Cross-flux effect as a vortex pinning process in grain-oriented $YBa_2Cu_3O_7$. *Physical review B*, 48(18):995–997, 1982.

[74] L. M. Fischer, A. V. Kalinov, I. F. Voloshin, I. V. Baltaga, K. V. Il'enko, and V. A. Yampol'skii. Superposition of currents in hard superconductors placed into crossed ac and dc magnetic fields. *Solid state communications*, 97(10):833–836, 1996.

[75] L. M. Fischer, A. V. Kalinov, S. E. Savel'ev, I. F. Voloshin, V. A. Yampol'skii, M. A. R LeBlanc, and S. Hirscher. Collapse of the magnetic moment in a hard superconductor under the action of a transverse ac magnetic field. *Phisica C*, 278:169–179, 1997.

[76] M. Willemin, C. Rossel, J. Hofer, H. Keller, A. Erb, and E. Walker. Strong shift of the irreversibility line in high-Tc superconductors upon vortex shaking with an oscillating magnetic field. *Physical Review B*, 58(10), 1998.

[77] M. A. R. LeBlanc, S. Celebi, and M. Rezeq. Generation of quasi-reversibility in a commercial Bi:2223/Ag tape by vortex shaking with varying orthogonal magnetic fields. *Physica C*, 361, 2001.

[78] P. Vanderbemden, S. Dorbolo, N. Hari-Babu, A. Ntasis, D. A. Cardwell, and A. M. Campbell. Behaviour of bulk melt-textured YBCO single domains subjected to crossed magnetic fields. *IEEE transactions on applied superconductivity*, 13(2), 2003.

[79] P Vanderbemden, Z. Hong, T. A. Coombs, S. Denis, M. Ausloos, J. Schwartz, I. B. Rutel, N. Hari-Babu, D. A. Cardwell, and A. M. Campbell. Behaviour of bulk high-temperature superconductors of finite thickness subjected to crossed magnetic fields: experiment and model. *Physical Review B*, 75(17), 2007.

[80] P Vanderbemden, Z. Hong, T. A. Coombs, M. Ausloos, N. Hari-Babu, D. A. Cardwell, and A. M. Campbell. Remagnetisation of bulk high-temperature superconductors subjected to crossed and rotating magnetic fields. *Superconductor science and technology*, 20(9), 2007.

[81] A. Badia-Majos and C. Lopez. Critical-state analysis of orthogonal flux interactions in pinned superconductors. *Physical Review B*, 76(5), 2007.

[82] Z. Hong, P. Vanderbemden, R. Pei, Y. Jiang, A. M. Campbell, and T. A. Coombs. The numerical modelling and measurement of demagnetisation effect in bulk YBCO superconductors subjected to transverse field. *IEEE transactions on applied superconductivity*, 18(2), 2008.

[83] J.-F. Fagnard, S. Kirsch, M. Morita, H. Teshima, B. Vanderheyden, and P. Vanderbemden. Measurements on magnetised GdBCO pellets subjected to small transverce ac magnetic fields at very low frequency: evidence for a slowdown of the magnetisation decay. *Physica C*, 512:42–53, 2015.

[84] J.-F. Fagnard, M. Morita, S. Nariki, H. Teshima, H. Caps, B. Vanderheyden, and P. Vanderbemden. Magnetic moment and local magnetic induction of superconducting/ferromagnetic structures subjected to crossed fields: experiments on GdBCO and modelling. *Superconductor Science and Technology*, 29(12):125004, 2016.

[85] M. Kapolka, J. Srpčič, D. Zhou, M. D. Ainslie, E. Pardo, and A. R. Dennis. Demagnetisation of cubic Gd-Ba-Cu-O bulk superconductor by crossed fields: measurement and three-dimensional modelling. *IEEE transactions on applied superconductivity*, 28(4), 2018.

[86] M. Baghdadi, H. S. Ruiz, and T. A. Coombs. Crossed-magnetic-field experiments on stacked second generation tapes: reduction of the demagnetisation effects. *Applied physics letters*, 104, 2014.

[87] A. Campbell, M. Baghdadi, A. Patel, D. Zhou, Y. Huang, K. Y. Shi, and T. Coombs. Demagnetisation by crossed fields in superconductors. *Superconductor Science and Technology*, 30(3), 2017.

[88] M. Baghdadi, H. S. Ruiz, and T. A. Coombs. Nature of the low magnetisation decay on stacks of second generation superconducting tapes under crossed and rotating magnetic field experiments. *Scientific reports*, 8, 2018.

[89] A. Baskys, A. Patel, and B. A. Glowacki. Measurement of crossed-field demagnetisation rate of trapped field magnets at high frequencies and below 77 K. *Superconductor Science and Technology*, 31(6), 2018.

[90] J. Luzuriaga, A. Badia-Majos, G. Nieva, J. L. Giordano, C. Lopez, A. Serquis, and G. Serrano. Magnetic relaxation induced by transverse flux shaking in MgB_2 superconductors. *Superconductor Science and Technology*, 22(1), 2008.

[91] S. Celebi, F. Sirois, and C. Lacroix. Collapse of the magnetization by the application of crossed magnetic fields: observations in a commercial Bi:2223/Ag tape and comparison with numerical computations. *Superconductor Science and Technology*, 28(2), 2015.

[92] P. Vanderbemden, A. D. Bradley, R. A. Doyle, D. M. Lo, W. andAstill, D. A. Cardwell, and A. M. Campbell. Superconducting properties of natural and artificial grain boundaries in bulk melt-textured YBCO. *Physica C*, 302, 1998.

[93] D. X. Chen and R. B. Goldfarb. Kim model for magnetisation of type-II superconductors. *Journal of applied physics*, 66, 1989.

[94] R. L. Peterson. Magnetisation of anisotropic superconducting grains. *Journal of applied physics*, 67, 1990.

[95] P. Mikheenko, V. S. Dang, Y. Y. Tse, M. M. Awang Kechik, P Paturi, H. Huhtinen, Y Wang, A Sarkar, J. S. Abell, and A. Crisan. Integrated nanotechnology of pinning centres in $YBa_2Cu_3O_x$ films. *Superconductor Science and Technology*, 23, 2010.

[96] A. Xu, V. Braccini, J. Jaroszynski, Y. Xin, and D. Larbalestier. Role of weak uncorrelated pinning introduced by $BaZrO_3$ nanorods at low-temperature in $(Y,Gd)Ba_2Cu_3O_x$ thin films. *Physical review B*, 86, 2012.

[97] A. Xu, J. Jaroszynski, F. Kametani, and D. Larbalestier. Broad temperature range study of j_c and h_{irr} anisotropy in $YBa_2Cu_3O_x$ thin films containing either Y_2O_3 nanoparticles or stacking faults. *Applied Physics Letters*, 106, 2015.

[98] J. Zou, M. D. Ainslie, D. Hu, and D. A. Cardwell. Influence of time-varying external magnetic fields on trapped fields in bulk superconductors. *IEEE transactions on applied superconductivity*, 25(3), 2015.

[99] J. Zou, M. D. Ainslie, D. Hu, and D. A. Cardwell. Mitigation of demagnetisation of bulk superconductors by time-varying external magnetic fields. *IEEE transactions on applied superconductivity*, 26(4), 2016.

[100] L. Queval, V. M. R. Zermeno, and F. Grilli. Numerical models for ac loss calculation in large-scale applications of HTS coated conductors. *Superconductor Science and Technology*, 29(2), 2016.

[101] M. Tsuda, T. Susa, T. Ohyama, A. Ishiyama, S. Koyahashi, and S. Haseyama. Electromagnetic behaviour on high-temperature superconducting bulk YBCO exposed to time-varying magnetic field. *IEEE transactions on applied superconductivity*, 10(1), 2000.

[102] T. Ohyama, H. Shimizu, M. Tsuda, and A. Ishiyama. Trapped field characteristics of Y-Ba-Cu-O bulk in time-varying external magnetic field. *IEEE transactions on applied superconductivity*, 11(1), 2001.

[103] J. Ogawa, M. Iwamoto, O. Tsukamoto, M. Murakami, and M. Tomita. Interaction between trapped magnetic field and AC loss in HTS bulk. *Physica C*, 372, 2002.

[104] K. Yamagishi, J. Ogawa, O. Tsukamoto, M. Murakami, and M. Tomita. Decay of trapped magnetic field in HTS bulk caused by application of AC magnetic field. *Physica C*, 392, 2003.

[105] Y. Zushi, I. Asaba, J. Ogawa, K. Yamagishi, O. Tsukamoto, M. Murakami, and M. Tomita. Study on suppression of decay of trapped magnetic field in HTS bulk subject to AC magnetic field. *Physica C*, 412, 2004.

[106] O. Tsukamoto, K. Yamagishi, J. Ogawa, M. Murakami, and M. Tomita. Mechanism of decay of trapped magnetic field in HTS bulk caused by application of AC magnetic field. *Journal of materials processing technology*, 161, 2005.

[107] K. Yamagishi, I. Asaba, S. Sekizawa, O. Tsukamoto, J. Ogawa, K. Kikukawa, and M. Hirakawa. AC losses in HTS bulk at various temperatures. *IEEE transactions on applied superconductivity*, 15(2), 2005.

[108] J. Ogawa, S. Fukui, T. Oka, M. Yamaguchi, T. Sato, M. Takada, R. Sato, and M. Tomita. Influence of high frequency AC magnetic field on trapped magnetic field. *IEEE transactions on applied superconductivity*, 17(2), 2007.

[109] P. Laurent, J. Fagnard, N. Har Babu, D. A. Cardwell, B. Vanderheyden, and P. Vanderbemden. Self-heating of bulk high temperature superconductors of finite height subjected to a large alternating magnetic field. *Superconductor Science and Technology*, 23(12), 2010.

[110] H. Fujishiro, T. Huyama, T. Tateiwa, Y. Yanagi, and T. Oka. Importance of initial M-shaped trapped field profile in a two-stage pulse field magnetisation (MMPSC) method. *Physica C*, 463-465, 2007.

[111] D. Zhou, M. D. Ainlsie, Y. Shi, A. R. Dennis, K. Huang, J. R. Hull, D. A. Cardwell, and J. H. Durrell. A portable magnetis field of >3T generated by the flux jump assisted, pulsed field magnetisation of bulk superconductors. *Applied physics letters*, 110, 2017.

[112] M. Ikebe, H. Fujishiro, T. Naito, K. Noto, S. Kohayashi, and S. Yoshizawa. Thermal conductivity of YBCO(123) and YBCO(211) mixed crystals prepared by MMTG. *Cryogenics*, 34(1), 1994.

[113] H. Fujishiro, M. Ikebe, T. Naito, K. Noto, S. Kohayashi, and S. Yoshizawa. Anisotropic thermal diffusivity and conductivity of YBCO(123) and YBCO(211) mixed crystals. i. *Jp. J. Appl. Phys.*, 33(9A), 1994.

[114] F. Gomory. Characterization of high-temperature superconductors by AC susceptibility measurements. *Superconductor science and technology*, 10, 1997.

[115] R. W. Rollins, H. Kupfer, and W. Gey. Magnetic field profiles in type-II superconductors with pinning using a new ac technique. *Journal of applied physics*, 45, 1974.

[116] M. Ziese, P. Esquinazi, and H. F. Braun. What do we learn from vibrating high-temperature superconductors? *Superconductor science and technology*, 7, 1994.

[117] N. Baorong, H. Kitagawa, T. Wakuda, T. Shigemitsu, K. Funaki, K. Yamafuji, and T. Matsushita. Force-displacement characteristics of fluxoid lattice and pinning potential in Y-Ba-Cu-O bulk superconductor. *Jpn. J. Appl. Phys.*, 32, 1993.

[118] H. Kupfer, A. A. Zhukov, R. Kresse, R. Meier-Hirmer, W. Jahn, T. Wolf, T. Matsushita, K. Kimura, and K. Salama. Comparison of pinning parameters between low-Tc superconductors and $YBa_2Cu_3O_{7-\delta}$. *Physical review B*, 52, 1995.

[119] B. Lehndorff, H. G. Kurschner, and B. Lucke. Determination of pinning strength of $YBa_2Cu_3O_{7-\delta}$ from magnetic stiffness measurements. *Appl. Phys. Lett.*, 67, 1995.

[120] M. Golosovsky, M. Tsindlekht, and D. Davidov. High-frequency vortex dynamics in $YBa_2Cu_3O_7$. *Superconductor science and technology*, 9, 1996.

[121] J. R. Powell, A. Porch, R. G. Humphreys, F. Wellhofer, M. J. Lancaster, and C. E. Gough. Field, temperature, and frequency dependence of the surface impedance of $YBa_2Cu_3O_7$ thin films. *Physical review B*, 57, 1998.

[122] A. A. Pesetski and T. R. Lemberger. Experimental study of the inductance of pinned vortices in superconducting $YBa_2Cu_3O_{7-\delta}$ films. *Physical review B*, 62, 2000.

[123] G. Pasquini and V. Bekeris. Peak effect in YBCO crystals: statics and dynamics of the vortex lattice. *Superconductor science and technology*, 19, 2006.

[124] G. Blatter, M. V. Feigelman, V. B. Geshkenbein, A. I. Larkin, and V. M. Vinokur. Vortices in high-temperature superconductors. *Rev. Mod. Phys.*, 66, 1994.

[125] E. H. Brandt. Penetration of AC fields into type-II superconductors. *Physical review letters*, 67, 1991.

[126] E. H. Brandt. Dynamics of the flux-line lattice in high-Tc oxides. *Physica C*, 185-189, 1991.

[127] C. J. Van der Beek, V. B. Geshkenbein, and V. M. Vinokur. Linear and nonlinear AC response in the superconducting mixed state. *Physical review B*, 48, 1993.

[128] T. Kobayashi, T. Kimura, J. Shimoyama, K. Kishio, K. Kitizawa, and K. Yamafuji. Exponential field dependence of critical current density of underdoped $(La_{1-x}Sr_x)_2CuO_4$ single crystals. *Physica C*, 254, 1995.

[129] R. Willa, V. B. Geshkenbein, and G. Blatter. Campbell penetration in the critical state of type-II superconductors. *Physical review B*, 92, 2015.

[130] R. Willa, V. B. Geshkenbein, and G. Blatter. Probing the pinning landscape in type-II superconductors via campbell penetration depth. *Physical review B*, 93, 2016.

[131] K. S. Haran, S. Kalsi, T. Arndt, H. Karmaker, R. Badcock, B. Buckley, T. Haugan, M. Izumi, D. Loder, J. W. Bray, P. Masson, and E. W. Stautner. High power density superconducting rotating machines - development status and technology roadmap. *Superconductor science and technology*, 30, 2017.

Appendix A

Total flux comparison of a triangular and cylindrical bulk

In this section the growth procedure for one specific bulk will be outlined; for the rest the procedure was similar qualitatively, with the temperature profile during heat treatment varying for preforms of differing sizes. The bulk in question is a triangular bulk, shown schematically in Figure A.1 (a).

Cylindrical bulks, albeit of a standard shape, have their drawbacks when it comes to tiling a surface. In order to maximise the total flux generated by a set of bulks both the maximum trapped field of each respective bulk, and the combined surface area should be maximised. Tightly packed cylinders form a triangular grid, which covers at most 90.7 % of the surface. Conversely, triangles can be packed much more efficiently with the surface coverage approaching 100 %. Hence, in a motor application, in which the total magnetic loading (the total flux in the air gap) directly determines the output power, triangular bulks will be preferential.

To estimate the improvement in flux attained by replacing a cylindrical bulk with a triangular prism let us consider a set of long and thin bulks of circular and triangular cross-sections (Figure A.1). The bulks are assumed fully magnetised, hence the current will be equal to J_C and will flow in the azimuthal direction in the cylinder and parallel to the closest side face in the triangular bulk. The trapped field B_z parallel to the long axis of the bulk (z-direction) can then be calculated from Ampere's law, which gives the result for the cylinder

$$B_z^{\bigcirc}(r) = \mu_0 J_C \left(r_0 - r\right), \tag{A.1}$$

where r is the radial coordinate and r_0 the cylinder radius. For the triangular bulk the result is

$$B_z^{\triangle}(x) = \mu_0 J_C \left(\frac{\sqrt{3}a}{6} - x \right), \tag{A.2}$$

where a is the side length of the triangle and the x-direction is parallel to the triangle height ($\sqrt{3}a/6$ is one third of the triangle height).

The comparison between the two cases is meaningful if the centre trapped fields are the same, in which case

$$r_0 = \frac{\sqrt{3}a}{6}, \tag{A.3}$$

or when the cylinder cross-section is an inscribed circle of the triangle. Then, the total flux can be calculated as the integral of the magnetic field over the cross-section, giving

$$\Phi^{\bigcirc} = \frac{\pi}{3}\mu_0 J_C r_0^3 = \frac{\sqrt{3}\pi}{216}\mu_0 J_C a^3 \tag{A.4}$$

for the cylinder, and

$$\Phi^{\triangle} = \frac{1}{24}\mu_0 J_C a^3 \tag{A.5}$$

for the triangle. Their ratio is

$$\frac{\Phi^{\triangle}}{\Phi^{\bigcirc}} = \frac{3\sqrt{3}}{\pi} \approx 1.65. \tag{A.6}$$

This means that, given the same centre trapped field, the triangular cross-section bulk will generate a 65 % higher total flux. Since this is identical to the ratio of the respective cross-sectional areas the trapped field, averaged over the area, is the same in both cases. The difference in flux is purely due to the higher surface area of the triangle.

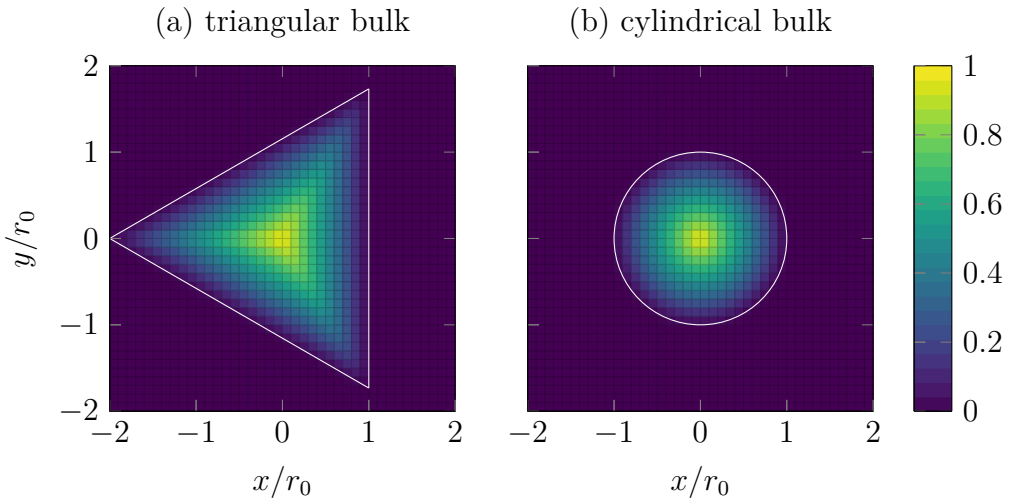

Fig. A.1 The magnetic field distribution across the (a) triangular and (b) cylindrical cross-section for a field-independent J_C and the same centre trapped field.

Appendix B

Calculation of losses in an infinite cylinder

In this appendix the hysteresis losses, Q, in an infinite superconducting cylinder due to an AC magnetic field parallel to the cylindrical axis are calculated in two different ways within the Bean model framework. This is to demonstrate the equivalence of the two expressions

$$Q = \int \mathbf{M}\, d\mathbf{B} = \mathbf{E} \cdot \mathbf{J}, \tag{B.1}$$

where $\mathbf{M}$ is the magnetisation, $\mathbf{B}$ the applied magnetic field, $\mathbf{E}$ is the induced electric field and $\mathbf{J}$ is the induced current density in the superconductor.

It is shown that the losses per unit volume per cycle evaluate to

$$Q = \begin{cases} \frac{2B_A^2}{\mu_0}\left(\frac{2\beta}{3} - \frac{\beta^2}{3}\right) & \beta < 1, \\ \frac{2B_A^2}{\mu_0}\left(\frac{2}{3\beta} - \frac{1}{3\beta^2}\right) & \beta > 1, \end{cases} \tag{B.2}$$

where B_A is the amplitude of the changing magnetic field, $\beta = B_A/B_P$, and $B_P = \mu_0 J_C r_0$ is the penetration field with r_0 the cylinder radius. Here, the derivation will be shown for the case $\beta < 1$; for the case $\beta > 1$ the procedure is similar.

The more straightforward of the two ways in this example is by calculating the losses as the area of the magnetisation loop,

$$Q = \int \mathbf{M}\, d\mathbf{B}, \tag{B.3}$$

because the magnetisation can be written as a simple function of the applied magnetic field.

The local magnetisation can be calculated using the expression $\nabla \times \mathbf{M} = \mathbf{J}$ with the boundary condition $\mathbf{M}(r = r_0) = 0$. Assuming that, in one instant, the applied magnetic field value is B, where $-B_A < B < B_A$, the local magnetisation can be written as

$$M(B,r) = \begin{cases} J_C(r - r_0) + \frac{B_A - B}{\mu_0} & r_0 - \frac{B_A}{\mu_0 J_C} < r < r_0 - \frac{B_A - B}{2\mu_0 J_C}, \\ -J_C(r - r_0) & r_0 - \frac{B_A - B}{2\mu_0 J_C} < r < r_0. \end{cases} \tag{B.4}$$

Integrating this expression over the cross-section of the cylinder, and dividing by the area πr_0^2, leads to the dependence $M(B)$. Defining the penetration field as $B_P = \mu_0 J_C r_0$, and the reduced applied field as $\beta = B_A/B_P$, leads to the result

$$M(B) = \frac{2}{r_0^2} \int_0^{r_0} M(B,r) r \, dr = \frac{1}{4\mu_0} \left(\left(4\beta - 3\beta^2\right) B + \left(\beta^3 - 2\beta^2\right) \left(B_P - \frac{B^2}{B_P} \right) - \frac{B^3}{3B_P^2} \right). \tag{B.5}$$

Subsequently, this can be integrated with respect to the magnetic field, giving the final result from equation B.1 as

$$Q = 2 \int_{-B_A}^{B_A} M(B) \, dB = 2 \frac{B_A^3 \left(2B_P - B_A\right)}{3\mu_0 B_P^2} = \frac{2B_A^2}{\mu_0} \left(\frac{2\beta}{3} - \frac{\beta^2}{3} \right), \tag{B.6}$$

where the factor 2 is because the integral goes from $B = -B_A$ to $B = B_A$, only one half-cycle, whereas Q is the loss per cycle.

An alternative way of calculating the hysteretic losses is via the equation

$$Q = \mathbf{E} \cdot \mathbf{J}, \tag{B.7}$$

where the electric field is given by Faraday's law from the changing magnetic field as

$$\nabla \times \mathbf{E} = -\frac{\partial \mathbf{B}}{\partial t}. \tag{B.8}$$

This calculation avoids the need for the explicit expression of magnetisation and may be preferable to the above procedure if $M(B)$ is not analytical.

In cylindrical coordinates Faraday's law can be written as

$$\frac{1}{r} \frac{\partial \left(rE\right)}{\partial r} = -\frac{\partial B}{\partial t}, \tag{B.9}$$

where B is, generally, the z-component of the magnetic field (parallel to the cylinder axis), and E is the azimuthal component of the induced electric field.

Since the electric field and current density in the superconductor are parallel, the heat generated will be positive ($Q > 0$), hence we can deal with absolute quantities and can omit the minus in front of the time derivative of magnetic field. From the above equation E can be obtained by integration, where it should be noted that the time derivative of magnetic field is a function of r. The time derivative can be approximated by the amount of change in magnetic field during one half cycle of applied field, ΔB, divided by the duration of one half-cycle, Δt. From the Bean model we can write

$$\Delta B = 2\left(\mu_0 J_C\left(r - r_0\right) + B_A\right), \tag{B.10}$$

which can be inserted into Faraday's law, giving the average local field over one half-cycle as

$$E(r) = \frac{1}{r}\int \frac{\Delta B}{\Delta t} r\, dr = \frac{1}{\Delta t}\left(\frac{2}{3}\mu_0 J_C r^2 - \left(\mu_0 J_C r_0 - B_A\right) r + \frac{C}{r}\right), \tag{B.11}$$

where the integration constant C is determined from the boundary condition that the electric field be zero at the penetration depth of the applied field, $E(r = r_0 - B_A/(\mu_0 J_C)) = 0$. To obtain the heat generation per cycle per volume the above expression is multiplied by Δt, and subsequently integrated over the superconductor cross-section, and divided by πr_0^2, giving the result

$$Q = \frac{2}{\pi r_0^2}\int 2\pi r\, E\Delta t\, J_C\, dr = \frac{4}{r_0^2}\int E\Delta t\, J_C\, r\, dr, \tag{B.12}$$

where the integral is evaluated in the interval $r_0 - B_A/(\mu_0 J_C) < r < r_0$. Evaluating the integral leads to the result from equation B.1. The normalised loss from equation B.1 is shown in Figure B.1.

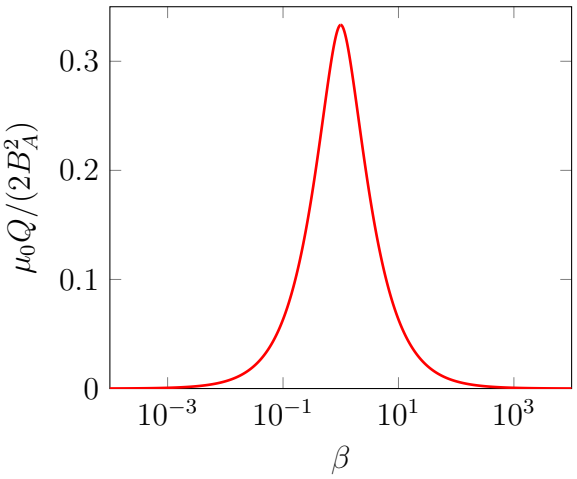

Fig. B.1 The normalised loss as a function of the reduced applied magnetic field amplitude, $\beta = B_A/B_P$.

Appendix C

Lorentz force distribution due to an M-shaped trapped field profile

The decay of trapped field will depend on the established circulating currents because of the direction of the Lorentz force, $\mathbf{F_L} = \mathbf{J} \times \mathbf{B}$, determined by the distribution of current density in the superconductor. A bulk of radius r_0 and height h, for example, which is partially magnetised using ZFC with the applied field amplitude of B_P (and not $2B_P$, the minimum amplitude needed for full magnetisation with ZFC), will exhibit an M-shaped trapped field profile due to current circulating in opposite directions in the bulk (see Figure C.1).

This means that, locally, the Lorentz force, felt by the flux vortices, can point inwards into the centre of the bulk. This is shown as negative values of F_L in Figure C.1. This means that if the superconductor in this configuration is exposed to AC magnetic fields, the flux vortices may become unpinned and move in the direction of the Lorentz force, towards the centre of the bulk. Hence, this effect could change the decay of trapped field, as measured by an array of Hall sensors on the surface of the bulk.

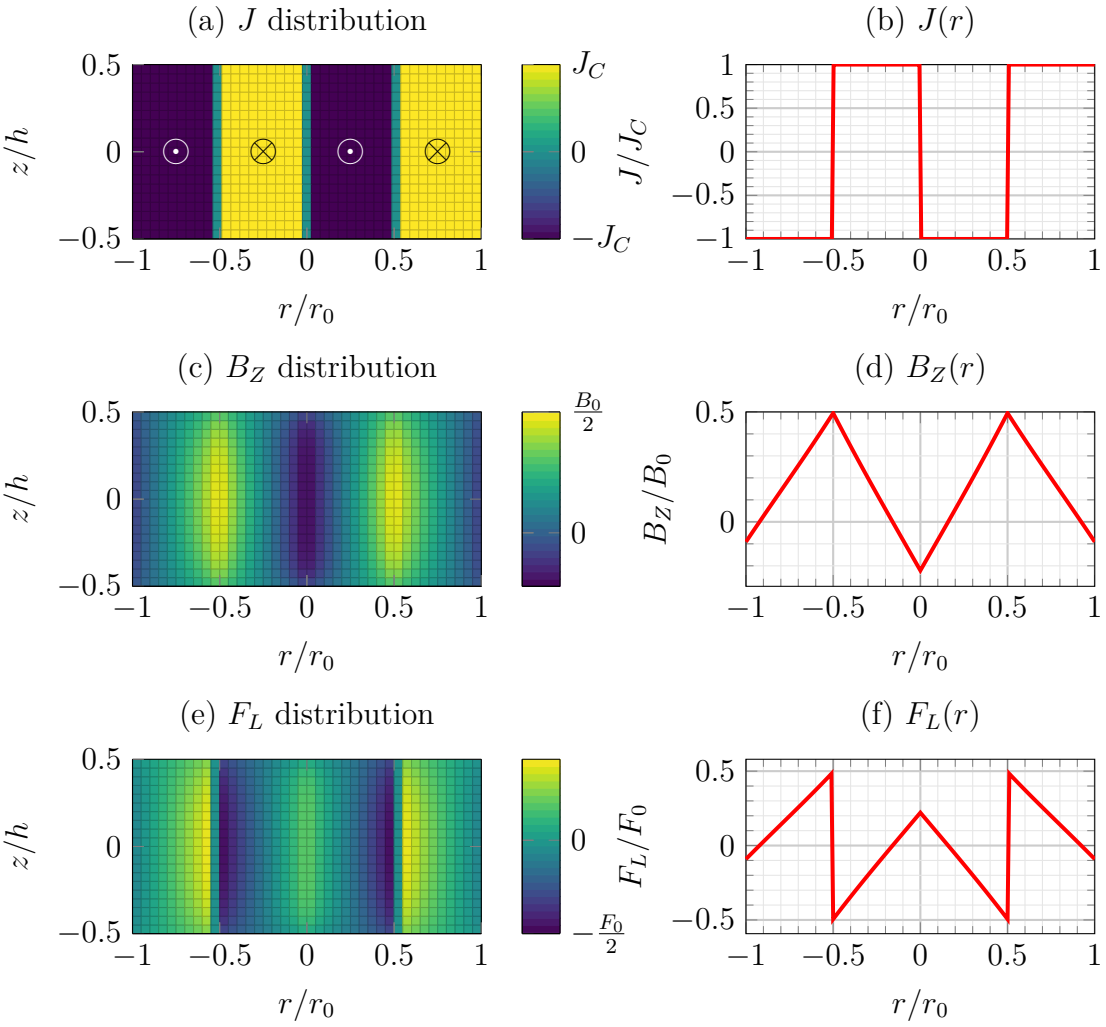

Fig. C.1 (a) The distribution of current density, J, leading to an M-shaped trapped field profile. (b) The dependence of $J(r)$ along $z = 0$. (c) The distribution of B_Z calculated from the distribution of J with the Biot-Savart law. Here, B_0 is the trapped field of a fully magnetised bulk. (d) The corresponding M-shaped profile of B_Z along $z = 0$. (e) The distribution of the Lorentz force, $F_L = BJ$. Here, $F_0 = B_0 J$. (f) The F_L profile along $z = 0$. Negative values correspond to its direction inwards to the bulk centre.

Appendix D

List of publications

- **J. Srpčič**, D. A. Moseley, F. Perez, K. Y. Huang, Y. Shi, A. R. Dennis, M. D. Ainslie, A. M. Campbell, M. Boll, D. A. Cardwell, J. H. Durrell, *Flux vortex dynamics in type-II superconductors.* Superconductor Science and Technology 33, 2020.
- **J. Srpčič**, F. Perez, K. Y. Huang, Y. Shi, M. D. Ainslie, A. R. Dennis, M. Filipenko, M. Boll, D. A. Cardwell, J. H. Durrell, *Penetration depth of shielding currents due to crossed magnetic fields in bulk (RE)-Ba-Cu-O superconductors.* Superconductor Science and Technology 32, 2019.
- **J. Srpčič**, D. Zhou, K. Y. Huang, Y. Shi, A. R. Dennis, M. D. Ainslie, A. M. Campbell, R. Bause, M. Boll, M. Filipenko, D. A. Cardwell, J. H. Durrell, *Demagnetization study of pulse-field magnetized bulk superconductors.* IEEE Transactions on Applied Superconductivity 28, 2018.
- K. Y. Huang, Y. Shi, **J. Srpčič**, M. D. Ainslie, D. K. Namburi, A. R. Dennis, D. Zhou, M. Boll, M. Filipenko, J. Jaroszynski, E. E. Hellstrom, D. A. Cardwell, J. H. Durrell, *Composite stacks for reliable* $> 17\,\mathrm{T}$ *trapped fields in bulk superconductor magnets.* Superconductor Science and Technology 33, 2020.
- D. Zhou, M. D. Ainslie, **J. Srpčič**, K. Y. Huang, Y. Shi, A. R. Dennis, D. A. Cardwell, J. H. Durrell, M. Boll, M. Filipenko, *Exploiting flux jumps for pulsed field magnetisation.* Superconductor Science and Technology 31, 2018.
- M. D. Ainslie, **J. Srpčič**, D. Zhou, H. Fujishiro, K. Takahashi, D. A. Cardwell, J. H. Durrell, *Towards optimisation of multi-pulse, pulsed field magnetisation of*

bulk high-temperature superconductors. IEEE Transactions on Applied Superconductivity 28, 2018.

- M. Kapolka, **J. Srpčič**, D. Zhou, M. D. Ainslie, E. Pardo, A. R. Dennis, *Demagnetisation of cubic Gd-Ba-Cu-O bulk superconductor by crossed-fields: measurement and three-dimensional modeling.* IEEE Transactions on Applied Superconductivity 28, 2018.

- K. Y. Huang, D. Zhou, **J. Srpčič**, Y. Shi, D. K. Namburi, A. R. Dennis, M. D. Ainslie, M. Boll, R. Bause, M. Filipenko, J. H. Durrell, D. A. Cardwell, *Spatial distribution of flexural strength in Y-Ba-Cu-O bulk superconductors.* IEEE Transactions on Applied Superconductivity 28, 2018.